STRUCTURAL, MORPHOLOGICAL, OPTICAL AND MAGNETIC PROPERTIES OF PURE AND TRANSITION METAL DOPED CADMIUM SULPHIDE NANOFILMS AT ROOM TEMPERATURE

THESIS SUBMITTED IN FULFILLMENT OF THE REQUIREMENTS FOR THE DEGREE OF

DOCTOR OF PHILOSOPHY

IN

PHYSICS

BY

SURESH KUMAR

[ENROLLMENT NUMBER 096901]

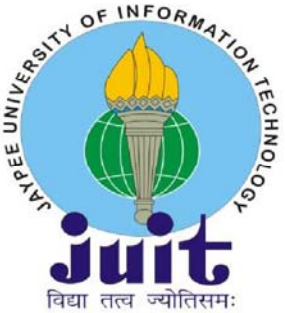

DEPARTMENT OF PHYSICS AND MATERIAL SCIENCE

JAYPEE UNIVERSITY OF INFORMATION TECHNOLOGY

WAKNAGHAT, SOLAN (H.P) – 173234

INDIA

JULY 2013

CERTIFICATE

This is to certify that the thesis entitled, "**Structural, morphological, optical and magnetic properties of pure and transition metal doped cadmium sulphide nanofilms at room temperature**" which is being submitted by **Mr. Suresh Kumar** for the award of degree of **Doctor of Philosophy** in **Physics** by the **Jaypee University of Information Technology** at Waknaghat, is the record of candidate's own work carried out by him under our supervision. This work has not been submitted partially or wholly to any other University or Institute for the award of this or any other degree or diploma.

Date: July 10, 2013

Dr. Vineet Sharma
Supervisor–I
Email: vineet.sharma@juit.ac.in
Mob.: +91 94182 33083

Dr. Pankaj Sharma
Supervisor–II
Email: pankaj.sharma@juit.ac.in
Mob.: +91 94189 52533

Acknowledgements

I express my sincerest gratitude to my supervisors, **Dr. Vineet Sharma** and **Dr. Pankaj Sharma** for leading me through all these years. Their positive attitude towards research and zest for research work has prompted me for the timely completion of the work.

I would like to thank **Prof. (Dr.) Yajulu Medury (COO, JES)**, **Brig. (Retd.) Balbir Singh (Director, JUIT), Prof. T. S. Lamba (Dean, A & R)** and **Prof. P. B. Barman (HOD, Physics & Materials Science)** for providing all kinds of facilities to carry out my research work.

I extend my gratitude to Prof. S. C. Katyal (JIIT, Noida), Prof. (Dr.) Sunil K. Khah, Dr. Dheeraj Sharma, Dr. Rajesh Kumar, Dr. S. K. Hazra, Dr. Ragini R. Singh and Dr. S. K. Tiwari for their consistent support and encouragement. I also thank the technical staff; Mr. Kamlesh Mistra, Mr. Ravinder Tiwari, Mr. Deepak Singh, Mr. Baleshwar Shukla, Mr. Manoj Panday and Mr. Promod Kumar for their help during my research work.

I would like to thank Dr. R. S. Gulia (Director General, HGPI, Sirmour), Mr. Kuldeep Singh Rana (SDO, HVPN), Dr. S. K. Sharma (Director General, DVIET, Karnal), Dr. Santosh Kumar (GIST, Korea), Dr. V. S. Rangra (HPU, Shimla), Dr. N. S. Negi (HPU, Shimla), Mr. T. S. Chaudhary (KIT, Ambala), Mr. N. K. Juyal (WIHG, Dehradun) and Mr. J. K. Gangwar (Hartron, Ambala) for their generous help during my research work.

I would like to extend my gratitude to Dr. Dixit Prashar (JU, Gawalior), Dr. Dinesh Kumar and Dr. Amanpal Singh (KU, Kurukshetra), Dr. Kameshwer Kumar and Ms. Ashu Sharma (HPU, Shimla) and Mr. Sukvinder Saini (PU, Chandigarh) for their help in various characterizations.

Besides, I can never ever forget my colleagues, Jatin, Jibesh, Varun, Swapnil, Abhishak, Sunanda, Neha, Pawan, Ankush, Hitanshu, Dikshita, JaiVardhan, Richa, Krishna, Sk Emdadul and Swati from JUIT who have helped me in a numerous ways. I cherish the years spent in the Deptt. of Physics and Materials Science, JUIT, Waknaghat.

Special thanks to my long time friends Sukhavinder, Surinder, Manoj, Sushil, Mridul, Mukul, Bishan, Ajay, Kavita, Rekha, Manoop, Narinder, Sunil, Ashish, Anmol, Satindra, Naveen, Harpal, Amit, Barjinder, Raj, Pawan, Ravinder and

Subhash for their wonderful friendship. I would like to express my heartfelt appreciation to all those who have contributed directly/indirectly.

Life is miserable without parents and beloved ones. I can't forget the pain that my parents and in-laws have taken throughout my research work. It is only because of their support, love and blessings that I could overcome all frustrations and failures. I am also thankful to both of my sisters for their moral support.

To my dearest son '**Arindam**' for bringing joy and happiness into my life.

Cordially, I thank to my wife '**Anuradha**', my love, for having patience in these distance working years and for encouraging and inspiring me when things do not work properly. Without her strength and profound support I would not be here and this work will not be accomplished.

Thank you all.

I am forever thankful to Almighty God for the life and all the countless blessings.

Date: July 10, 2013 **[Suresh Kumar]**

CONTENTS

List of Figures

List of Tables

CHAPTER 1

Introduction

JAYPEE UNIVERSITY OF INFORMATION TECHNOLOGY
juit
विद्या तत्व ज्योतिसमः

In the modern era of science and technology, role of materials is inevitable. Materials science is an approach to investigate the relationships that exist between the structures and properties of materials. Materials influence all segments of our everyday lives. Various kinds of materials are being used in industry, housing, agriculture, medical, transportation, communication, etc., to meet the needs of individual and society. Materials can be classified as solids and fluids according to their flow or mechanical behavior. The solids are the materials whose shear viscosities exceed $10^{14.6}$ poise whereas viscosities of fluids are less than $10^{14.6}$ poise [1]. On technical ground, materials can be classified as metals, semiconductors, insulators, ceramics, glasses, composites, biomaterials, polymers, etc. Semiconductors have attracted significant attention after the discovery of transistor (Bardeen, Brattain and Shockley; 1947) and become most important materials for fabrication of electronic and optoelectronic devices. A few semiconductors such as Si, Ge, GaAs, InP, SiC, CdS, ZnS, ZnSe, CdSe, CdTe, ZnO, GaN, InGaAs, AlInGaP, etc. exhibit excellent applications in modern technology. Some manifestations of semiconductor technology can be easily seen in daily life appliances such as electronic balance, video games, radio, television, mobile phone, watches, CD player, stereo, computer, digital lights, calculator, diagnostic equipments, refrigerator, security devices, toys and many more. The developments in semiconductor technology during the past 60 years have made electronic devices smaller, faster, efficient and more reliable. Advances in the field of semiconductor science and technology go on continuously to improve our lives. Semiconducting materials have band gap (> 0 eV and < 4 eV and electrical conductivity (10^{2} Scm^{-1} – 10^{-9} Scm^{-1}) at room temperature are called semiconductors. The properties of semiconductors are intermediate to metals and insulators.

1.1 Semiconductors: science and technology

The electrical conductivity of semiconductors may be controlled by doping, temperature, external electric and magnetic field. At absolute zero, pure semiconductor acts as an insulator having electrical conductivity $> 10^{-14}$ Scm^{-1} [2]. Semiconductors can be classified in several ways (Figure 1.1). On the basis of structure, semiconductors are of two types as crystalline and non–crystalline. In crystalline semiconductors, the atoms are stacked in a regular manner, forming a three dimensional periodic arrangement of constituent particles (atoms, ions or molecules). They have long range order and thus, have definite properties such as sharp melting

point, definite heat of fusion, anisotropy, etc. A single crystal or monocrystalline semiconductor has continuous crystal lattice of the entire sample and unbroken to the edges of the sample, with no grain boundaries. Examples of single crystals are pure Si, Ge and GaAs, etc. When the periodicity in the crystal structure is interrupted at grain boundaries, the crystal is said to be polycrystalline. In this case the size of the grains is smaller than the size of the unit cells. The size of the grains in which the structure is periodic may vary from macroscopic dimensions to several angstroms. In the majority of the semiconductor applications, single crystal semiconductors are used because of their superior electrical properties. Polycrystalline semiconductors show electrical behavior similar to that of single crystal, but their conductivity is significantly lower due to the presence of grain boundaries which obstruct the flow of mobile carriers. Non–crystalline or amorphous semiconductors are having short range order and lack crystalline periodicity. Oxide glasses (silicates), glassy chalcogenides and amorphous Si (or Ge) are the most familiar non–crystalline semiconductors. On the basis of nature of the current carriers, semiconductors are ionic and electronic. In ionic semiconductors such as AgBr, Cu_2O, etc., the conduction takes place through the movement of ions and is accompanied by mass transport. In electronic semiconductors, the conduction takes place due to flow of electrons without any mass transformation.

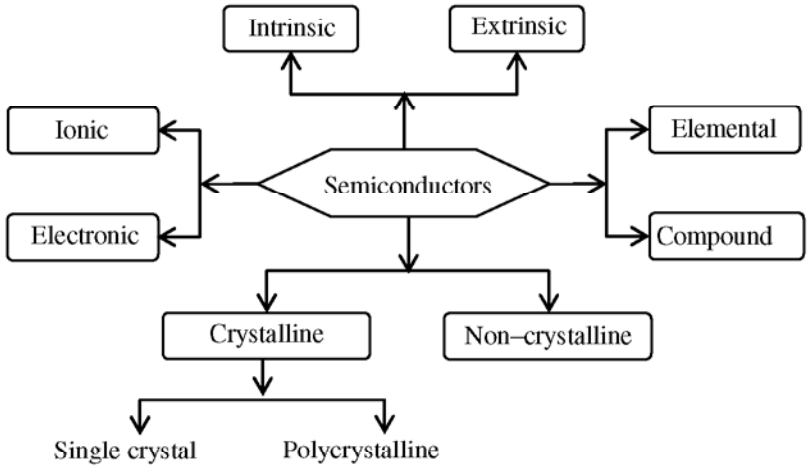

Figure 1.1 Classification of semiconductors

Semiconductors may also be classified as elemental and compound. In elemental semiconductors, all the constituent atoms are of the same kind (group IV elements: C, Si and Ge), whereas a compound semiconductor consists of two or more

different elements (group III–V, II–VI, II–IV–V, etc., elements). On the basis of impurity addition, semiconductors are intrinsic (electrical behavior is based on the electronic structure inherent to the pure crystal) and extrinsic (electrical behavior is directed by nature of impurity atoms *i.e.*, *n*–type and *p*–type).

In recent years, major research focus is on the synthesis, characterization and application of semiconductors. In emerging technologies these semiconductors are explored and used in different forms such as quantum dots (QDs), nanoclusters, nanotubes, nanowires, nanofilms, etc. When the size of semiconductors reduces to nanoscale, their properties change dramatically due to large surface area or quantum size effect (QSE). The large surface to volume ratio and quantum confinement of semiconductor nanomaterials offer greater chemical reactivity, affect their strength, novel transport properties, enhanced optical, electrical and magnetic behavior. Semiconductor nanomaterials and devices are attracting researchers in many fields, such as solar cells, electronic devices, laser technology, waveguide, LEDs, chemical and biosensors, energy conversion, packaging films, etc. [3–9]. There are a large number of materials showing semiconducting behavior including elemental semiconductors (group IV), binary semiconductors (group III–V, II–VI), ternary semiconductors (group I–III–VI, II–IV–V), etc. In the recent years, particularly II–VI semiconductors have progressively attracted researchers due to their optically active nature and size dependent exciton energy. They have relatively high band gap energy, large ionicity, high effective mass of carriers, small radiative carrier lifetime and short carrier diffusion in comparison to III–V compounds [4]. II–VI nanomaterials show high performance in optoelectronics devices [4,9–11]. They are also significantly used in catalysis, electronics, photonics, sensing, nano devices, etc. [12–16].

1.2 II–VI semiconductors

The binary compound $A^{II}B^{VI}$, where A is divalent and B is hexavalent (chalcogen element), is called II–VI semiconductor. A list of II–VI semiconductors is given in Table 1.1. Most of the II–VI semiconductors are crystallized in cubic–zinc blende (ZW) or hexagonal–wurtzite (WZ) or polymorph structure where each anion is surrounded by four cations at the corners of a tetrahedron and vice versa. This tetrahedral coordination is typical of s–p^3 covalent bonding however, these materials also have a substantial ionic character. The ionic character varies considerably over the whole range and increases as the atomic size decreases. Therefore the bonding is

predominantly ionic in ZnS while HgTe is nearly covalent. Hence, band gap for compound with more ionic character is higher than that of covalent compound.

Table 1.1 II–VI semiconductors

Group II B ↓	Group VI A ↓			
	O	**S**	**Se**	**Te**
Zn	ZnO	ZnS	ZnSe	ZnTe
Cd	CdO	CdS	CdSe	CdTe
Hg	HgO	HgS	HgSe	HgTe

All II–VI semiconductors are direct band gap in nature. The band gap ranges from infrared (IR) to ultraviolet (UV) region of electromagnetic spectrum with high optical transition probabilities for absorption and emission. Interaction of phonon is essential during light absorption and luminescence process in order to conserve energy and momentum. Hence, radiative transition probability increase significantly in direct band gap semiconductors and make them suitable for many electronic as well as optoelectronic applications. The group VI elements (except O) are called chalcogenides. Among the chalcogenides of mercury, HgS is a semiconductor whereas both HgSe and HgTe are semimetals. However, remaining six compounds form a group of II–VI semiconductors (Table 1.1). Few of the II–VI semiconductors properties are summarized in Table 1.2. II–VI semiconductors can be easily prepared in high quality polycrystalline and nanocrystalline films. The materials used in synthesis of these semiconductors are relatively inexpensive and experimental process involves low cost techniques such as chemical bath deposition (CBD), spray pyrolysis and electrochemical deposition. Thus, the use of II–VI films presents an economical approach synthesis of semiconductors for various applications (Figure 1.2). These II–VI semiconductors can be further classified in two major categories:

(i) II–VI oxide semiconductors

(ii) II–VI non–oxide semiconductors

Table 1.2 Properties of II–VI semiconductors at 300 K

System	Stable structure[*]	Lattice Parameters[*] (Å)	Band gap[*] (eV)	Electron affinity[*] (eV)	Conductivity type [*]	Refractive index [#]
ZnO	WZ	$a = 3.250^{\Theta}$ $c = 5.120$	3.35^{Θ}	4.10	*n*	2.03
ZnS	ZB	$a = 5.409$	3.66	3.90	*n*	2.37
	WZ	$a = 3.819$ $c = 6.256$	3.91^{Θ}			2.38
ZnSe	ZB	$a = 5.669$	2.67	4.09	*n, p*	2.5
ZnTe	ZB	$a = 6.104$	2.25	3.50	*p*	2.72
CdO	RS	$a = 4.710$	2.40	….	*n*	….
CdS	WZ	$a = 4.137$ $c = 6.716$	2.42	4.50	*n*	2.53
CdSe	WZ	$a = 4.298$ $c = 7.010$	1.74	4.95	*n*	2.5
CdTe	ZB	$a = 6.481$	1.45	4.28	*n, p*	2.72

[*] Ref. 4, [#] Ref. 17 and [Θ] Ref. 18

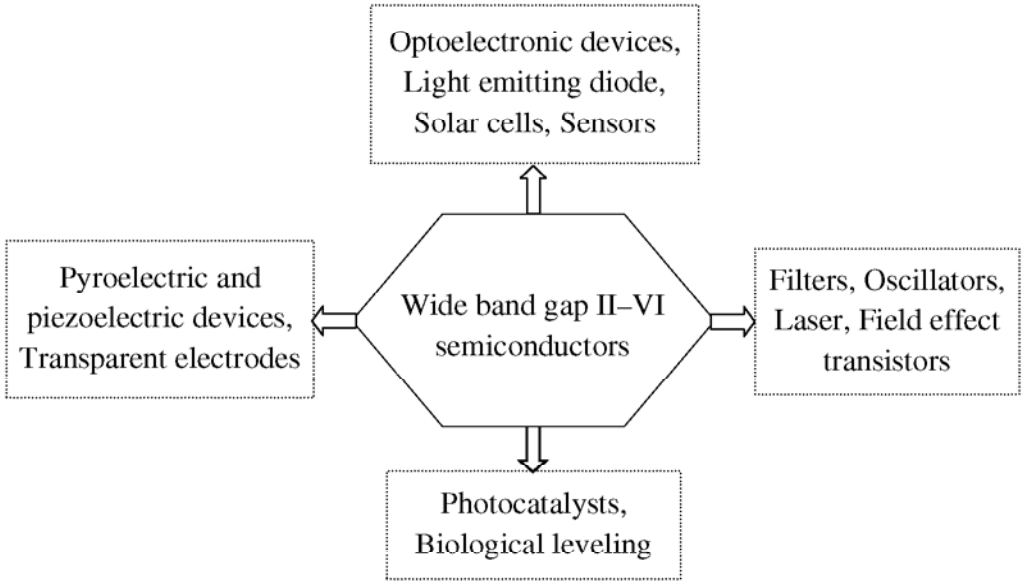

Figure 1.2 Applications of II–VI semiconductor films.

1.2.1 II–VI oxide semiconductors

ZnO is a metal oxide semiconductor which has gained substantial interest in the research community because of its large free exciton binding energy (60 meV), strong cohesive energy (1.89 eV), high optical gain (300 cm^{-1}), radiation hardness, high mechanical and thermal stabilities [19]. ZnO is a direct band gap semiconductor having stable WZ structure, high free carrier concentration (10^{21} cm^{-3}) and Hall mobility (~ 200 $cm^2V^{-1}s^{-1}$) [4,18]. Generally, ZnO has *n*–type character while *p*–type character has been proven difficult to achieve [18]. Minegishi *et al.* have deposited highly resistive (~ 100 Ωcm) *p*–type ZnO thin films with very low concentration of mobile holes [20]. Hwang *et al.* have reported *p*–type conductivity in vacuum annealed ZnO films deposited on (*001*) GaAs substrates [21]. Sharma *et al.* have reported the ferromagnetism above room temperature in both bulk and thin film forms of $Zn_{1-x}Mn_xO$ with $x < 4$ at.% [22]. Also, *n*–type doping in Fe, Co, or Ni doped ZnO has been predicted to stabilize high T_c ferromagnetism [23]. *n*–type ZnO films on other *p*–type materials such as Si, NiO, GaN, AlGaN, ZnTe, CdTe, etc., have been used for many *p*–*n* heterostructure devices [24]. A high intensity UV emission has been observed from *n*–ZnO/*p*–AlGaN heterojunction in which ZnO has served as the active layer [24]. ZnO (II–VI) has some advantages over GaN (III–V), which is widely used in light emitting diodes (LEDs), such as preparation of high quality single crystals, large exciton binding energy and simple synthesis methods in bulk and nanostructured film form. It has been utilized in many commercial applications such as integrated optics, liquid crystal displays (LCDs), laser diodes, UV detectors, photocatalysts, etc. [20–24].

CdO was first deposited as a transparent conducting film in 1907 [25]. It can be found as colorless amorphous powder or as brown or red crystals. It is used as a transparent material and is a *n*–type semiconductor under the non–stoichiometric condition of interstitial Cd or O vacancies with the direct band gap of 2.2 eV – 2.5 eV and the indirect band gap of 1.36 eV – 1.98 eV [26]. The crystal structure of CdO is rocksalt (RS) type and is similar to NaCl. CdO is regarded as the densest structure of CdO_6 octahedra [27]. CdO films have been used in various applications such as phototransistors, transparent conducting oxides (TCO), LCDs, IR detectors, phenol photodegradation and anti reflection coatings [26,28]. Khallaf *et al.* have deposited CdO films on glass substrates using different complexing agents by CBD technique

[28]. They have observed optical band gap of as–deposited films in the range 3.37 eV – 4.64 eV and 2.53 eV for annealed films [28].

1.2.2 II–VI non–oxide semiconductors

ZnS exists in two stable crystal structures ZB and WZ with direct band gap [4]. Generally, WZ form is considered to be desirable due to its optical properties. However, ZB structure of ZnS is stable below 1593 K [4]. ZnS has been synthesized in different forms such as nanoparticles, nanowires, nanobelts, nanocombs, nanofilms, nanohelices, etc., by various techniques [29,30]. ZnS is an important phosphor host lattice material used in electroluminescent devices because of its large band gap. ZnS has been extensively studied for a variety of applications such as electro–optic modulators, field effect transistors (FETs), electroluminescent devices, etc. [31,32]. Bhargava *et al.* have reported luminescence properties of Mn doped ZnS nanocrystals of size 3.5 nm – 7.5 nm [33]. A deep blue LED based on chemically synthesized $Cd_{1-x}Zn_xS$@ZnS QDs has been demonstrated by Bae *et al.* [34]. The magnetic behavior of transition metal (TM) doped ZnS nanoparticles and thin films have been extensively studied by various researchers [23, 35–37]. The growth mechanism for the deposition of undoped and doped ZnS films by CBD has been reported [38,39].

ZnSe is a light yellow binary semiconductor which exist both in WZ and ZB crystal structure. It is a direct band gap (2.67 eV) semiconductor with an electron affinity 4.09 eV, binding energy 22 meV, electron mobility 530 $cm^2V^{-1}s^{-1}$, free carrier concentration 4.37×10^{11} cm^{-3}, conductivity ~ 10^{-4} Scm^{-1} and small exciton Bohr radius 3.8 nm [40,41]. Among all II–VI compounds, ZnSe can be prepared in both *n* and *p*–type forms [4]. Group VII (halogens), III (In, Al), etc., can be used for *n*–type doping while *p*–type ZnSe are obtained by N and Li doping. ZnSe films of thickness 30 nm – 100 nm with resistivity ~ 20 Ωcm have been deposited on $CuInSe_2$ films for designing ZnO/ZnSe/$CuInSe_2$ solar cells having conversion efficiency of 10% [4]. Hankare *et al.* have reported a decrease in band gap and an increase in electrical conductivity of polycrystalline ZnSe thin films with increasing annealing temperature [42]. ZnSe is a popular material for IR applications because of its high refractive index and low dispersion rate at IR wavelengths. Its valence band edge is at a higher energy level *w.r.t.* ZnS. Hence, regarded as an efficient host to dope different TM ions for various applications [43–45]. The existence of magnetism with doping in ZnSe nanostructures has been studied by various researchers [23,46,47].

ZnTe is a *p*–type semiconductor with ruby red appearance in crystal and grey or brownish red in powder form. ZnTe typically has a stable ZW crystal structure. This ZW structure allows it to be grown on various substrates like GaAs, GaSb, AlSb, InAs, PbSe, etc., in addition to glass and quartz [48–51]. Easy feasibility of doping in ZnTe makes it a perspective material for designing green, blue LEDs, laser diodes, devices operating under THz frequencies, etc. [48–51]. ZnTe films have low conductivity than the bulk and their conductivity has been found to increase with doping, for example Ag doped ZnTe films [52]. An increased In doping in ZnTe has been reported to decrease the optical band gap [51]. ZnTe films are popularly used for making back contact in CdS/CdTe heterojunction solar cell [48]. Saito *et al.* have observed ferromagnetism in $Zn_{1-x}Cr_xTe$ films with critical temperature (T_c) ~ 300 K for x = 0.2 [49]. A half metallic ferromagnetism, antiferromagnetism with excess doping and spin glass behavior has also been reported in ZnTe: Mn, ZnTe: Cr and ZnTe: V systems [23,49,53].

In II–VI semiconductor, CdTe is one of the leading photovoltaic (PV) and sensor material because of its direct band gap (1.5 eV at room temperature) that corresponds closely to sunlight spectrum [54,55]. CdTe has high optical absorption coefficient ($> 5 \times 10^5$ cm^{-1}) and electron mobility ~ 1100 $cm^2V^{-1}s^{-1}$ [54]. A thin layer of CdTe with thickness of ~ 2 μm has been reported to absorb nearly 99% of the incident radiation, hence, used as *p*–type absorber layer in solar cells [54]. Due to high ionicity (7.7%) of CdTe, the crystallites show strong chemical bonding (5.75 eV) leading to high chemical and thermal stability [54]. CdTe shows both *n*–type (Cd excess) and *p*–type (Te excess) conductivity which is further enhanced by impurity doping with In, As, Ga, Ag, Sb, etc. [56,57]. Post deposition treatment with $CdCl_2$ further improves the quality of CdTe films. In comparison to Si detectors, the large atomic numbers of Cd (48) and Te (52) extend the operation range of CdTe detectors to a higher photon energy (up to 1 MeV) without cryogenic cooling [58]. Hg doped CdTe is suitable for IR detection in 8 nm – 12 mm range and Zn doped CdTe shows excellent properties for solid state x–ray and γ–ray detection [58,59]. Mn doped CdTe is a semi–magnetic semiconductor used as antiferromagnetic and mid–IR lasing material at room temperature [59]. Alver *et al.* have reported room temperature ferromagnetism in Co doped CdTe films which improved with thermal annealing [60]. Nanostructured CdTe QDs can be easily synthesized from aqueous phase and

used in biological applications to distinguish different kinds of antigen, labeling of tumor cells, sensing of drug delivery, detection of residual pesticides, etc. [61].

Another II–VI semiconductor, CdSe is potentially used in TFTs, gas sensors, acousto–optic devices, photoreceptors, electro photography, optoelectronic devices, laser diodes, biomedical imaging, etc. [61–65]. The first active matrix LCD showing a still picture has been manufactured in 1973 using CdSe [66]. CdSe/Ti is used as photoanode in photo electrochemical (PEC) cells for hydrogen production [63]. Generally, CdSe is known to exist in stable hexagonal and metastable cubic structure with lattice constant a = 6.08 Å [62]. It has been reported that the phase transformation of cubic to hexagonal CdSe (bulk) takes place at high temperature (> 1273 K), whereas cubic CdSe thin films convert to hexagonal at 723 K [64]. CdSe is n–type with the resistivity ~ 10^6 Ωcm and an electron mobility 650 $cm^2V^{-1}s^{-1}$ [63,64]. The n–type CdSe can be easily obtained by doping with Ga, In, Sb, etc. However, p–type conductivity in CdSe is more difficult to achieve. N and Cu dopants are used to obtain p–type CdSe. CdSe has a direct band gap of 1.73 eV (Bulk) at room temperature, high absorption coefficient (~ 10^5 cm^{-1}), low exciton binding energy 15 meV, high photosensitivity and large exciton Bohr radius (5.4 nm) [62]. Nanostructured CdSe in various forms show quantum confinement and tunable optoelectronic properties [62,65]. Various studies have reported ferromagnetic, paramagnetic and superparamagnetic behavior for Cu, Ni, Mn and Fe doped CdSe nanostructures under different growth conditions [67,68].

1.3 CdS semiconductor

In II–VI semiconductor family, cadmium sulphide (CdS) is an important inorganic chemical compound. The appearance of CdS powder or crystal is yellow to dark orange in colour and appears white for crystallites of size < 3 nm. CdS has attracted much attention within the scientific community from the beginning of semiconductor research due to its excellent structural, optical and electrical properties.

CdS has excellent chemistry with other II–VI semiconductors and a lot of work has been reported for these compounds, core shells, composites, heterostructures, etc. [14–16,70–74]. CdS has also shown promisingly application with other elements of periodic table and semiconductor groups [32,70, 75,76]. A ZnTe/CdS heterojunction system has been reported for PV solar energy conversion and green emitting injection luminescence device applications [14,15,77]. Fang *et al.*

have reported TiO_2 electrode sensitized with CdS to extend the optical absorption and photocurrent action spectrum into a wider visible range facilitating the photon to photocurrent conversion efficiently [75]. The transparent nano CdS–polyurethane films show a QSE and are utilized in photocatalytic H_2 generation [78]. Oladeji and Chow studied homogeneous $Cd_{1-x}Zn_xS$ thin films deposited by low temperature CBD [32]. The depth profile analysis indicated that Cd diffuses into ZnS film more readily than Zn into CdS film. Further, they verified that these films could be used to improve the spectral response of CdTe based solar cells. Saren *et al.* studied water soluble and biotaggable CdSe–CdS nanocrystals encapsulated in phospholipid liposomes which are used in drug/gene delivery applications [13]. Kirovskaya *et al.* illustrated that the InP–CdS and ZnTe–CdS thin film systems have been are proven to be active adsorbents and sensitive elements for sensors and photocatalysts which help in detection and neutralization of toxic gases [14].

The values of general physical quantities for CdS semiconductor at room temperature are shown in Table 1.1.

Table 1.3 General properties of bulk CdS at 300 K

Physical quantity	**Structure**	**Value**
Molecular weight (amu)	….	144.477
Lattice constant (Å)	ZB	$a_0 = 5.82^{\#}$
	WZ	$a_0 = b_0 = 4.137^{*}$ $c_0 = 6.716^{*}$
Bond length (μm)	ZB	$2.530^{\#}$
Crystal density (gcm^{-3})	ZB	$4.855^{\blacklozenge}$
	WZ	4.820
Melting point (K)	….	$2023^{\#}$
Dielectric constant	….	$\varepsilon_r = 8.6^{\#}$ $\varepsilon_i = 5.3^{\#}$
Refractive Index	ZB	$2.506^{\blacklozenge}$
	WZ	$2.529^{\#}$
Electron effective mass (m^*_e/m_e)	….	$0.19^{\#}$
Carrier concentration n/p (cm^{-3})	….	$10^{18\#}$
Electron Hall mobility ($cm^2V^{-1}s^{-1}$)	….	$350^{\#}$
Resistivity range (Ωcm)	…..	$10^1 – 10^{8\#}$

[*] Ref. 4, [#] Ref. 17 and [♦] Ref. 87

CdS has applications in various sectors like photoconduction, photovoltaics, microelectronics and optoelectronics. Recently, TM doped CdS has become popular material for magneto–optical and spintronic applications [79]. CdS based devices include LEDs, photoresistors, FETs, optical filters, photodetectors, gas sensors, optical waveguides, nonlinear integrated optical devices, biological markers, radiation detectors, piezoelectric ultrasonic transducers, piezoelectric acoustic resonators, photocatalysts, blue green lasers, phosphors, electroluminescent devices, etc. [15,73,76,80–86]. Thus, the studies on structural, morphological and optical properties of CdS semiconductor are very important in term of efficient fabrication and functioning of various devices.

1.3.1 Structural and morphological properties

In general, CdS exists in two structural forms; cubic or sphalerite–ZB and hexagonal–WZ (Figure 1.3). ZB structure consists of two interpenetrating *fcc* sub–lattices (one of Cd atoms and other of S atoms) displaced from each other along the body diagonal by $a/4$, a being the lattice constant for the ZB structure. All the Cd–S bonds lie parallel to the body diagonal of the cube point. However, WZ structure comprises of two interpenetrating *hcp* sub–lattices (one of Cd atoms and other of S atoms) displaced from each other by $3c/8$ along the c–axis where c is the lattice constant. The Cd–S bonds are parallel to the c–axis and all points lie in same direction. These arrangements of atoms result into two different stacking sequences: *ABCABC*... along (*111*) direction for ZB and *ABAB*... along c–axis for WZ [88,89]. In

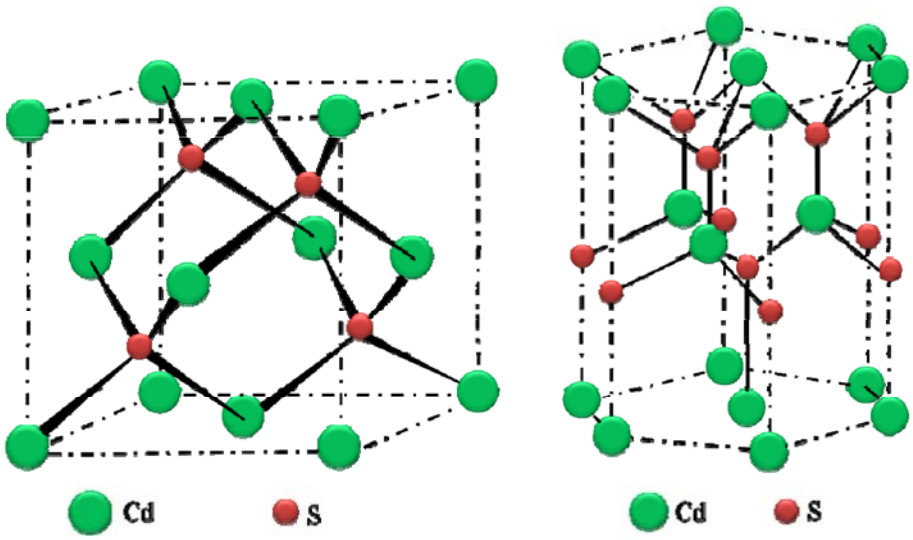

Figure 1.3 CdS crystal structure (a) ZB (b) WZ

both structures each atom is tetrahedrally surrounded by four atoms of the other kind, but the arrangement of the tetrahedral for WZ is such that a lattice has hexagonal symmetry and cubic symmetry for ZB. WZ structure of CdS is closely related to ZB because total energy difference between them is subtle (~ 1.1 meV/atom) [90].

Generally, CdS films grow in both crystal structures and commonly, the combination is known as polymorph structure. WZ phase is thermodynamically more stable than ZB [4]. The phase transition of CdS films, from metastable ZB to stable WZ under ambient pressure, occurs at approximately 593 K where its colour changes from pale yellow to dark orange. However, CdS under very high pressure (~ 3 GPa) transforms into a rare crystal structure *i.e.*, rocksalt (RS) [91].

Derin *et al.* used thermal evaporation technique to deposit cubic phase CdS thin films with lattice constants a = 5.82 Å having crystallite size in the range of 17.3 nm – 34.5 nm on Au substrates [92]. Dingyu *et al.* have deposited hexagonal CdS films with preferred orientation along the (*002*) plane having crystallite size from 34.4 nm – 44.4 nm by thermal evaporation [93]. CdS films deposited by thermal evaporation on heated substrates typically comprised of columnar crystals with the c–axis perpendicular to the substrate and size of crystallites increased with increase in substrate temperature [94,95]. Hu *et al.* have deposited hexagonal polycrystalline CdS films by magnetic sputtering on different substrates (glass, quartz, SnO_2 and Si) with sputtering powers of 100 W – 200 W, pressures of 0.1 Pa – 0.5 Pa and substrate temperatures of 373 K – 523 K [96]. Dhawale *et al.* have deposited hexagonal CdS nanorods having prominent orientation along (*100*) plane on glass substrates by simple successive ionic layer adsorption and reaction (SILAR) method [97]. Morphological analysis revealed that the CdS films have thickness between 130 nm – 1230 nm and surface to be composed of spherical grains along with porous spongy clusters. The increase in film thickness leads to the formation of matured nanorods having diameter 150 nm – 200 nm [97]. Tong *et al.* have reported mixed phase in CdS films on Si and quartz substrates using femto–second pulsed laser deposition [98]. The small grain size, low root mean square (*rms*) roughness and low stress have been reported for films deposited on quartz substrate in comparison to Si substrate.

Polymorph CdS films deposited by CBD have been reported by various researchers [99–102]. However, pure cubic phase CdS films [94,103,104] and pure hexagonal phase by CBD are also reported in the literature [105–107]. Lazos *et al.* have studied surface morphology of CdS films as a function of number of depositions

[107]. They observed that superficial grains are uniformly distributed on the film surface and surface roughness remains constant. In addition, grain size also increased with the number of dips and acquired round shape. Kim *et al.* reported the surface morphology of CdS thin films prepared using modified CBD technique. The ultrasonication reduced *rms* roughness and grain size of the films by disrupting the homogeneous reaction by–product and the large size CdS cluster breaks into smaller ones[108]. Acevedo *et al*. have reported a comparative study on the properties of hexagonal CdS thin films deposited on SnO_2 glass by laser ablation, close space vapor transport, sputtering and CBD techniques. CdS films deposited by CBD were found to have low grain size (70 nm), low *rms* roughness (23 nm), high band gap (2.48 eV) and high figure of merit (421.3) in comparison to the films deposited by other techniques [109]. Lee J has reported that CdS films deposited by CBD have small grains with cubic phase whereas vacuum evaporated films have large grains with hexagonal phase [110]. Moreover, CdS films deposited by CBD for various applications yield higher and more stable characteristics [110].

To deposit size tunable CdS semiconducting films with desired phase, scaled grain formation, improved morphology and better adhesion qualities, the CBD technique provide better possibilities in comparison to other deposition techniques.

1.3.2 Optical properties

In semiconductors, there is a forbidden energy region where no allowed states can exist. Above and below this energy region, are permitted energy states (bands). The upper band is called conduction band (CB) and the lower is valence band (VB). The energy gap between the highest filled VB and lowest filled CB is called the band gap [3]. The band gap is the most important parameter of semiconductors which affects their optical, electrical and electronic properties. For an electron to jump from VB to CB, it needs energy ($h\nu$) equal to the band gap, leaving behind a vacancy known as hole. If a photon has more energy than the band gap, then it will excite electron from lower in the VB to higher in the CB. However, the excess energy is lost through inelastic collisions as the electron settles to the bottom of the CB and the hole rises to the top of the VB. The electron always returns to its ground state through electron–hole recombination process in which a photon is emitted having energy equal to the band gap. A scheme of the energy band gap of a semiconductor (in different forms) absorbing a photon and emitting a photon is shown in Figure 1.4. The

change in the dimensions of semiconductor will change its properties and add many features. For decreasing size of a crystalline semiconductor, starting from bulk to quantum dot the allowed energy levels gradually broaden and become more discrete. In nanostructured semiconductors, the edges of the band structure are not completely developed and show more discrete levels with Fermi energy lying in the band gap. For QDs or nano clusters the orbital sets are developed into CB and VB. The highest occupied molecular orbital (HOMO) becomes the top of the VB and the lowest unoccupied molecular orbital (LUMO) becomes the bottom of the CB. The decreasing size of semiconductor leads to the broadening of band gap. The electrons, holes and excitons in nanocrystallites have limited space to move and their motion is possible only for definite values of the energy. As a result, the continuum of states in the CB and VB are broken down into discrete states with energy spacing approximated by inverse of the square of crystallite radius. Hence, broadening of the band gap in comparison to the bulk takes place, *i.e.*, a blue shift in the optical absorption spectra.

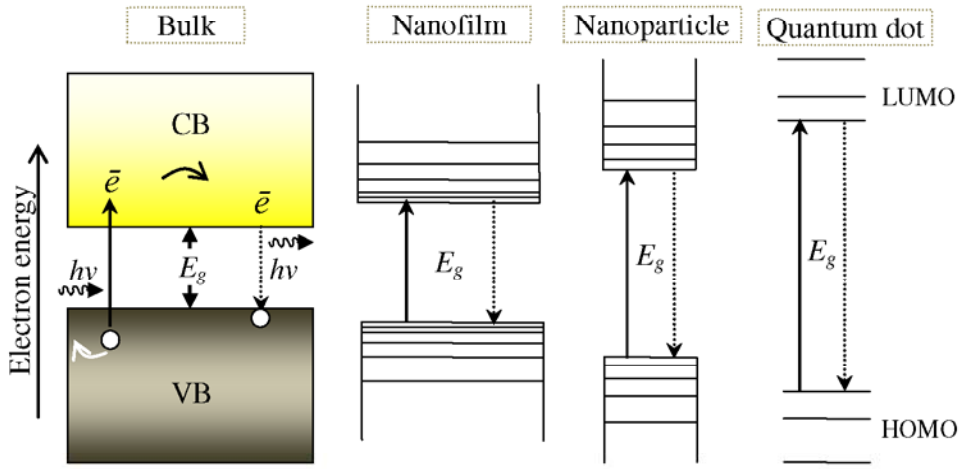

Figure 1.4 Energy band gap scheme for semiconductors from bulk to quantum dot

Several theoreticians have described the blue shift behavior of a semiconductor as a function of particle size [111–115]. Effective mass approximation (EMA) is the most popular theoretical effort used to understand the size dependent band gap behavior of low dimensional systems because of its simplicity. The other treatments that are used to describe the band gap of nanoparticles include the tight binding approximation (TBA), the effective bond orbital model (EBOM), Wannier function method (WFM), empirical pseudo potential method (EPM), density functional theory (DFT) and hyperbolic band model (HBM) [111–115]. For

nanostructured CdS, the band gap can be tuned between 2.42 eV – 4 eV by varying the size of crystallites. The smaller crystallites are blue shifted *w.r.t.* the larger ones showing quantum confinement in them. In practice, two types of confinements are observed for nano range CdS depending upon the size of crystallites [112]. When the radius of the crystallite (R_c) < 2 exciton Bohr radius (a_B = 3 nm), the electrons and holes are considered as two confined particles which are bound by an enforced Coulomb interaction. However, when R_c > 4 exciton Bohr radius, the ground exciton is treated as a rigid sphere. These spheres are confined as quasi–particles with quantized motion. In between these two limiting cases, both the electron and hole confinement with their Coulomb interaction are considered [115,116]. The study of the optical band gap behavior and optical constants of CdS semiconductor near the fundamental absorption edge and sub band gap region is important for optoelectronic applications. The accurate knowledge of absorption coefficient, band gap, refractive index and extinction coefficient is indispensable for the design and functioning of optoelectronic devices.

The experimentally observed direct band gap of bulk CdS is 2.42 eV (at wavelength 512 nm) [116]. Pal *et al.* have reported that the band gap and refractive index of the films have a close relationship with the crystallite size [95]. Using the optical measurements, the refractive index of cadmium rich CdS thin films have been reported in the range 2.19 – 2.39 at a wavelength 1000 nm and the band gap values varied from 2.38 eV – 2.41 eV for crystallite size 12.4 nm – 19.9 nm. Using ellipsometric technique, Derin *et al.* have found the refractive index 2.942, extinction coefficient 0.538 at 450 nm and band gap 2.46 eV for CdS film of thickness 63 nm [92]. Mahanty *et al.* reported that as–deposited sulfur deficient CdS films have band gap lower than bulk CdS, while nearly stoichiometric films have the higher band gap 2.43 eV [101].

1.4 Effect of metal additives

The usefulness of the semiconductors for constructing various devices depends mainly upon their conductivity and band gap behavior. These properties of semiconductors can be easily controlled and modified by introducing different type of impurities into their crystal lattice. The addition of impurities provides charge carrying elements in the doped semiconductor. There are two types of doping *i.e.*, *n*–type and *p*–type which introduce negative charge (donor) and positive charge

(acceptor) carriers respectively in the doped semiconductor. The donors create states near the CB while acceptors create states near the VB. Hence, dopants have ability to alter the position of Fermi energy level which results in tailoring the band gap and conduction type (Figure 1.5). The band gap tailoring is mainly concerned with two main components. First, to maintain the size of particles intrinsically which governs the quantum confinement where band gap is inversely related to particle size. Second, introduction of an impurity element in the host semiconductor to decrease or increase the optical band gap.

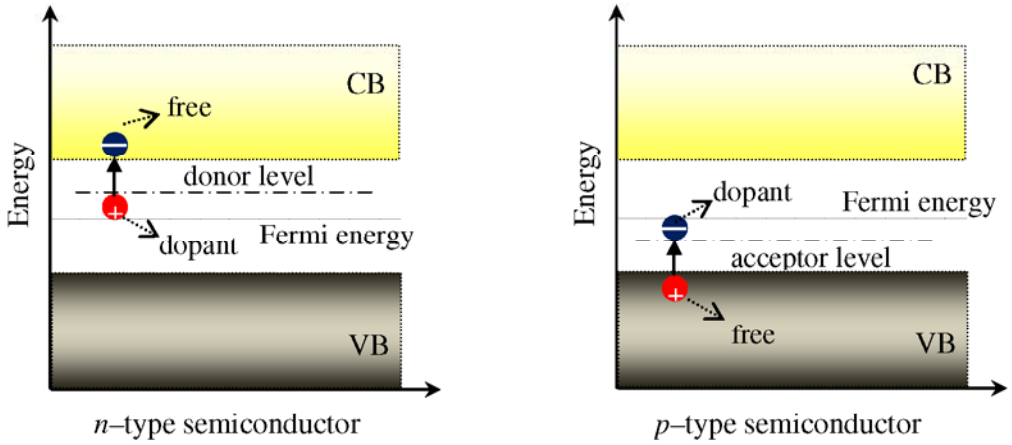

Figure 1.5 Electronic band structure of doped semiconductor (*n*–type and *p*–type)

Sebastian reported *p*–type conductivity in Cu doped CdS thin films deposited by CBD technique [117]. The deposited films exhibit high electrical conductivity in comparison to undoped films. The optical band gap decreased from 2.35 eV – 2.0 eV and electrical conductivity increased from 10^{-9} $\Omega^{-1}cm^{-1}$ – 2 $\Omega^{-1}cm^{-1}$. Kim *et al.* have reported *n*–type conduction in In doped CdS films deposited by thermal evaporation [118]. The band gap, electrical conductivity, carrier concentration and Hall mobility increased up to the optimum In concentration (3×10^{20} cm^{-3}). Wu *et al.* studied the effect of Fe doping in CdS films [119]. $Cd_{1-x}Fe_xS$ film with $x = 0.0025$ showed *n*–type conduction with carrier concentration 3.1×10^{18} cm^{-3} and resistivity 0.25 Ωcm. At $x = 0.14$, the conductivity reversed from *n*–type to *p*–type having carrier concentration 3.8×10^{15} cm^{-3} and resistivity 239.7 Ωcm. Thambidurai *et al.* have prepared hexagonal CdS and Ni, Co, Cr doped CdS nanoparticles of size < 5 nm by co–precipitation technique and found that the band gap of nanoparticles decreased with increase in dopant concentration [120]. Chandermohan *et al.* reported the effect

of TM (Mn, Co, Ni and Fe *via* ion implantation) on structural and optical properties of CdS thin films deposited by thermal evaporation [79]. The pristine as well as TM doped CdS films have WZ structure which grow preferentially along the (*002*) plane. A systematic decrease in the XRD peak intensity with increasing dopant ion fluences has been observed. A reduction in optical band gap is reported with maximum TM doping. Marandi *et al.* reported Mn–doped CdS nanoparticles composed of 65% hexagonal and 35% cubic phases [121]. They illustrated that Mn^{2+} ions act as luminescent activators in CdS host nanocrystals and the excitation can be tuned by QSE while the activator related emission remains unaltered. Recent work on TM doped CdS semiconductor shows new prospective of CdS for technological applications [79,119–123].

1.5 Transition metal doped CdS dilute magnetic semiconductors

TM (magnetic) ions are one of the important categories of dopants in semiconductors. Semiconductors containing magnetic impurities have been studied theoretically and experimentally for several decades [23,124–129]. On the amount of magnetic ions doping, there are three type of semiconductors *i.e.*, magnetic semiconductor, semiconductor and dilute magnetic semiconductor (Figure 1.6) [126].

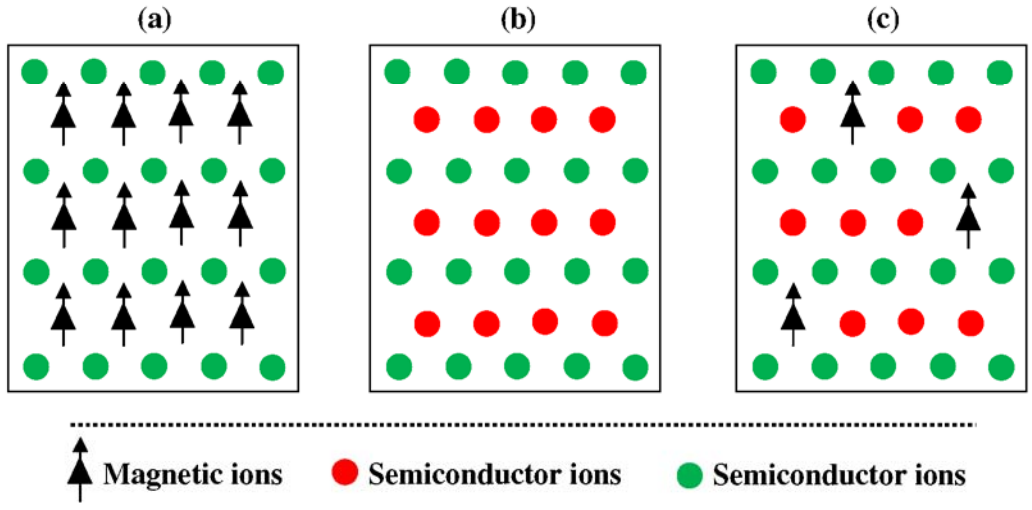

Figure 1.6 (a) Magnetic semiconductor, in which a periodic array of magnetic ions is present; (b) Semiconductor, which contains no magnetic ions; and (c) DMS having fraction of magnetic ions.

In order to achieve desired magnetic character in a semiconductor (Figure 1.6(c)), a controlled amount of magnetic impurity is introduced in its host structure

(Figure 1.6(b)). This category of semiconductor is called dilute magnetic semiconductor (DMS) [126].

DMS are lightly doped semiconducting materials (especially from group II–VI and III–V) wherein a small fraction of the host cations are substituted by TM or rare earth ions. This fractional substitution brings a dramatic change in the magnetic properties of the host semiconductor, while, the semiconducting properties substantially remain unchanged. It has been reported that a fractional TM substitution will not deteriorate the optical and electronic transport properties of the host but simultaneously introduce large magnetic field effects [124]. TM and rare earth metals with partially filled *d* states or *f* states act as magnetic impurities typically characterized by large magnetic moments. The unpaired electrons and unpaired electron spins of these dopants lead to magnetic behavior in DMS. 3*d* TM impurities in semiconductors form deep levels within the band gaps of the host materials and influence the various properties. TM impurities (particularly Cr, Mn, Fe, Co and Ni) incorporated into II–VI semiconductor act as acceptor which tunes various properties like optical, electrical, luminescence, etc. [79,119–123]. In DMS, the tetrahedrally coordinated cations of II–VI semiconductor are randomly replaced by 3*d*–TM ions.

Generally, TM contributes its $4s^2$ electrons to the s–p^3 bonding and can therefore, substitutionally replace the cations of the host semiconductor in the tetrahedral bonding to form a TM^{2+} charge state. Two 4*s* electrons participate in the tetrahedral bonding scheme, whereas the 3*d* electrons remain localized around the TM ion subject to the crystal field [130]. The partially filled 3*d* band of the TM^{2+} ion has an energy gap between the up–spin (↑) occupied states and empty down–spin (↓) states. The TM–*d* bands are hybridized with the host valence bands (Sulfur –*p* bands in CdS). This hybridization gives rise to the exchange interaction between the localized 3*d* spins and the carriers in the host VB. The *s*–band of the CB does not mix with the TM–*d* bands, but, is still influenced by the magnetic ion [131]. In DMS, exchange interaction includes interactions between *s*–electrons in CB, *p*–electrons in VB and *d*–electrons from magnetic ions *i.e.*, double exchange (*sp*–*d*) interaction and interactions between *d*–electrons from magnetic ions *i.e.*, superexchange (*d*–*d*) interaction [124,132,133]. The competition between superexchange and double exchange gives rise to canted ferromagnetic behaviour in DMS [134]. The difference in the number of spin–up and spin–down electrons of TM–*d* bands gives rise to the spontaneous magnetic moment (Figure 1.7) [127,131,135].

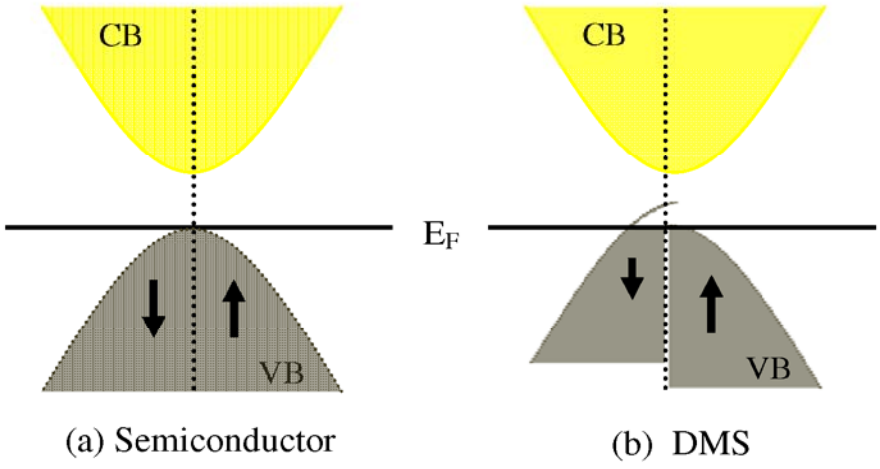

Figure 1.7 A representation of the electronic states available in (a) semiconductor and (b) DMS [135].

The basic mechanisms involved for ferromagnetism in DMS can be explained in terms of superexchange and double exchange interaction. There are various theoretical studies on the origin of the ferromagnetism in DMS [127,131,133,136–138]. Dietl *et al.* referred Ruderman–Kittel–Kasuya–Yosida (RKKY) interaction as the origin of the ferromagnetism [127,131,137,138]. RKKY interactions based on the exchange interaction between the magnetic ion and the CB electrons, were proposed [137,138]. The CB electron gets magnetized in the vicinity of magnetic ion and there is oscillatory decay of polarization. This oscillation results in an indirect superexchange interaction (RKKY) between the two magnetic ions on the nearest or next nearest magnetic neighbors. The interaction may induce a ferromagnetic or antiferromagnetic setting of the moments dependent on the distance between the interacting atoms [127,131]. Although this theory explains some characteristic magnetic and transport properties of the DMS, but, the application of the RKKY theory is questionable because of low carrier density in DMS. Akai stressed the *d*–character of the holes based on his band calculations and invoked a double exchange mechanism [132].

Dietl *et al.* also demonstrated the equivalence of the RKKY and Zener model in the mean field and continuous approximations [127,134,136]. The mean field Zener model describes the direct interaction between *d*–shells of the adjacent TM atoms behind antiferromagnetic configuration of the *d*–shell spins. On the other hand, the indirect coupling of spins through the conduction *p*–electrons tends to align the spins of incomplete *d*–shells in a ferromagnetic order. It is only possible if indirect

superexchange coupling dominates over the *d*–*d* coupling between adjacent *d*–shells. The net behaviour of DMS depends on the resultant of two interactions [127,131,134].

Sato and Yoshida proposed a double exchange mechanism for the carrier–induced ferromagnetism in DMS [23,131,133,138]. They modified the Zener model by proposing that the magnetic ions in different charge states couple with each other by virtual hopping of an extra electron from one ion to the other in the double exchange mechanism. In DMS, if the neighboring TM magnetic moments are in the same direction, the TM–*d* band is widened by the hybridization between the up spin states. Therefore, in the ferromagnetic configuration the band energy can be lowered by introducing carriers in the *d* band. If neighboring TM ions have parallel magnetic moment, then the 3*d* electron in the partially occupied 3*d* orbitals hops to the 3*d* orbitals of the neighboring TM ions. As a result, the *d*–electron lowers its kinetic energy in ferromagnetic state. This is the double exchange (*sp*–*d*) mechanism.

The *sp*–*d* interaction is ferromagnetic (potential exchange) for CB states and is predominantly antiferromagnetic (kinetic exchange) for VB states [133,139]. The *d*–*d* superexchange between the *d*–electrons of the magnetic ions is a short ranged antiferromagnetic interaction and is mediated by the intervening anion [132,133]. The competition between antiferromagnetic superexchange and ferromagnetic double exchange interaction favors the canted ferromagnetic behaviour in DMS [134].

TM doping in the semiconductor governs a new field of research called spintronics aiming to combine magnetic and semiconducting properties into a single material. Spintronics, means spin + electronics, emerged from the dilute magnetic semiconductor which utilize both the spin and the charge of the carriers in a semiconductor. DMS potentially serve as a mean to inject electrons with a definite spin and to control the spin dependent properties in adjacent non–magnetic semiconducting layers [140]. Spintronic materials open up a faster and more efficient mode of information storage and transfer for quantum computation, electronics, magnetotronics and communication [140–146]. The field of spintronics began with the discovery of the giant magnetoresistance (GMR) effect in 1988 (Nobel Prize, 2007) by Grunberg and Fert, in which the resistance of a ferromagnetic/non–magnetic sandwich layer is strongly dependent on magnetic field [144,147]. GMR has found applications in magnetic field sensors in the heads of magnetic recording disks and magnetic random access memory (MRAM) [142–146].

The earliest DMS were II–VI semiconductor alloys like $Zn_{1-x}Mn_xTe$ and $Cd_{1-x}Mn_xTe$ presenting either spin–glass behavior or weak ferromagnetism, with T_c of only few kelvin [124]. Later, research on DMS was inspired by the discovery of spontaneous low temperature ferromagnetism in Mn doped GaAs exhibiting a T_c ~ 110 K [126]. Dietl *et al.* have predicted that 5% Mn–doped CdS would have T_c 200 K on the basis of the bound magnetic polaron model [127]. The current focus of DMS is on the origin and control of magnetism for spin related applications at nanoscale. It has been predicted that DMS can exhibit magnetism below, at and above room temperature by introducing suitable TM ion in the host semiconductor [22,49,124,127,148–150]. CdS DMS are very promising materials for spintronics devices.

The detailed theoretical explanations regarding magnetic behavior of TM doped CdS DMS have been reported [124,127,140,151–155]. There has been ample experimental work on these DMS [145,156–165]. The non–volatile memory and bistable switching effect have been reported in Mn doped CdS films [157]. Delikanli *et al.* have synthesized 10% Mn doped CdS nanorods (diameter ~ 10 nm and length ~ 120 nm) by solution phase chemistry which exhibit strong temperature dependence coercivity and saturation magnetism [159]. Bhattacharyya *et al.* have reported ferromagnetism at room temperature in Carbon–encapsulated CdS:Mn^{2+} (Mn ≤ 4.5 at.%) DMS nanocrystals [145]. Aksu *et al.* have studied the effect of Mn diffusion doping in vacuum deposited CdS films and found that the Mn:CdS films annealed above 580 K have clear hysteresis loops conforming to ferromagnetism [161]. Gao *et al.* have reported room temperature ferromagnetism (T_c ~ 300 K) in DMS $Cd_{0.94}Mn_{0.06}S$ nanowires fabricated by electrochemical method [162]. The fabricated nanowires show their potential as spin polarizer in spintronic devices, such as spin–FET, spin–LED, spin–RTD (resonant tunneling device), etc. [162]. Srivastava *et al.* have reported a temperature dependent magnetic phase transition (T_c = 295 K) in 2% Cr doped CdS DMS QDs [163]. Liu *et al.* have deposited CdFeS granular films embedded with Fe clusters showing tunneling magnetoresistance effects [158]. El–Hagary and Soltan have studied the magnetic properties of hexagonal $Cd_{1-x}Fe_xS$ ($0.05 \leq x \leq 0.2$) DMS nanocrystalline films deposited by electron beam evaporation technique [164]. The temperature and field dependent magnetization measurements have shown ferromagnetism with a T_c at or above room temperature for $0.1 \leq x \leq 0.2$. Murali *et al.* have reported diamagnetism in undoped CdS nanocrystals,

ferromagnetism for 2 at.% and 3 at.% and paramagnetism for 4 at.% and 5 at.% doping of Fe in CdS nanocrystals [166]. Bacaksiz *et al.* have reported spray pyrolysis deposited $Cd_{1-x}Co_xS$ films ($x \leq 0.10$) devoid of ferromagnetism while, the Co diffused CdS films show ferromagnetic loops [160]. Saravanan *et al.* have observed diamagnetism for 2% and 3% and ferromagnetism for 6% Co concentration in CdS nanocrystals synthesized by co–precipitation technique [167]. Kumar *et al.* have reported ferromagnetic behavior in 3% Ni doped CdS nanoparticles and 3% Ni & Cu co–doped CdS nanoparticles [165].

Research on TM doped CdS in various forms (films, nanoparticles, nanowires, QDs etc.) have demonstrated the occurrence of various phenomena *viz.* room temperature ferromagnetism, bistable switching, memory effect, tunneling effect, magneto–photoluminescence, etc. [79,157,162,168]. Thus, CdS DMS may offer an opportunity to integrate optical, electrical and magnetic properties into a single material, which makes it an ideal candidate for future magneto–optical and spintronic applications [79,120,152,157,162].

1.6 Applications of CdS semiconductor

1.6.1 Photoresistors

A light variable resistor works on the fact that resistance is inversely proportional to the amount of light falling on it and is known by many names including photoresistor, photoconductor, or simply the photocell. A typical CdS photocell (Figure 1.8) structure uses an active CdS layer on an insulating or ceramic

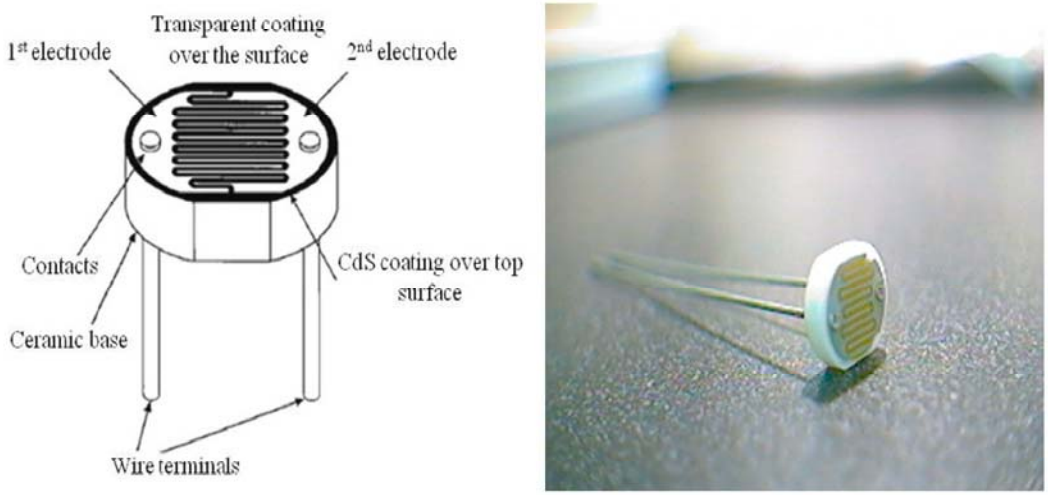

Figure 1.8 Typical construction and picture of a plastic coated CdS photocell [170]

substrate and contacts are then placed on either side of the exposed area. With increasing illumination the resistivity of photocell decreases which allows more photocurrent to flow. CdS photoresistor as a low cost photo sensitive element has been used for many years in photographic light meters as well as in other applications such as smoke, flame and burglar detectors, card readers, lighting control for street lamps, etc. [169,170].

1.6.2 Window layer/Solar Cell

Window or buffer layer is the top layer on the absorber in a solar cell which has high band gap and is transparent to light. The semiconductor compounds having *n*–type conductivity and band gap 2.0 eV – 3.6 eV are suitable as window layer in thin film solar cells. The *n*–type CdS films are good candidate for window layer applications with different *p*–type absorbers such as Cu_2S, $CuInGaS_2$, $CuInGaS_2$, $CuInGaSe_2$, CdTe, etc. [171]. These films play an important role in solar cell performance influencing the electrical properties of the junction and protect the junction against chemical reactions and mechanical damage. CdS layer optimizes the band alignment of the device and builds up a sufficiently wide depletion region that minimizes the tunneling of charge carriers. Hence, it establishes a higher contact potential that allows larger open circuit voltage [171]. The band gap of CdS (bulk, 2.42 eV) allows the solar spectrum to transmit quite freely making it suitable as a window layer [172].

Solar cells based on compound semiconductors (II–VI, III–V and I–III–VI) were first investigated in the 1960s. Practically, solar cell is a *p–n* junction device fabricated by placing two electronically dissimilar materials together with a thin electronic barrier between them to separate charge. (*Solar cell works on photovoltaic principle: Photovoltaic is the direct conversion of light into electricity at the atomic level. The heart of a PV device is the interface between two different types of semiconductor (n–type and p–type). In photovoltaic effect, photon with sufficient energy hits an atom in the interface region, ejects an electron leaving behind a hole and creates a potential difference between n–type and p–type material.*)

For CdS, photovoltaic effect was firstly discovered by Reynolds with an efficiency ~ 5% using sunlight [173]. Fraas and Yale have reviewed four different CdS–based thin film solar cells (CdS/Cu_2S, CdS/CdTe, CdS/InP and CdS/$CuInSe_2$) with conversion efficiencies 7.5%, 12%, 14% and 12% respectively, for terrestrial

applications [174]. CdS buffer layer deposited by CBD for $CuInGaSe_2$ and CdTe solar cell showed conversion efficiency 19.5% and 16.5% respectively [175,176]. The highly efficient ZnO/CdS/$CuInGaSe_2$ solar cell on glass substrate with a record efficiency of 19.9% was developed at national renewable energy laboratory (NREL), USA [177].

1.6.3 Thin film transistors and Schottky diodes

Researchers are taking several different routes to develop inexpensive and flexible integrated circuits. CdS TFTs have been fabricated using CBD method where CdS film acts as a channel layer [86,178]. The surface channel mobility > 1 $cm^2V^{-1}s^{-1}$ shows that the deposited CdS film offer great promise for low temperature processing applications (*e.g.*, in plastic electronics) [178]. Iyyer *et al.* have fabricated a thin film Al/CdS/Al sandwich structure which works as a capacitive type temperature transducer with capacitance 15 nF – 25 nF [179]. Ye *et al.* fabricated Schottky junction PV device on CdS nanobelts using Au as the Schottky contact and In/Au as the ohmic contact [180]. The fabricated device can work as a power source in nano optoelectronic systems. Mereu *et al.* have fabricated thin film – FET by depositing two coplanar electrodes of Au (drain and source) on CBD – CdS film surface and gate contact by Al on the backside of the SiO_2/Si (*n*–type) substrate [181].

1.6.4 Photocatalysts and sensors

Semiconductor based photocatalysis is an efficient tool for destroying organic pollutants in a medium and are efficiently used for the treatment of number of industrial residues. Smyntyna *et al.* have reported the increase or decrease of the electrical conductance in CdS based sensors under the exposure of CO or SO_2 gases for detection of atmospheric pollutants [182]. Urbanczyk *et al.* have investigated sensor properties of physical vapor deposited CdS films towards: NO_2, SO_2, NH_3 and H_2S gases sensitivity, using surface acoustic wave dual delay line systems [183]. Tristao *et al.* have prepared a coupled CdS/TiO_2 photocatalyst for degradation of an organic textile dye (azo dye; Drimaren red) in the presence of artificial UV light [184]. Singh *et al.* have reported CdS/polyacrylamide thick film structure on alumina substrate for sensing liquid petroleum gas (LPG) at room temperature [185]. Zhang *et al.* deposited a cubic phase sheet CdS which acts as visible light driven photocatalyst [186]. This photocatalyst works efficiently for the selective oxidation of saturated

primary C—H bonds in alkyl aromatics, using molecular oxygen as a benign oxidant and benzotrifluoride as the solvent, under ambient conditions [186]. Hong *et al.* have used a simple monolithic film system (CdS/TiO_2) for H_2 production [187]. The repeated unit CdS/TiO_2 structure generated large amount of H_2 without decreased efficiency of any unit [187].

1.6.5 Some other applications

CdS is an effective sensitizer among the various semiconductors such as CdSe, CdTe, $CuInS_2$, InP, etc. [84]. It works as a photoanode in photo electrochemical (PEC) cells because of its suitable band gap, long life time and excellent stability. Dang *et al.* have used vacuum deposited ZnO/CdS bilayer structure in PEC cell as a working electrode and reported that this bilayer electrode has significantly better cell performance than ITO/ZnO film electrode [84].

Benlattar *et al.* deposited 1 mm thick CdS thin film and proposed a model of shield device (Figure 1.9) for radiative cooling application which block solar radiation, but allows complete transmission in the atmospheric window region [188]. The radiative properties of CdS shield *i.e.*, very low IR band reflectance and full transparency across 8 μm – 13 μm, improved optical properties for passive cooling purposes [188].

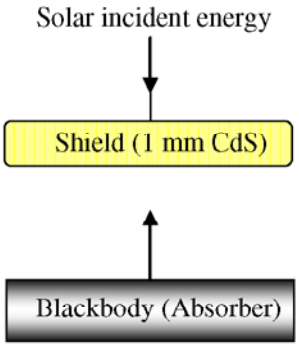

Figure 1.9 Model for the radiative cooling effect

Mitra *et al.* have reported that WZ phase of CdS films is piezoactive and the piezoelectric coupling factor, $|k_c| \geq 0.1$ which is several times greater than that of the crystalline quartz [189]. The strong pyro – and piezo – effects in CdS significantly affect the electric field distribution and device operations. They introduced the pyro – photovoltaic coupling where the photovoltaic effect and the CdS polarization strongly depend on each other. Mondal *et al.* have demonstrated the memory behavior of CdS

nanocomposite using a hybrid inorganic/organic heterostructure sandwiched between oxides or organic layers [76]. Their study indicates that the solution grown CdS nanocomposite and conducting polymer offer possibility in next generation non–volatile flash memory devices for flexible electronics.

1.7 Motive and motif of the present work

Semiconductors are the most successful invented materials of the last century which have revolutionized the science and technology. Group II–VI semiconductors with band gap ranging from 1 eV – 3 eV are suitable for various scientific and technological applications. Among II–VI semiconductors, the CdS is an important semiconductor with attractive optoelectronic and other properties. The quasi–two dimensional structures *i.e.*, nanofilms of these semiconductors exhibit the quantum confinement effect which possess versatile physical and chemical properties in contrast to their bulk counterparts.

The preparation and characterization of semiconductors in nano form is an exciting area of materials research because of size tunable properties. The band gap engineering in semiconductor nanofilms play an essential role towards device fabrication and utilization. The band gap of nanofilms may be modified either by controlling the size of crystallites or by introducing dopant in the host matrix using CBD. CBD has become a popular choice to deposit II–VI films because it is simplest, non–expensive, low temperature, substrate flexible and economical way for large area coating. It may offer a great control over crystallite size, deposition rate and film thickness simply by controlling deposition parameters.

The properties of II–VI semiconductors are extremely sensitive to the presence of impurities and can be controlled by the amount of doping. Fractional TM doping in II–VI semiconductors leads to DMS and may offer novel spin based characteristics along with semiconducting nature. II–VI DMS may increase the storage, detection and processing capabilities of the devices which makes them more compact and multifunctional. In II–VI DMS, TM dopants Ni^{2+} and Co^{2+} have $4s^2 3d^8$ and $4s^2 3d^7$ electron configuration in the neutral state where valence electrons corresponding to the 4*s* orbital and partially filled 3*d* shells lead to the up–spin (↑) occupied states and empty down–spin (↓) states. CdS doped with Ni^{2+} and Co^{2+} may offer an opportunity to integrate optical, electrical and magnetic properties into a single material depending on the random fractional substitution of TM ions.

The present study explores the various properties of the CdS nanofilms. This work is an effort to understand and explore CdS nanofilms deposited *via.* CBD technique. The deposition is optimized with various growth parameters *i.e.*, S/Cd molar ratio and deposition temperature. The quality of the deposited nanofilms is studied with annealing temperature and film thickness. The CdS nanofilms are investigated for their structural, morphological and optical behavior with growth parameters. To explore the DMS behavior, Ni^{2+} and Co^{2+} ion doping in CdS nanofilms is investigated. The phase transition from diamagnetism to para – / ferro – magnetism with dopant concentration is examined with corresponding structural, morphological and optical analysis. This may be useful in tailoring of basic semiconducting properties along with magnetic behavior. The commencement of magnetic behavior in CdS nanofilms may increase their potential towards spintronics.

CHAPTER 2

Experimental and characterization techniques

JAYPEE UNIVERSITY OF INFORMATION TECHNOLOGY
juit
विद्या तत्व ज्योतिसमः

This chapter presents an overview of thin film deposition and characterization techniques. The concept of CBD, its advantages, theory and mechanism involved in film deposition are discussed. The various experimental techniques used for the characterization of deposited nanofilm have been described.

2.1 Nanofilms

A film is a layer/coating of material on a substrate ranging from fraction of a nanometer (monolayer) to several micrometers (multilayers) in thickness [190]. On the basis of thickness (t), films may be categorized as thick film ($t > 1$ μm) and thin film ($t \leq 1$ μm). Any layer/coating of a material with one of its dimensions less than that of the other two is called a thin film. However, if thickness (t) ≤ 100 nm with crystallite size ≤ 100 nm and exhibits quantum size effect (QSE), the film is recognized as nanostructured film or nanofilm. Films of desirable thickness are prepared by depositing material on a supporting substrate. These films may exhibit properties similar to their bulk counterparts or different from them. But, at nanoscale the properties of films change dramatically in comparison to bulk. The characteristics of nanofilms are primarily dominated by two dimensional effects and possess high surface to volume ratio, geometrical control, compactness, single crystal like properties, etc.

Nanofilm allows performance oriented properties (electrical conductivity, magnetism, heat transfer, light absorbance, fluorescence, etc.) to be shown by the surface of the film without affecting the underlying substrate [191]. Nanofilms (both crystalline and amorphous) have immense importance in many technological applications including microelectronic, storage, display and communication devices, wear resistance, surface and decorative coatings, photoconductors, filters, optical coatings (windows, solar cells, etc.), sensors, catalysts, etc. [192,193].

2.1.1 Preparation of substrates for deposition

The substrates required for the uniform deposition of the film should be extremely clean. The contaminated surfaces provide random nucleation sites which promote irregular growth and non–uniform film deposition [194]. Glass is the most commonly used substrate in chemical bath deposition. The surface of glass is reactive towards species in solution. The glass substrates have been cleaned by adopting following steps (i) washed ultrasonically with 1% soap solution (Labolene, Qualigen,

India) (ii) washed ultrasonically with double distilled water, (iii) soaked in chromic acid for 24 hours, (iv) washed with double distilled water several times, (v) ultrasonically degreased with acetone followed by double distilled water, (vi) washed ultrasonically with ethanol, (vii) boiled in double distilled water, (viii) dried in oven and (ix) kept in desiccator.

2.1.2 Film deposition techniques

The act of depositing a thin layer on a surface is called thin film deposition technique. In the last few decades a great research interest is devoted toward the synthesis of films. The nanofilms have further boosted the thin film technology. Film growth is a thermodynamically non–equilibrium process. The film may exhibit drastically different growth behavior under different deposition conditions, *e.g.*, layer by layer growth at low deposition rates, the formation of three dimensional islands at high deposition rates, phase transfer with deposition conditions, etc. The fundamental characteristics of a film strongly depend on the film thickness and deposition technique. Hence, it is essential to choose suitable technique for film deposition. Thin film deposition techniques can be classified in two main groups; physical deposition and chemical deposition (Figure 2.1) [195].

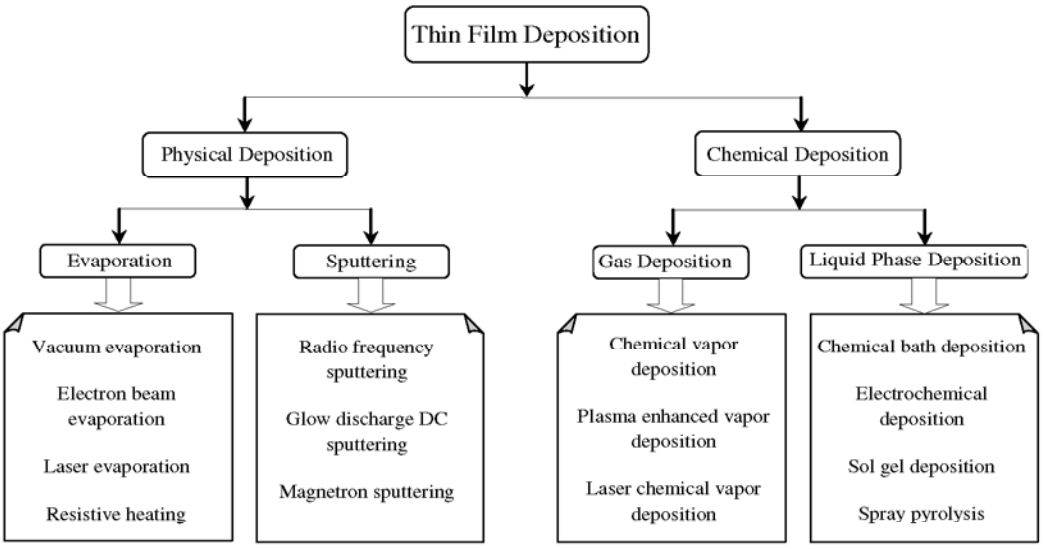

Figure 2.1 Classification of thin film deposition techniques

2.2 Chemical bath deposition technique

Among the various deposition techniques, the chemical bath deposition (CBD) is a low temperature soft route for the growth of films and nanostructures. Chemical

bath deposition or chemical solution deposition (CSD) is based on precipitation or electroless processes in solutions. Liebig in 1835, first described a chemical solution process to deposit silver mirror [196,197]. This technique has been used to deposit films of many compound semiconductors such as oxides, chalcogenides and halides as well as to synthesize nanostructured films [198–201]. It has been used successfully to deposit semiconductor films for more than 130 years but the development in CBD has grown rapidly in the last two decades [198–201]. The continuous research interest in CBD is associated with its remarkable success in depositing effective nanostructured films for PV cells, photocatalysts, optoelectronics, etc., and the existence of size quantization in CBD films [198–202].

2.2.1 Advantages of CBD technique

CBD is the cheapest technique to deposit thin/nano films and to synthesize nanomaterials (nanorods, nanowires etc.). The main advantage of this technique lies in its simple experimental set up (Figure 2.2) consisting of a reaction bath, hot plate magnetic stirrer, substrate holder, *p*H meter and thermometer.

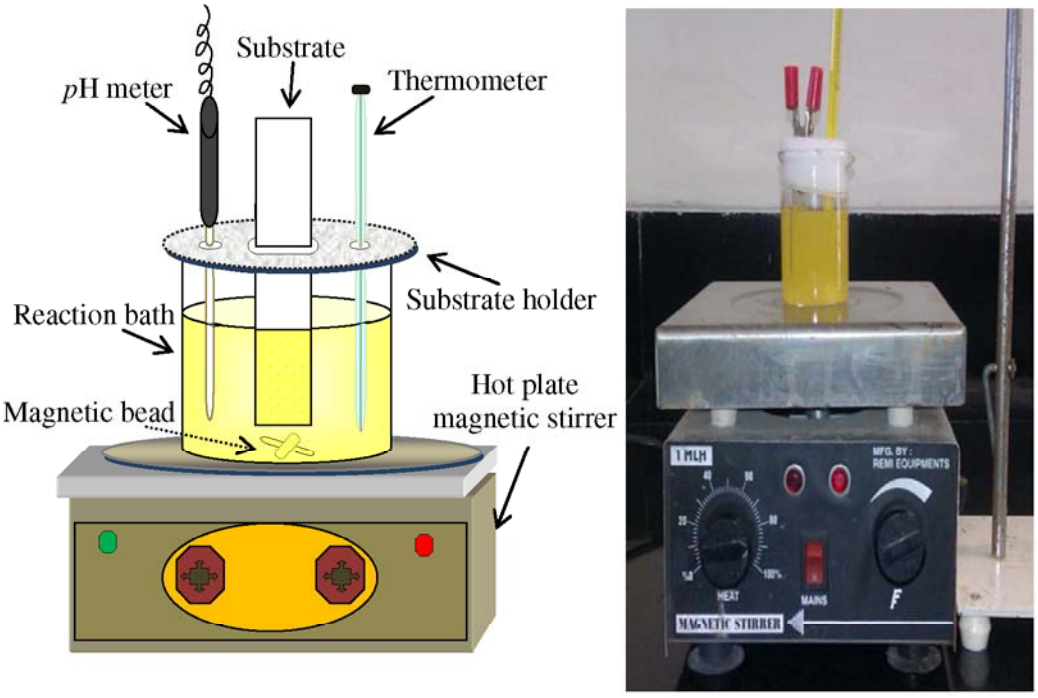

Figure 2.2 Experimental set up for CBD

Other advantages of this technique are

(i) Simple and free from any sophisticated instrumentation.

(ii) Low temperature processing technique (< 373 K) which avoids the oxidation or corrosion of the metallic substrates.

(iii) Scalable technique preferred for large area batch processing or continuous deposition.

(iv) Control film thickness from a few nanometers to micrometer by varying deposition parameters *i.e.*, concentration, temperature, time, *p*H, etc.

(v) Capable of depositing large variety of materials (chalcogenides, oxides, halides, etc.) on different type of substrates (metallic, semiconductor, polymers, etc.) of any size and shape.

(vii) Avoids the vapor phase of the reactants due to dilute solutions rendering minimum toxicity and occupational hazards.

(viii) Yields adherent, uniform, stable and efficient films with good reproducibility.

2.2.2 Reaction mechanisms

The mechanism of CBD can be understood using the concept of solubility product (k_{sp}). Consider an insoluble ionic compound (M_aX_b) in equilibrium with its saturated aqueous solution, then for dissolution

$$M_aX_{b\,(s)} \quad \rightleftharpoons \quad aM^{n+}_{(aq.)} + bX^{m-}_{(aq.)}$$

k_{sp} in terms of concentration of dissolved ions is given by

$$k_{sp} = [M^{n+}]^a[X^{m-}]^b$$

The more soluble is the salt, the greater the ion product and larger is k_{sp}. The values of k_{sp} (at 298 K) for CdS, NiS and CoS are 10^{-28}, 10^{-21} and 10^{-21} respectively [199]. According to the solubility consideration, the precipitation will occur when the product of the concentrations of anions and cations (ionic product (Q_{ip})) exceeds the solubility product (k_{sp}). The film formation in CBD occurs at supersaturation state, where the precipitation is very slow or there is no precipitation even for $Q_{ip} > k_{sp}$.

Generally, CBD process is either an initial homogeneous nucleation in solution or heterogeneous nucleation on the substrate. In CBD, solid material (precipitate/film) is formed indicating thermodynamically unstable bath [38]. O'Brien *et al.* have discussed different possible mechanisms for film formation (Figure 2.3) [38]. In ion by ion (or atom by atom) mechanism, there is condensation of atomic species mainly ions at the reacting surface to form a film (by heterogeneous reaction). In cluster by cluster mechanism, agglomeration of colloids takes place in the solution (by homogeneous reaction) and tends to adsorb at the substrate surface to particulate

films. Practically, both the mechanisms may interact or occur simultaneously leading to film formation where colloids are included in the growing film, *i.e.*, a mixed mechanism [38]. The predominance of one mechanism over another is governed by the extent of heterogeneous and homogeneous nucleation including degree of supersaturation of the solution and catalytic activity of the reacting surface [38].

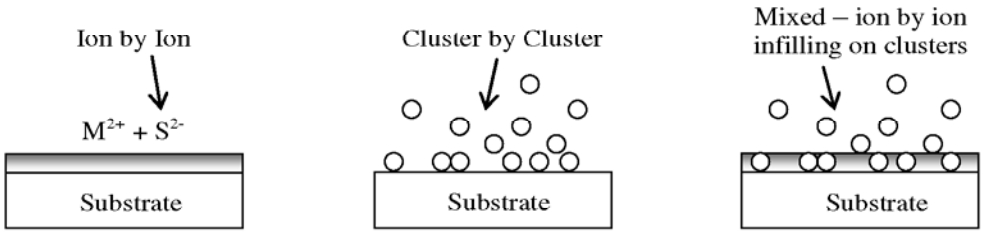

Figure 2.3 Different mechanisms of film formation

Hodes G described four possible reaction mechanisms for CBD process, whose operation depend on the specific processes and reaction parameters, [199] as (i) Simple ion by ion mechanism, (ii) Simple cluster by cluster (hydroxide) mechanism, (iii) Complex decomposition ion by ion mechanism and (iv) Complex decomposition cluster by cluster mechanism

For example, in CdS deposition from thiourea, the first two mechanisms involve free S^{2-} ions, while the last two are based on breaking of a S—C bond and do not involve formation of free chalcogenide. Figure 2.4 shows an experimental process of CdS film formation on the substrate.

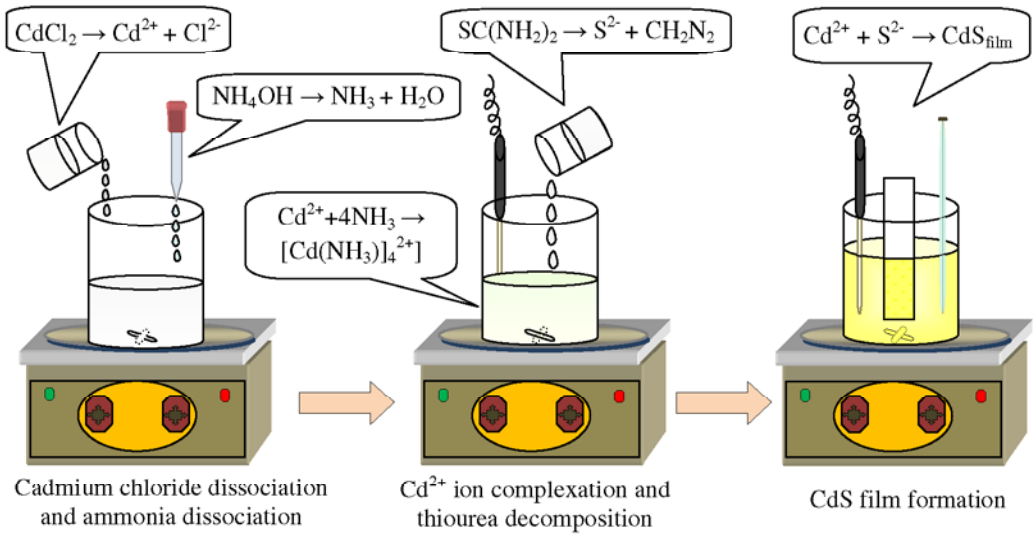

Figure 2.4 Scheme of CdS film formation *via* CBD

2.2.3 Factors influencing the deposition

The main factors influencing the film deposition in CBD are (i) nature and concentration of reactants, (ii) nature and concentration of complexing agent, (iii) deposition temperature, (iv) *p*H, (v) deposition time, (vi) nature and spacing of the substrates, and (vii) rate of stirring.

Nature of the reactants and their concentration influence the composition of the products in the bath and the film [199]. Khallaf *et al*. have reported that with $CdSO_4$, thicker CdS films are formed in comparison to $Cd(CH_3COO)_2$, $CdCl_2$ and CdI_2 as Cd sources [104]. The CdS films deposited using iodides and chlorides of cadmium at a constant *p*H showed a WZ structure with high band gap (2.62 eV) and ZB structure with low band gap (2.45 eV) respectively [203].

Most of the chemical depositions are carried out in alkaline solution and to control the precipitation of metal hydroxides, a complexing agent (or ligand) is used. The complexing agent also reduces the concentration of free metal ions (maintaining the *p*H) to prevent the rapid bulk precipitation of the desired product. Ammonium hydroxide (NH_4OH), triethanolamine (TEA: $C_6H_{15}NO_3$), ethylene diamine–tetra acetate (EDTA: $C_{10}H_{12}N_2O_8$), hydrazine (N_2H_4), ethanolamine (EA: C_2H_7NO), tartric acid (TA: $C_4H_6O_6$), nitrilotriacetic acid (NTA: $C_6H_9NO_6$) and dimethylamine (DMA: C_2H_7N) are few popular complexing agents which are frequently used in CBD [204-207]. Khallaf *et al.* have reported that CdS films deposited on quartz using NTA alone led to porous, non–adherent films while high quality of CdS films have been obtained with the addition of hydrazine [205].

In general, low deposition temperature favors ion by ion growth and slow rate of chemical reaction results in higher terminal thickness. During the growth of films, nuclei are generated on the substrate and grow as discrete grains. At low deposition temperature, surface grains grow too slow to coalesce with each other forming voids and smaller grains [208]. However, high deposition temperature favors the hydroxide cluster mechanism due to the higher hydroxide concentration and lower stability of the complexes [199]. As the deposition temperature increases, the dissociation of the metal–complex increases. The kinetic energy of the reactant ions or molecules increases leading to greater interaction between them. This results in increase or decrease of terminal thickness, depending on the supersaturation of the solution. Moreover, increase in the bath temperature is an effective path to diminish the voids and to promote homogeneous film growth.

The concentration of the various species at the substrate surface is *p*H dependent. Hence, the selection of a suitable *p*H is also important for film formation on the substrate. As the *p*H value of the reaction bath increases, the availability of free metal ions reduce and more stable metal complex is formed. This decreases the rate of chemical reaction leading to higher terminal thickness. In case of CdS deposition, thiourea decomposition is generally faster at higher *p*H. The presence of a solid phase of $Cd(OH)_2$ and its concentration in the solution increase for higher *p*H. Most of the films in CBD are deposited in alkaline solution (*p*H > 7) and very few reports are available in literature to deposit films in acidic solution (*p*H < 7). Boyle *et al.* have deposited CdS thin films from an acidic bath having *p*H between 4.5 – 5.5 and reported that these films show entirely different properties in comparison to the films deposited from alkaline bath [209].

The time of deposition is also significant in thin films deposition. It varies from few minutes to even days depending on reaction rate. The deposition starts with an induction period followed by film growth with deposition time till termination. The film thickness can be controlled by removing the substrate from the reaction bath for desired thickness or by numbers of successive deposition.

The substrates of different nature and shape can be coated uniformly using CBD. The rough substrates are better for film deposition due to large actual surface area of contact and possibility of affixing the initial deposit in pores. The ion exchange between metal ions present in the substrate and the solution may play an essential role in binding the initial deposit. Substrate sensitization is another way to increase the tendency of binding the deposit on the substrate which is commonly done using $SnCl_2$ solution. Various types of metals, glasses and semiconductors are used as substrate in CBD for film deposition. Polymer substrates are used in many applications after the activation treatment which introduces carboxylic groups on a hydrophobic surface.

Stirring is another important factor to dissolve reagents and prepare homogeneous solutions for thin film deposition. During the deposition, the overall effect of stirring is mainly to prevent the deposition of loosely adherent and large aggregates of particles which hinder the film growth by blocking the substrate surface [199].

In this work, CBD technique has been used for CdS nanofilms with varying deposition parameters, *i.e.*, S/Cd molar ratios (0.5, 1, 2, 3, 4 and 5), deposition

temperature (323 K, 333 K, 343 K, 353 K and 363 K) and film thickness (39.7 nm, 65.6 nm, 87.4 nm and 112.5 nm).

2.3 Characterization techniques

The films have been characterized for compositional, morphological, structural, optical and magnetic properties. For this different tools and techniques have been used. In this section, a description of these is presented.

2.3.1 Profilometry

The stylus profilometry is a mechanical technique used for film thickness measurement. The measurements are obtained electromechanically by moving a diamond tipped stylus on the film surface according to the user defined scan length, speed and stylus force. The surface variations cause the stylus to be translated vertically and electrical signals corresponding to the stylus movement are produced as variation in core position of the linear variable differential transformer (LVDT). LVDT scales an *ac* reference signal proportional to the change in position, which in turn is conditioned and converted to a digital format through a high precision analog to digital converter (Figure 2.5) [210]. The film whose thickness has to be measured is deposited with a region masked to create a step on the sample surface. Then the thickness of the sample can be measured by measuring the vertical motion of the stylus over the step.

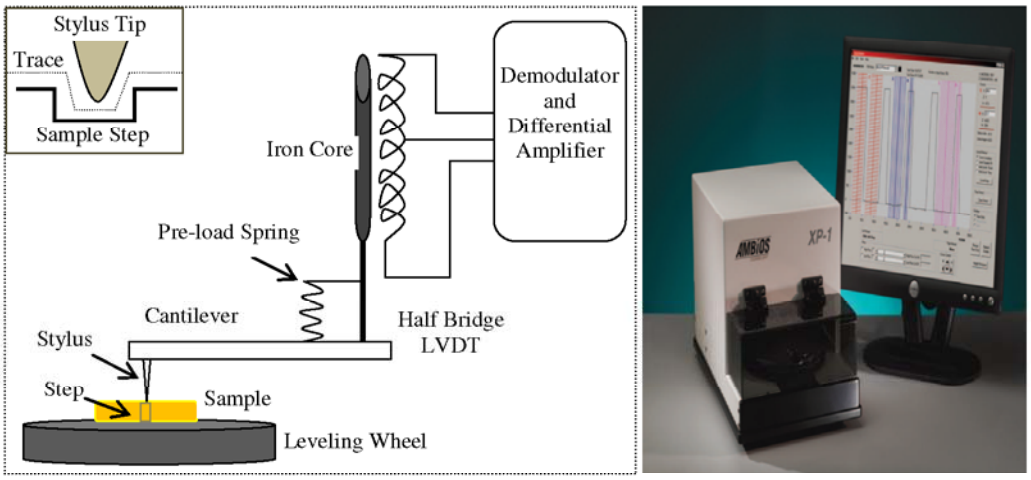

Figure 2.5 Schematic diagram and image of AMBIOS XP–1 stylus profilometer

In the present work, the thickness of deposited nanofilms has been measured using stylus profilometer (AMBIOS XP–1; KU, Kurukshetra), with a precision of

± 0.1 nm having a diamond tipped stylus (radius = 2 μm), scan length (maximum; 30 mm) and programmable stylus force of 0.03 mgf – 10 mgf.

2.3.2 Composition characterization

In the present investigation, the stoichiometry of the deposited films has been analyzed using energy dispersive x–ray spectroscopy.

Energy dispersive x–ray spectroscopy (EDAX/EDS) is an analytical technique used for identifying the elemental composition of the material. It works on the principle that each element has a unique atomic structure allowing specific set of peaks in x–ray spectrum [211]. To stimulate the emission of characteristic x–rays from a sample, a high energy beam of charged particles, is focused into the sample. The bombarding electrons collide with the electrons of an atom of the sample, knocking off some of them and creating holes in place of electrons. The electrons from the outer higher energy shells occupy these holes spontaneously (Figure 2.6). The difference in energy between higher and lower energy shell is released in the form of x–ray. The number and energy of x–rays emitted from the sample are measured by an energy dispersive spectrometer.

The primary components of the EDAX set up includes: the excitation source (electron beam or x–ray beam), the x–ray detector, the pulse processor and the analyzer. The output of this analysis is an EDAX spectrum, which is a plot of how frequently an x–ray is received for each transition (Figure 2.6).

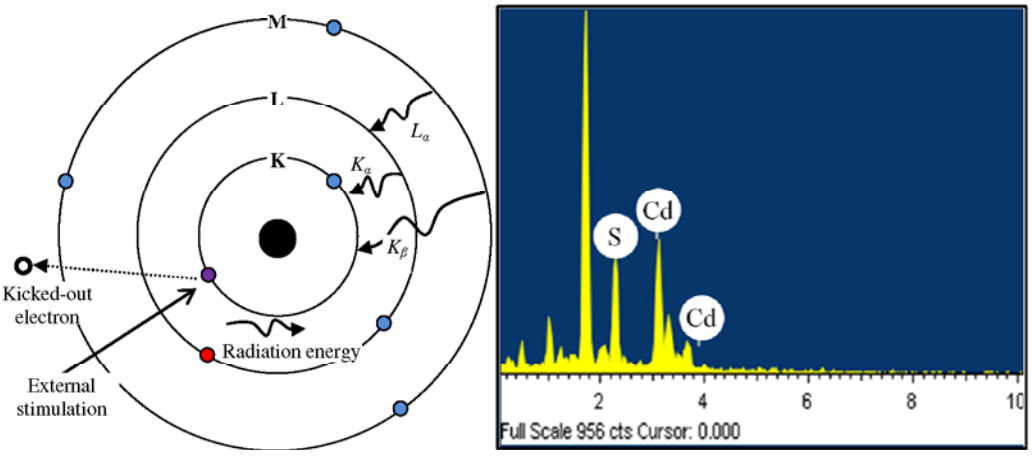

Figure 2.6 Emission of x–rays and example of EDAX spectra for CdS nanofilms

An EDAX spectrum normally displays peaks corresponding to the energy levels for which maximum x–rays are received. These peaks are characteristic of an

atom and therefore, correspond to a single element. An EDAX spectrum also corresponds to the type of x–ray (Figure 2.6).

In the present work, the composition analysis has been performed using EDAX (Bruker, LN2 free X–Flash 4010 SDD detector equipped with QUANTAX 200 software; WIHG, Dehradun).

2.3.3 Morphological characterization

The uniformity and roughness of the film surface play an important role in their opto–electronic behavior. When the surface is rough, the films are less transparent and the grain boundaries affect the opto–electronic properties of such films. The surface morphology of the films is studied using scanning electron microscopy (SEM) and atomic force microscopy (AFM).

2.3.3.1 Scanning electron microscopy

SEM is a powerful and most widely used technique for imaging the surfaces and provides information about the surface morphology. The high resolution of SEM makes it a convenient tool for probing nanostructured materials. SEM is operated at magnifications that are easily adjustable from 10× to over 300,000× with a resolution of 50 nm – 100 nm. The major components of SEM are: electron gun or cathode, electron lenses, sample stage, detectors for all signals of interest, display and data output devices.

SEM works on the principle that accelerated electrons carry significant kinetic energy. This energy is dissipated as variety of signals produced by electron–sample interactions on deceleration of incident electrons [212]. These signals include secondary electrons (that produce SEM images), backscattered electrons, characteristic x–rays (used for elemental analysis), continuum x–rays, visible light and heat. A stream of monochromatic electrons generated by an electron gun is condensed and focused by condenser lens. A set of coils is used to scan the beam and the objective lens focuses the scanning beam on one point at a time on the desired sample area (Figure 2.7). The electron beam hits the sample producing secondary electrons that are collected by a secondary detector, converted to a voltage and amplified. The amplified voltage is applied to the display unit causing variation in the intensity of the light spot. The final image consists of thousands of these spots of varying intensity on the display that correspond to the morphology of the sample.

In SEM analysis, sample preparation is very important depending on the nature of the sample and/or study. In order to avoid the charging of the surface, most of the samples are coated with a thin layer of conducting material, commonly carbon and gold.

An improved version of SEM which is capable of examining the sample without any conductive coating at low vacuum is field emission scanning electron microscopy (FE–SEM).

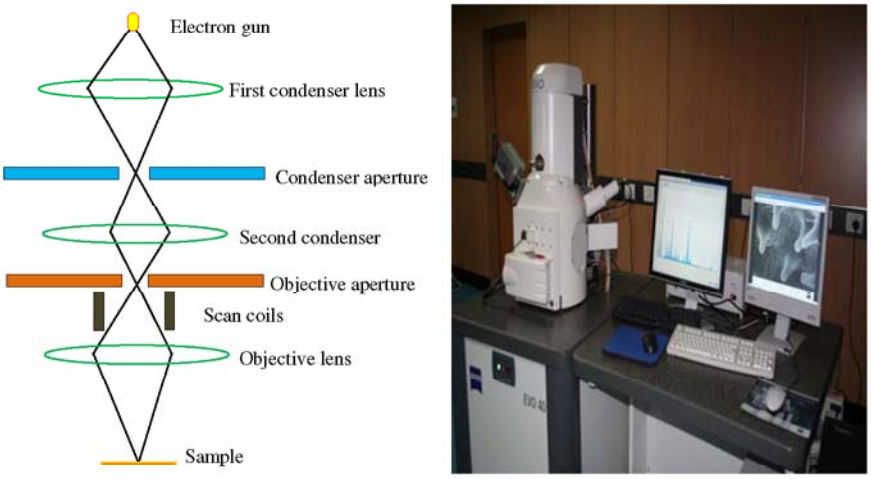

Figure 2.7 Diagram for image formation of a typical SEM and instrumental set up

In the present work, SEM (ZEISS EVO40; WIHG, Dehradun and JEOL/EO JSM–6610; IIT, Ropar) and FE–SEM (HITACHI S–4700; IIT, Roorkee) have been used to study the morphology of nanofilms.

2.3.3.2 Atomic force microscopy

AFM is a high resolution scanning probe microscopy which gives topographical (2 and 3 – dimension (2D & 3D)) images of solid surfaces. AFM is one of the foremost tools for imaging, measuring and manipulating materials at the nanoscale.

A typical AFM has a tip (probe) mounted on a cantilever, a piezoelectric tube scanner, a laser, a position sensitive detector and control electronics as shown in Figure 2.8. AFM is based on measuring the changes in force between the tip and the solid surface by scanning a sharp probe over the surface of the sample. When the tip is brought closer to the surface of the sample, forces between the tip and the sample surface lead to a deflection of the cantilever according to Hooke's law [213,214]. The

force acting on the tip reflects the distance from tip atom to surface atom. Thus, images can be formed by detecting this force. The deflection is measured using a laser spot reflected from the top surface of the cantilever into position sensitive photodiodes and collected by a position sensitive detector (Figure 2.8). To avoid possible collision between the tip and sample surface, a feedback mechanism is often employed to adjust the tip–to–sample distance. Once the deflection of the cantilever has been detected in AFM, it can generate the topographic data sets by operating contact and non–contact mode in one of the two principal modes *viz.* constant–height or constant–force [214].

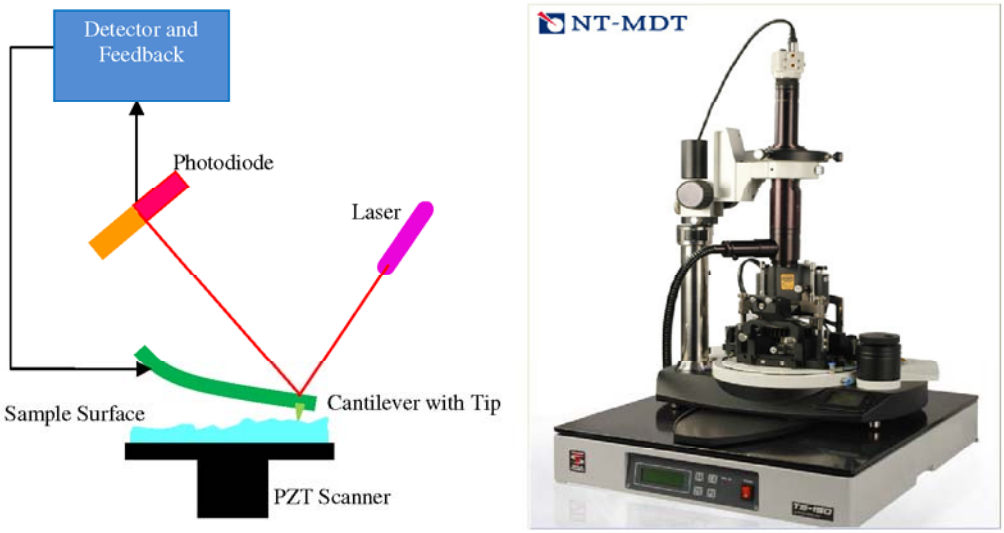

Figure 2.8 Diagram and experimental AFM set up

In the present work, AFM (NTMDT–INTEGRA; IIT, Roorkee) in non–contact mode which has a piezoscanner (55 μm × 55 μm) with vertical *z*–axis resolution of 0.1 nm, a Si_3N_4 cantilever with force constant (1.4 Nm^{-1}) and a probe of radius 20 nm have been used to study the topography of nanofilms.

2.3.4 Structural characterization

X–ray diffraction (XRD) has been used for the structural characterization of the nanofilms.

2.3.4.1 X–ray diffraction

XRD is a versatile and non–destructive technique that reveals crystallographic structure of materials. The distinctive diffraction pattern, fingerprint, of crystalline sample can be used to find information about structural properties.

(a) Principle of x–ray diffraction: Laue discovered that crystalline substances act as three dimensional diffraction gratings for x–ray wavelengths. X–ray diffraction is based on the constructive interference of monochromatic x–rays from a crystalline sample. The interaction of the incident x–rays with the atoms of the sample produce constructive interference at specific angles obeying Bragg's Law (Figure 2.9) [2, 215]. This law relates the wavelength of incident electromagnetic radiation (λ) to the diffraction angle (θ) and the interplanar spacing (d_{hkl}) in a crystalline sample as

$$2d_{hkl}\sin\theta = n\lambda \tag{2.1}$$

where n is unity for first order reflection.

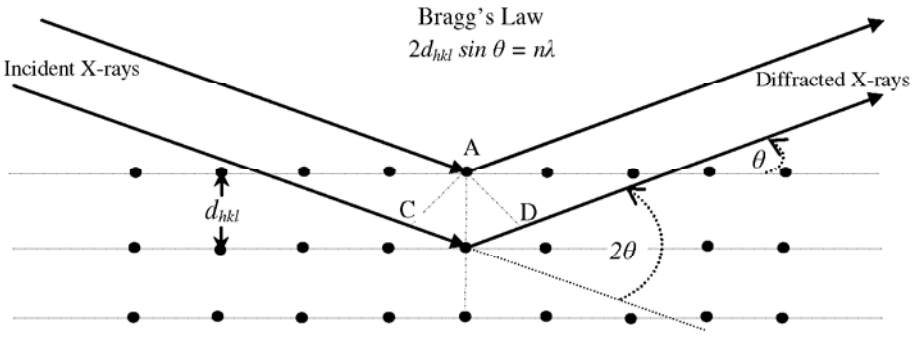

Figure 2.9 Bragg's law, x–ray diffraction from atoms in a crystalline sample

These diffracted x–rays are then detected, processed and counted. The possible diffraction directions of the lattice due to the random orientation of the crystallites in the sample are achieved by scanning the sample for a range of diffraction angles (2θ). The conversion of the diffraction peaks to interplanar spacing allows the identification of the material. This is done by comparing experimental interplanar spacing values with standard reference patterns indexed in Joint Committee on Powder Diffraction Standards (JCPDS) cards or Powder Diffraction File (PDF).

(b) XRD modes: Following two types of XRD modes are used for the structural analysis of the nanofilms.

(i) Bragg–Brentano (θ–2θ) geometry: The commonly used diffraction geometry in commercial diffractometers is the symmetric Bragg–Brentano (*BB*) or θ–2θ geometry [216]. In *BB* geometry, both incident and diffracted beam make same angle with the surface of a flat sample (Figure 2.9). This is achieved by rotating the detector arm with double angular speed in comparison to the rotation of the sample. In θ–2θ

geometry, only the diffraction from crystallographic planes which are parallel to the sample surface is recorded *w.r.t.* different diffraction angles.

(ii) Thin film geometry: In thin film (*TF*) diffraction geometry (Figure 2.10), the beam is incident at a fixed angle (less than 10°) on the sample surface and the detector moves along a circle centered at the sample position [216]. The reflections originate from crystallographic planes that are inclined at different angles *w.r.t.* the thin film surface. The angles of incident beam and diffracted beam *w.r.t.* to the film surface are different leading to asymmetric diffraction geometry. It is known as grazing angle x–ray diffraction (GAXRD).

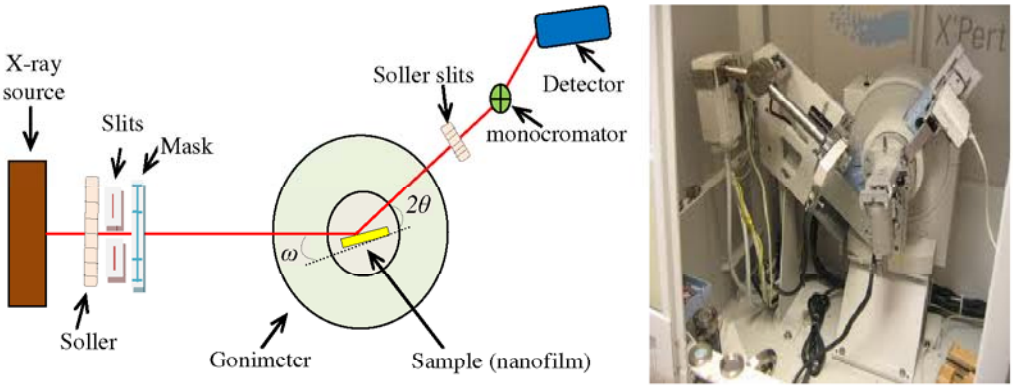

Figure 2.10 XRD thin film geometry

In the present work, XRD measurements have been performed using PANalytical X'Pert PRO x–ray diffractometers for θ–2θ and GAXRD at SAIF, PU, Chandigarh and HPU, Shimla respectively. X–rays are generated from a CuK_α source (λ = 1.5406 Å) with filament current of 30 mA and accelerating voltage of 40 kV.

(c) X–ray diffraction data analysis: The structural parameters such as lattice spacing, crystallite size, crystal phase, lattice constants, strain, dislocations, texture, etc. are strongly dependent on the deposition conditions. The various structural parameters associated with the nanofilms are:

(i) The interplanar spacing: The perpendicular distance between successive parallel planes of the atoms in a crystal *i.e.*, interplanar spacing or *d*–spacing (d_{hkl}) for films has been determined using equation (2.1).

(ii) Lattice parameters: The lattice parameters for different crystallographic systems ('*a*' for cubic, and '*a*' and '*c*' for hexagonal phase structure) depend on the Miller indices (*hkl*) and interplanar spacing (d_{hkl}). An analytical approach [215] is

applied to determine lattice parameters by taking an average of all the observed diffraction peaks using relations

For Cubic structure:

$$\frac{1}{d_{hkl}^2}=\frac{(h^2+k^2+l^2)}{a^2} \tag{2.2}$$

For Hexagonal structure:

$$\frac{1}{d_{hkl}^2}=\frac{4}{3}\frac{(h^2+k^2+l^2)}{a^2}+\frac{l^2}{c^2} \tag{2.3}$$

(iii) Microstrain: Microstrain (ε_{hkl}) is defined as an average value of the lattice spacing fluctuation (∂d_{hkl}) in diffracting volume [215, 216]

$$\varepsilon_{hkl}=\frac{\partial d_{hkl}}{d_{hkl}} \tag{2.4}$$

These fluctuations are assumed to be inside individual grains and between grains. The origin of microstrain in the films is related to lattice misfit that depends upon the growing conditions. The microstrain exists in the nanocrystallites and is calculated directly using Wilson method (*WM*) [217]

$$\varepsilon_{hkl}=\left(\frac{\beta_{hkl}\cot\theta}{4}\right) \tag{2.5}$$

(iv) Dislocation density: A dislocation is an imperfection in a crystal and is associated with mismatch in different parts of the lattice. The dislocation density (ρ_{hkl}) is defined as the length of dislocation lines per unit volume of the crystal and is calculated using Williamson and Smallman's formula [216]

$$\rho_{hkl}=\frac{n}{D_{hkl}^2} \qquad \text{lines /m}^2 \tag{2.6}$$

where D_{hkl} is the average crystallite size from Debye–Scherrer (*DS*) method and $n = 1$ for minimum dislocation density.

(v) Packing factor: Packing factor signifies the efficient atomic layer existence in crystalline domain. The packing factor (p) can be calculated using d_{hkl} and D_{hkl} [218]

$$p=\frac{D_{hkl}}{d_{hkl}} \tag{2.7}$$

(vi) Crystallite size and microstrain from x–ray peak broadening: The size of crystallite approaches nano dimension (< 100 nm), broadening the XRD peaks. The broad profile of XRD peaks is a collective outcome of nano crystallite size, lattice strain and instrumental factor [219]. For broad XRD peaks, there is possibility of an

error, due to inappropriate estimation of background level caused by small grain size effect and microstrain. To eliminate this error, instrumental broadening is corrected using a standard having negligible physical broadening [219,220]. The observed peak broadening ($\beta_{obs.}$) may be represented as

$$\beta_{obs.} = \beta_{inst.} + \beta_{hkl} \tag{2.8}$$

where $\beta_{inst.}$ is the broadening due to instrumental factor (= 0.05 for Si sample) and β_{hkl} is the broadening due to crystallite size and lattice strain. According to *DS* method, the peak broadening (β_D) of a Bragg reflection for nano crystallite is given by [215]

$$\beta_D = \frac{k\lambda}{D_{hkl}\cos\theta_{hkl}} \tag{2.9}$$

where k is the Scherrer's constant and is equal to 0.9 for spherical crystals (ZB/WZ), λ is the wavelength of x–rays, β_D is the angular full width at half maximum (*FWHM*) and θ_{hkl} is the Bragg's angle. Wilson (1949) suggested that the integral peak width (β_s) induced by microstrain individually [217] can be represented as

$$\beta_S = 4\varepsilon_{hkl}\tan\theta_{hkl} \tag{2.10}$$

where ε_{hkl} is microstrain. Williamson and Hall [221] proposed a method (*WH*) of deconvoluting the size and strain broadening by considering the peak width as a function of Bragg diffraction angle. The crystallite size and microstrain are extracted from total broadening (β_{hkl}) using *WH* method as

$$\beta_{hkl} = \beta_D + \beta_S = \frac{k\lambda}{D_{hkl}\cos\theta_{hkl}} + 4\varepsilon_{hkl}\tan\theta_{hkl} \tag{2.11}$$

(vii) Texture coefficient: The physical properties of the materials as well as the performance and reliability of the fabricated devices are strongly influenced by the texture of the material. The texture coefficient (TC_{hkl}) is a measure of the degree of orientation of each reflection in context to randomly oriented sample and is determined from [222]

$$TC_{(hkl)} = \frac{I_{(h_ik_il_i)}}{Io_{(h_ik_il_i)}}\left\{\frac{1}{N}\sum_{i=1}^{N}\frac{I_{(h_ik_il_i)}}{Io_{(h_ik_il_i)}}\right\}^{-1} \tag{2.12}$$

where $I_{(h_ik_il_i)}$ is the diffraction intensity of ($h_ik_il_i$) plane of the sample under investigation, $Io_{(h_ik_il_i)}$ is the intensity of ($h_ik_il_i$) plane of standard sample and N is the number of reflections in the XRD pattern.

2.3.4.2 Transmission electron microscopy

Transmission electron microscopy (TEM) is a high resolution technique which provides information about the morphology, composition and crystallographic structure on nanometer scale. It is useful for the characterization of single crystals, polycrystalline materials, biological specimens, nanostructured materials, etc. In TEM, a specimen is irradiated with an electron beam of uniform current density. Electrons are emitted from an electron gun and illuminate the specimen through a condenser lens and aperture system. The electron intensity distribution behind the specimen is magnified with a three or four stage lens system and viewed on a fluorescent screen or recorded on photographic film or captured electronically (Figure 2.11) [223].

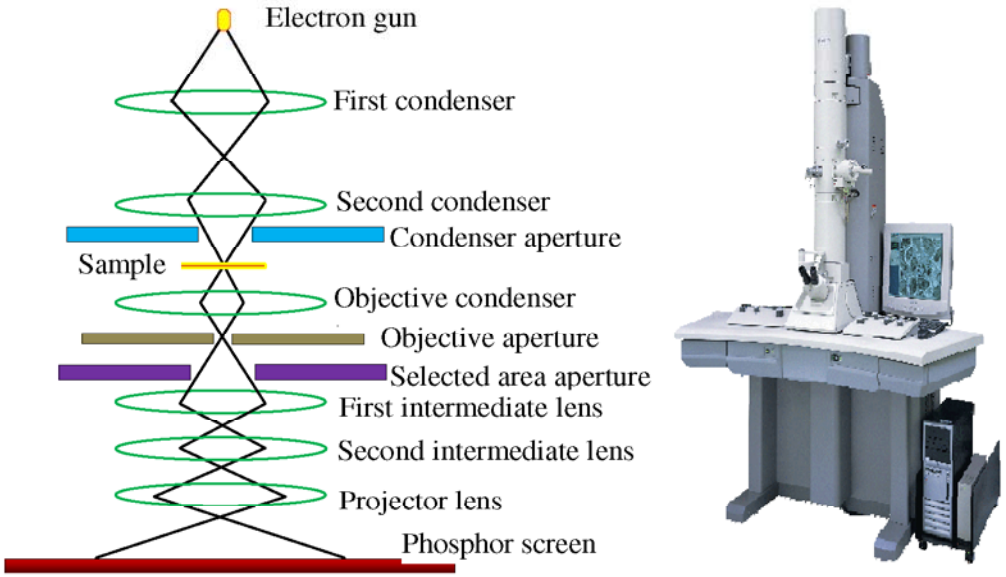

Figure 2.11 Diagram for image formation by typical TEM and instrumental set up

TEM comprises an electron gun, condenser system (lenses and apertures), specimen chamber, objective lens system, projector lens system, image recording system as shown in Figure 2.11. TEM in selected area diffraction (SAD) mode offers a unique capability to determine the crystal structure of individual nanomaterials, such as nanocrystals and nanorods as well as crystal structure of different parts of a sample.

In the present work, TEM images have been obtained (Hitachi: H–7500 TEM microscope equipped with CCD camera at accelerating voltage of 120 kV having maximum magnification 4×10^6 with line to line and point to point resolution of 3 Å and 0.5 Å respectively; SAIF, PU, Chandigarh) by scratching particles from the film

surfaces and making a suspension with small quantity of the obtained particles in ethanol solution. A drop of this suspension has been introduced on Cu/C grid, which is analyzed in TEM.

2.3.4.3 Fourier transform infrared spectroscopy

IR spectroscopy is a spectro–chemical technique of material analysis based on the interaction of IR radiation with matter. It probes the vibrational motion of atoms in a molecule which are influenced by the masses of atoms, their geometrical arrangement and strength of their chemical bonds [224]. When IR radiation interacts with molecules, the bonds between atoms vibrate (stretch, bend, twist, rock, and wag) at some specific frequencies characteristic of the molecule and the functional groups within the molecule. Thus, molecules absorb these frequencies depending on the type and number of functional groups present in the sample. Based on wavenumbers IR spectrum can be divided into three regions as (i) 14000 cm^{-1} – 4000 cm^{-1} Near–IR (NIR), (ii) 4000 cm^{-1} – 400 cm^{-1} Mid–IR (MIR) and (iii) 400 cm^{-1} – 10 cm^{-1} Far–IR (FIR). A typical Fourier transform infrared (FTIR) spectrometer mainly comprises of radiation source, optical path and Michelson interferometer, radiation detector and sample holder (Figure 2.13) [224]

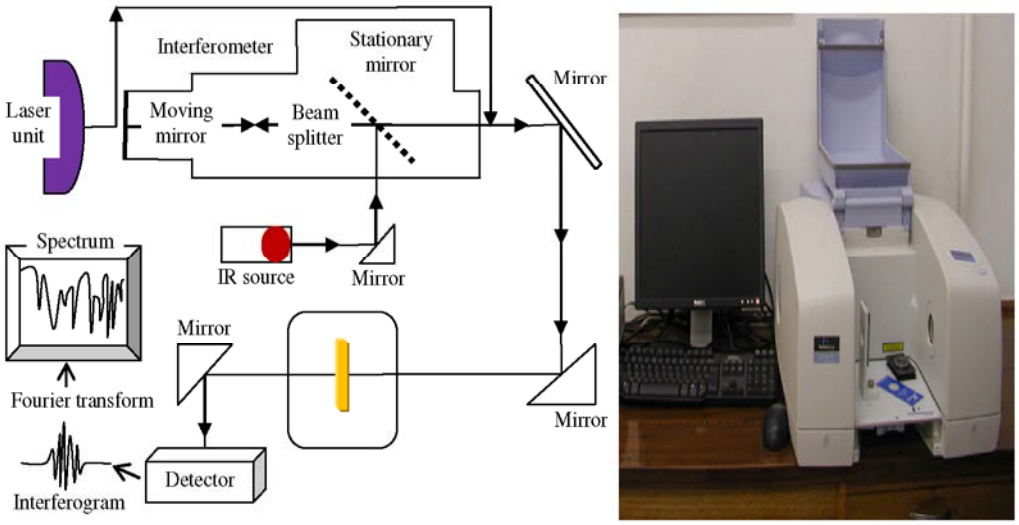

Figure 2.12 Scheme of a typical FTIR spectrometer and experimental set up

In the present work, FTIR measurements have been obtained in the spectral range 4000 cm^{-1} – 400 cm^{-1} at a resolution 1 cm^{-1} (Perkin Elmer 1600 FTIR; SAIF, PU Chandigarh) in $\%T$ mode using KBr pellet technique. The samples for FTIR

measurements were prepared by scraping the film from the substrate. The obtained powder was mixed with KBr powder which then pressed to form a pallet.

2.3.5 Optical characterization

The measurement of absorption coefficient and optical band gap of material are essential for opto–electronic applications. The absorption coefficient for various energies provides information about the optical properties of material.

UV–Vis–NIR spectroscopy is commonly used for the calculation of optical constants. UV–Vis–NIR spectrophotometer measures light intensity (absorbance (*%A*), reflectance (*%R*) and transmittance (*%T*)) as a function of wavelength on interaction of electromagnetic radiation with material [225]. Typically, a double beam spectrophotometer (Figure 2.13) consists, (i) a deuterium arc lamp for the UV spectral range (190 nm – 400 nm) and a tungsten lamp for the visible and IR spectral ranges (300 nm – 2500 nm), (ii) a monochromator composed of a diffraction grating, used to select a single wavelength (iii) a sample holder, (iv) a light detector (a photomultiplier tube, a photodiode for the UV–Vis–NIR range and a PbS cell for the IR range) and (v) a computer to record UV–Vis–NIR spectrum [225].

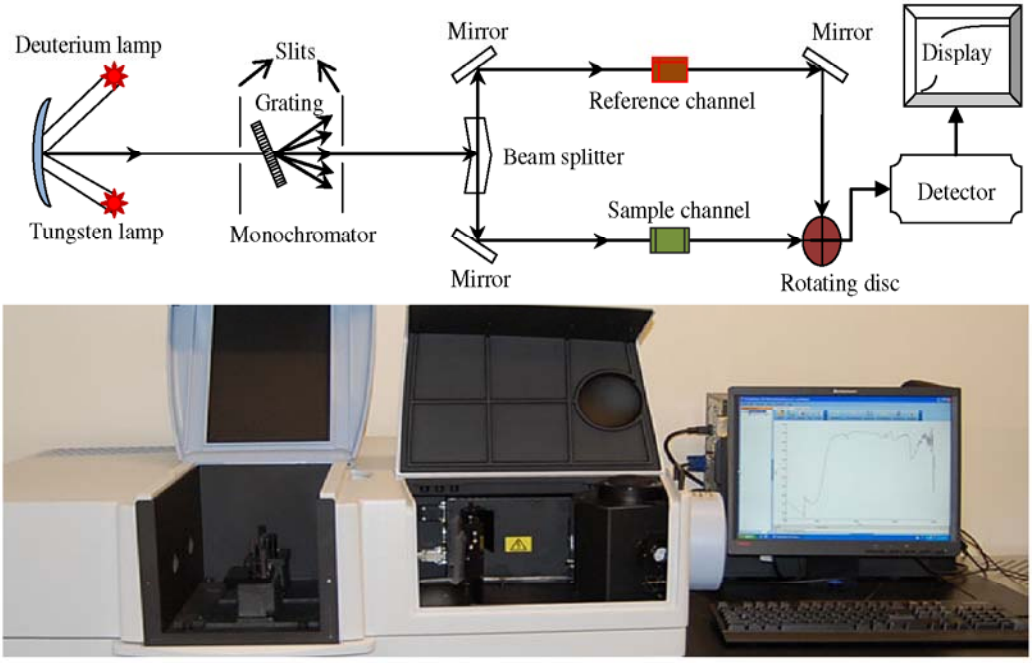

Figure 2.13 Diagram and experimental set up of a double beam spectrophotometer

In the present work, UV–Vis–NIR double beam spectrophotometer (Perkin Elmer: Lambda–750; JUIT, Solan) has been used for *%T* and *%R* measurements.

(a) Optical parameters: No material is fully transparent at all optical wavelengths and hence there will always be some absorption and reflection (Figure 2.14). According to law of conservation of energy, a relation between transmittance (T), absorbance (A) and reflectance (R) is given by

$$A + T + R = 1 \tag{2.13}$$

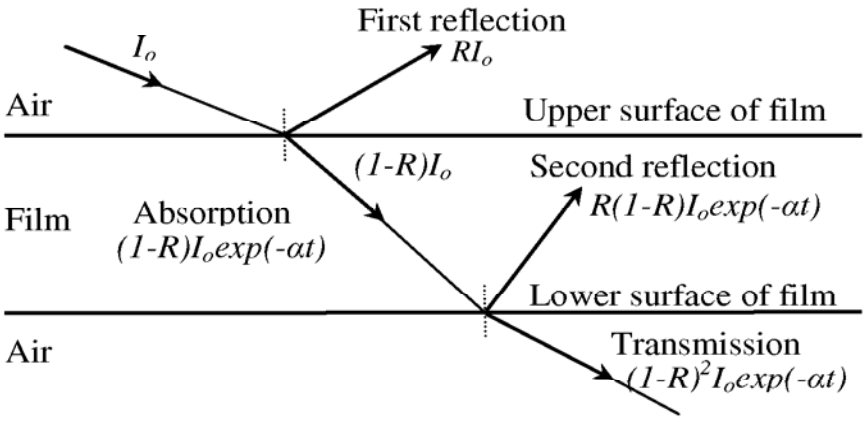

Figure 2.14 Light Interaction with film sample

In $\%T$ mode, the spectrophotometer measures the intensity of light passing through a sample (I_s) and compares it to the incident intensity of light (I_o), according to Lambert–Beer Law [226]

$$I_s = I_o e^{-\alpha t} \tag{2.14}$$

where α is absorption coefficient and t is the sample thickness. The ratio I_s/I_o is called transmittance ($\%T$).

Absorbance (A), a fraction of radiation absorbed inside of the material is [226]

$$A = \log_{10}\left(\frac{I_S}{I_o}\right) = \log_{10}(T) \tag{2.15}$$

The light interaction with film sample is shown in Figure 2.14. The portion internally reflected eventually is transmitted with considerable attenuation and is given by [226]

$$T = \frac{I_S}{I_o} = \frac{(1-R)^2 \exp(-\alpha t)}{(1-R^2)\exp(-2\alpha t)} \tag{2.16}$$

When the product αt is large, the second term in the denominator becomes negligible and transmittance is [226]

$$T = (1-R)^2 \exp(-\alpha t) \tag{2.17}$$

(i) Absorption coefficient: Absorption coefficient measures the spatial decrease in the intensity of a propagating beam due to the progressive conversion into different forms of energy. The absorption coefficient (α) gets influenced by scattering losses and fundamental absorption. In strong absorption region scattering losses can be ignored and absorption coefficient can be calculated from transmittance using [226]

$$\alpha = \frac{1}{t}\ell n\frac{1}{T} \tag{2.18}$$

For non–absorbing films, α is a function of both T and R [227]

$$\alpha = \frac{1}{t}\ell n\left[\frac{(1-R)^2}{2T} + \left(\frac{(1-R)^4}{4T^2} + R^2\right)^{1/2}\right] \tag{2.19}$$

The semiconductor materials exhibit minimal optical absorption for photons with energies smaller than the band gap and high absorption for photons with energies greater than the band gap. As a result, there is a sharp increase in absorption at energies close to the band gap that manifests itself as an absorption edge in the UV–Vis–NIR absorbance spectrum. The fundamental absorption edge is given as

$$E_g = h\nu = \frac{1.241}{\lambda_o} \text{ eV} \tag{2.20}$$

where λ_o is the cut off wavelength. In semiconductors, the optical absorption edge spectra can be generally divided into three distinct regions [228]

(a) For high absorption region ($\alpha \geq 10^4$ cm^{-1}), which involves the optical transition between VB and CB and determines the optical band gap, α is given by Tauc's power law as [229]

$$(\alpha h\nu)^m = B(h\nu - E_g) \tag{2.21}$$

where $h\nu$ is the incident photon energy, B is the slope of Tauc edge called band tailing parameter, E_g is the optical band gap and m is a constant which depends on the nature of transition between the VB and CB. In the above equation, m = 2 for a direct allowed transition, m = 1/2 for an indirect allowed transition, m = 2/3 for a direct forbidden transition and m = 1/3 for an indirect forbidden transition.

(b) For intermediate absorption region or Urbach's exponential tail region (10^1 cm^{-1} < α < 10^4 cm^{-1}) [230], α depends exponentially on photon energy as

$$\alpha(h\nu) = \alpha_o \exp\left(\frac{h\nu - E_o}{E_u}\right); \text{ for } h\nu < E_g \tag{2.22}$$

where α_o and E_o are constants determined from the converging point of $ln(\alpha)$ *vs.* hv plot. E_u or Urbach energy is often interpreted as the width of the tail of localized states in the gap region. The defects and doping perturbs both CB and VB, as a result Fermi level shifts into the parabolic portion of the appropriate band [226].

(c) For weak absorption region ($\alpha < 10^1$ cm^{-1}), the strength and shape of the absorption edge are found to depend on the structural properties of the material.

(ii) Optical band gap: In semiconductors, there is a minimum energy separating the highest filled VB and the lowest empty CB, known as the energy band gap. When this energy gap is calculated using optical methods, then it is called optical band gap (E_g). The optical band gap is the threshold for photons to be absorbed. The band gap of semiconductor is normally evaluated from the measurement of α as a function of the incident photon energy (hv) using equation (2.21) by extrapolating the linear part of plot $(\alpha hv)^m$ *vs.* hv to $(\alpha hv)^m \rightarrow 0$.

(iii) Optical constants: The optical constants (refractive index (n_f) and extinction coefficient (k_f)) of a thin film are determined from the simultaneous measurement of $\%T$ and $\%R$. The refractive index is the ratio of the speed of light in vacuum to the speed of light in medium.

The optical constants (n_f and k_f) can be estimated using $\%R$ as [227]

$$R = \frac{(n_f - 1^2) + {k_f}^2}{(n_f + 1^2) + {k_f}^2} \tag{2.25}$$

For semiconductors and insulators, or for weak absorbing materials, $k_f^2 << (n_f - 1)^2$ so equation (2.25) reduces to

$$R = \frac{(n_f - 1^2)}{(n_f + 1^2)} \tag{2.26}$$

The extinction coefficient (k_f) is the imaginary part of the complex refraction index which relates to light absorption and can be calculated as [226]

$$k_f = \frac{\alpha\lambda}{4\pi} \tag{2.27}$$

(iv) Dielectric constants: A dielectric is actually an insulator and affects how light passes through a materials. A high value of dielectric constant makes the distance inside the material looks longer so that the light travels slowly. The complex dielectric constant (ε^*) is a fundamental intrinsic material property and given by [231]

$$(n^*)^2 = \varepsilon^* \times \mu^* \tag{2.28}$$

where n^* and μ^* are complex refractive index and complex permeability respectively. For non–magnetic materials $\mu^* = 1$. Then above equation can be written as [231]

$$(n^*)^2 = (n_f - i\,k_f)^2 = \varepsilon_r - i\varepsilon_i \tag{2.29}$$

where the real part of dielectric constant (ε_r) is associated with the term that how much it will slow down the speed of light in the material and imaginary part (ε_i) gives that how a dielectric absorbs energy from electric field due to dipole motion. ε_r and ε_i can be calculated as

$$\varepsilon_r = {n_f}^2 - {k_f}^2 \tag{2.30}$$

and

$$\varepsilon_i = 2 n_f k_f \tag{2.31}$$

(v) Optical conductivity: The optical conductivity (σ) describes the response of the material to electromagnetic radiations and can be determined as [226]

$$\sigma = \frac{\alpha n_f c}{4\pi} \tag{2.32}$$

where c is velocity of light, α is absorption coefficient and n_f is refractive index.

2.3.6 Magnetic characterization

There are two types of magnetism in materials *i.e.*, induced magnetism and spontaneous magnetism. In induced magnetism, the material is magnetized only when there is an applied magnetic field *e.g.*, diamagnetism and paramagnetism. However, spontaneous magnetism refers to the ability of a material to retain its magnetic state even in the absence of an applied magnetic field *e.g.*, ferromagnetism, antiferromagnetism and ferrimagnetism. The magnetic properties of the materials can be investigated in terms of magnetic parameters *i.e.* saturation magnetization (M_s), remanent magnetization (M_r) and coercivity (H_c). These can be evaluated from the hysteresis loop (M–H curve) (Figure 2.15) obtained using vibrating sample magnetometer (VSM).

Various types of nano and bulk materials of magnetic nature can be characterized using VSM. The working principle of VSM is based on Faraday's Law of induction, according to which the *e.m.f* induced in an electrical circuit is proportional to the rate of change of magnetic flux linking the circuit [232,233]. VSM measures the change of flux in a coil when a sample with non–zero magnetic moment vibrates near it.

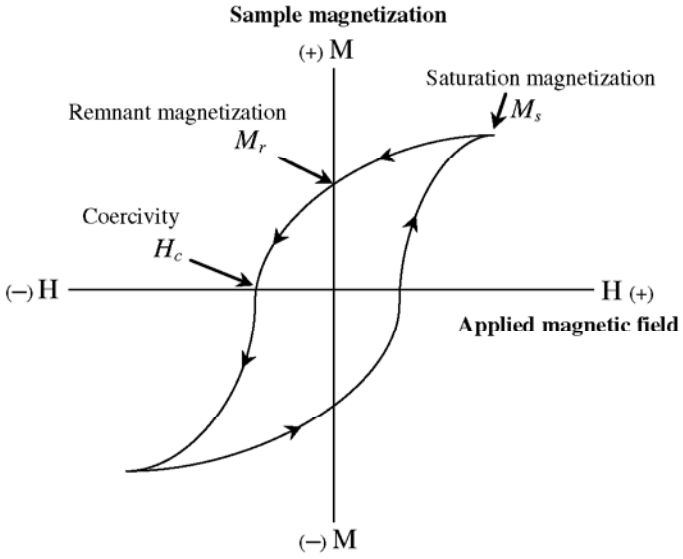

Figure 2.15 *M–H* curve for a magnetic material

When a sample is placed in a uniform magnetic field a dipole moment will be induced. If the sample vibrates with sinusoidal motion a sinusoidal electrical signal can be induced in pickup coils. The signal has the same frequency of vibration and its amplitude will be proportional to the magnetic moment and relative position *w.r.t.* the pickup coils system [234]. The schematic diagram of VSM is shown in Figure 2.16.

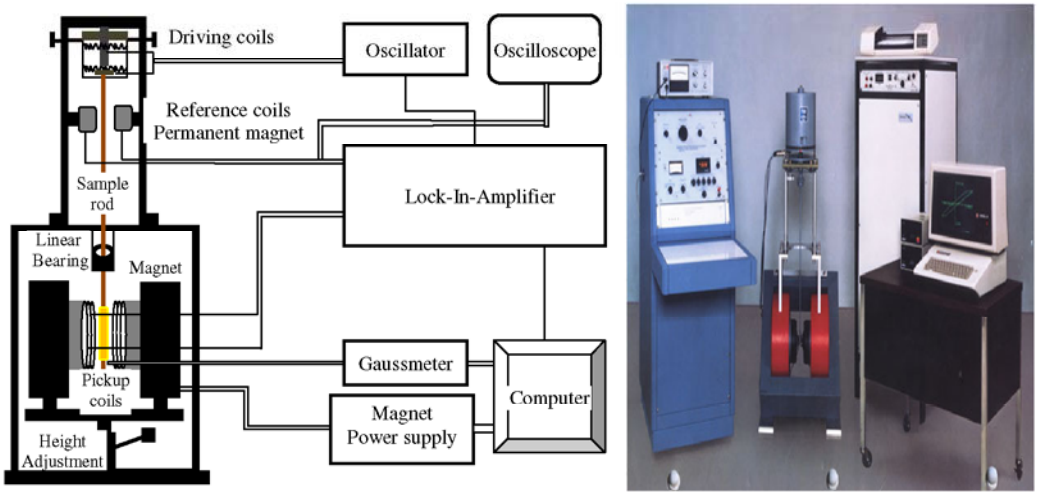

Figure 2.16 Diagram and experimental set up of VSM

In the present work, magnetic measurements (*M–H* curves) have been performed using VSM (EG & G PARC model 155; HPU, Shimla) at room temperature.

CHAPTER 3

CdS nanofilms

- **Suresh Kumar**, Pankaj Sharma and Vineet Sharma, "CdS nanofilms: Synthesis and the role of annealing on structural and optical properties" **Journal of Applied Physics**, 111, 043519 (2012).

- **Suresh Kumar**, Pankaj Sharma and Vineet Sharma, "Structural transition in II-VI nanofilms: Effect of molar ratio on structural, morphological and optical properties" **Journal of Applied Physics**, 111, 113510 (2012).

- **Suresh Kumar**, Santosh Kumar, Pankaj Sharma, Vineet Sharma and S.C. Katyal, "CdS nanofilms: Effect of film thickness on morphology and optical band gap" **Journal of Applied Physics**, 112, 123512 (2012).

- **Suresh Kumar**, Pankaj Sharma and Vineet Sharma, "CdS Nanopowder and Nanofilm: Simultaneous Synthesis and Structural Analysis" **Electronic Materials Letters**, 9, 371 (2013).

- **Suresh Kumar**, Pankaj Sharma and Vineet Sharma, "CdS nanofilms: Effect of deposition temperature on morphology and optical band gap" (2013), **Physica Scripta**, 88, 045603 (2013).

JAYPEE UNIVERSITY OF INFORMATION TECHNOLOGY
juit
विद्या तत्व ज्योतिसमः

The chemical route for the growth of bulk and nanosized materials distinctly involves the process of precipitation of solid phase from solution. A good understanding of the process and bath parameters controlling the precipitation helps to improve the growth of nanostructures. This chapter is divided into the following sections:

3.1 Simultaneous synthesis of CdS nanopowder and nanofilm

3.2 Effect of thermal annealing,

3.3 Effect of molar ratio (S/Cd),

3.4 Effect of deposition temperature, and

3.5 Effect of film thickness

3.1 Simultaneous synthesis of CdS nanopowder and nanofilm

The increasing interest in low dimensional nanostructured materials, such as nanoparticles, nanopowders and nanofilms, is because of their markedly different structure and properties from bulk counterparts [235–238]. Bulk CdS has very high resistivity which decreases for thin film depending on the deposition conditions and techniques. CdS, due to its wide band gap, compact unit cell and electron affinity is preferred for coating over other *p*–type semiconductor materials as optical window layer [239–240]. In addition, CdS provides better lattice matching with various *p*–type absorbers [240].

This section reports the simultaneous synthesis of CdS nanopowder (NP) and nanofilm (NF) by CBD technique. The physical and structural characteristics of nanosized CdS, in powder and film form, obtained under same growth conditions have been studied.

3.1.1 Experimental details

The simultaneous synthesis of CdS nanopowder and nanofilm involves drop wise addition of ammonia solution (2 M) into the aqueous solution of cadmium chloride (0.02 M), till transparent solution is obtained. The complexing agent (ammonia) dissolves white precipitates of $Cd(OH)_2$ under constant stirring and form cadmium–tetra–amine complex ($Cd(NH_3)_4^{2+}$). The solution has been vigorously stirred for 15 min to make it clear and homogeneous. A clean glass substrate with dimensions 35×25×1 mm has been inclined vertically in the solution for film deposition. An aqueous solution of thiourea ($SC(NH_2)_2$: 0.01 M) is added under

vigorous stirring within 30 s. A digital hot plate magnetic stirrer for constant stirring at 300 rpm has been used. The temperature 343 K ± 2 K and *p*H 11 ± 0.1 of the bath have been maintained for a growth period of 45 min. The formation of CdS from the reactant solution shows an initial stage of nucleation. In this stage $Cd(OH)_2$ is formed in the solution and on the substrate as an initial layer. This $Cd(OH)_2$ is chemically converted into $Cd(NH_3)_4^{2+}$ complex reacting with NH_4OH. Finally, $Cd(NH_3)_4^{2+}$ reacts with S^{2-} ions available in the bath from hydrolysis of thiourea. Hence, CdS in the form of layer on the substrate and as powder in solution has been obtained. The former growth mechanism on the substrate surface is *via* ion by ion process and the latter, *i.e.* the agglomeration of colloids in solution *via* cluster by cluster process [241]. The obtained powder and film have been thermally annealed at 573 K ± 5 K for 1 h. CdS nanofilm and nanopowder have been characterized for microstructure and surface morphology using XRD, SEM and AFM.

3.1.2 Results and discussion

3.1.2.1 Structural analysis

The intensity of prominent reflection plane (*002*) has been observed to be high for NF as compared to NP (Figure 3.1.1). The diffused background in XRD pattern of NP (Figure 3.1.1(a)) indicates the formation of weak crystalline structure. This behavior may be due to distorted periodicity of lattice elements and short range order structure of nanocrystallites. However, NF has smooth XRD pattern (Figure 3.1.1(b)). This may be attributed to the high crystallinity and long range order of large crystallites. Both samples have multiple reflection peaks with broad profile reflecting polycrystalline nature and existence of nanocrystallites. Besides, samples exhibit prominent α–CdS (WZ) phase. NP (Figure 3.1.1(a)) has additional peaks at 2θ = 29.82°, 31.84° and 55.14° that correspond to (*200*) reflections of β-CdS, (*002*) reflection of *hcp*–Cd and (*004*)/(*222*) reflection of mixed α and β–CdS phases respectively [242,243]. However, for NF (Figure 3.1.1(b)), only one additional peak at 2θ = 24.03° corresponding to (*222*) of orthorhombic (α–S_8) phase has been observed [243]. Thus, NF has prominent α–CdS structure with high crystallinity in comparison to NP. The growth of NP *via* cluster by cluster process may be attributed to predominant β–CdS phase in comparison to α–CdS structure. In NF, ion by ion growth process may be responsible for enhancing α–CdS structure. The occurrence of *hcp* phase of Cd in NP and orthorhombic α-S_8 in NF may be attributed to the size of

Cd^{2+} and S^{2-} ions. In the later stages of reaction, the large size Cd^{2+} ions are more favored in solution whereas, in the initial stage the tendency for adsorption of small S^{2-} ions on substrate is more in comparison to Cd^{2+} ions. The identical nature of 2θ and (*hkl*) suggests that the growth of CdS in solution and its adsorption on the substrate may have evolved under the same growth parameters. The d_{hkl} values (Table 3.1) are in reasonable agreement with standard d_{hkl} values of CdS [242].

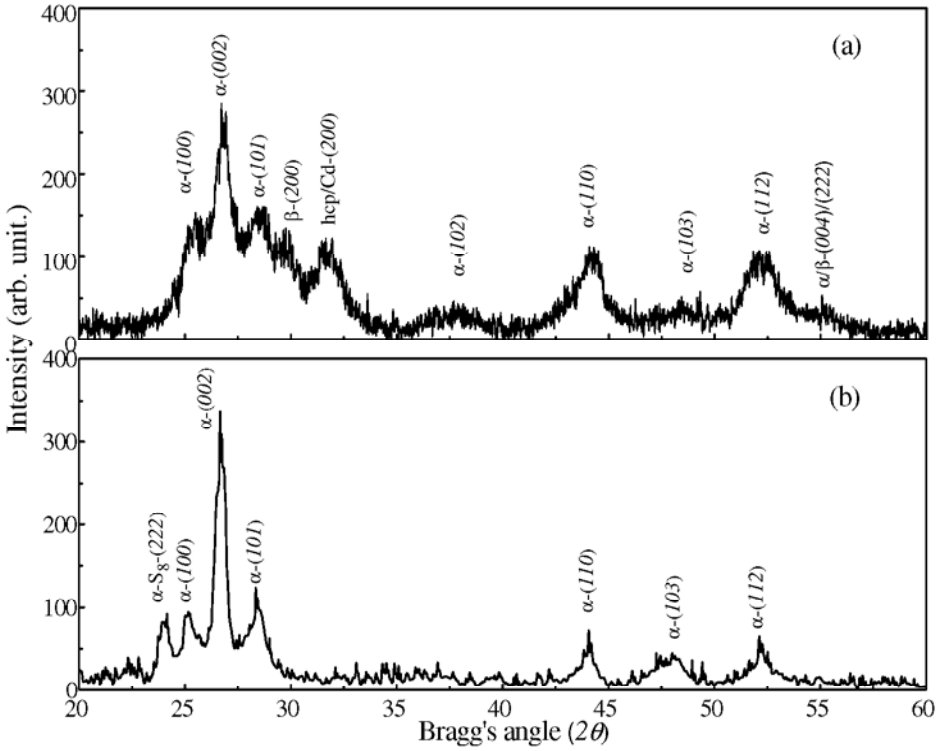

Figure 3.1.1 XRD spectra for (a) NP and (b) NF

The texture coefficient (TC_{hkl}) has been calculated using equation (2.12) [222]. TC_{hkl} values indicate higher degree of orientation for NF in comparison to NP (Table 3.1). For NF, crystallites illustrate strong orientation along (*002*) plane whereas, for NP they are weakly oriented. The evolution of the texture during growth mechanism has a strong effect on the surface features of grains. The initial ion by ion growth on substrate contributes to the strong texture development in comparison to cluster by cluster growth in the residue.

The lattice constants *a* and *c* for WZ structure have been calculated using equation (2.3) (Table 3.1). The *c/a* ratios for both the samples have been found to be slightly greater than the standard value 1.623 for the α–CdS (Table 3.1) [242]. Thus, for NP and NF, lattice deviation along *c*–axis is high. In NP, both lattice constants are

less than standard value [242] which indicates that crystallites in NP are under compressive strain. However, higher c value for NF indicates tensile strain [64]. Generally, the lattice constants of nanoparticles are different from their bulk counterparts due to the existence of defects like surface & interface stress, strain, grain boundaries, dislocations, etc. The deviations in c/a ratios are 0.80% and 0.84% for NP and NF respectively and are < 1% showing a marginal structural distortion.

Table 3.1 The structural parameters: Bragg's angle (2θ), interplanar spacing (d_{hkl}), texture coefficient (TC_{hkl}), lattice constants (a & c), c/a ratio, bond length (L_{Cd-S}), distortion parameter (ε_v), crystallite size (D_{hkl}) by *DS* method, crystallite size (D_v) and microstrain (ε_{hkl}) by *WH* method for NP and NF

Sample	2θ (deg)	d_{hkl} (Å)	TC_{hkl}	a (Å)	c (Å)	c/a	L_{Cd-S} (Å)	ε_v	D_{hkl} (nm)	D_v (nm)	ε_{hkl} $\times 10^{-3}$
NP	26.75	3.330	1.27	4.083	6.659	1.6311	2.499	-0.034	7.53	5.03	-1.38
NF	26.68	3.339	3.54	4.093	6.677	1.6314	2.506	-0.026	14.24	23.16	7.70

In a real crystal, the WZ structure deviates from the ideal arrangement due to changing c/a axial ratio and internal parameter (u_{ip}) [244] (for NP and NF, u_{ip} = 0.375). The parameter u_{ip} signifies the shift of anionic sub–lattice *w.r.t.* cationic sub–lattice in z–direction and is given as [244]

$$u_{ip} = \frac{1}{3}\left(\frac{a^2}{c^2}\right) + \left(\frac{1}{4}\right) \tag{3.1.1}$$

The structural deviation due to change in c/a ratio is responsible for contraction or expansion of lattice and hence, the bond length (L_{Cd-S}) (Table 3.1), which has been calculated using [244]

$$L_{Cd-S} = \sqrt{\left(\frac{a^2}{3}\right) + \left(\frac{1}{2} - u_{ip}\right)^2 c^2} \tag{3.1.2}$$

The lattice deviation in terms of distortion parameter (ε_v) (Table 3.1) has been calculated from [244]

$$\varepsilon_v = \left(a^2 c - a_o^2 c_o\right) / a_o^2 c_o \tag{3.1.3}$$

where a_o and c_o are the standard lattice constants [242]. The unit cell volume (for NP and NF = 96.133 Å^3 and 96.873 Å^3 respectively), u_{ip} and L_{Cd-S} are less than their respective standard values [242]. Moreover, the negative value of ε_v and higher

density (for NP = 4.992 g/cc and NF = 4.954 g/cc) *w.r.t.* standard CdS [242] directly indicate that there may be contraction of lattice. In nanocrystalline materials, the smaller surface energy of the nanocrystallites causes size contraction and solidification by elastic distortion of lattice [245]. The correlated arrangement in nanoparticles may also be responsible for the random lattice disorder and bond length contraction. This contracted bond length stiffens the nanoparticles leading to high density [246].

The crystallite size (D_{hkl}) has been calculated using *DS* method, equation (2.9) (Table 3.1). Additionally, *WH* method (equation (2.11)) has been used to get a fair idea of full width half maxima (*FWHM*) for diffraction peaks. The crystallite size (D_v) and microstrain (ε_{hkl}) have been calculated for NP and NF from the linear fit of *WH* plot (Figure 3.1.2) (Table 3.1).

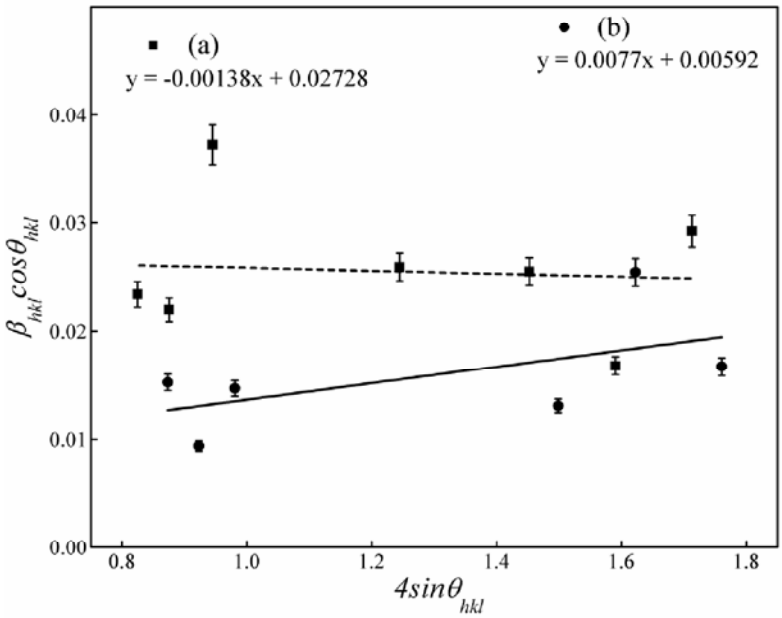

Figure 3.1.2 *WH* plot for (a) NP and (b) NF

The small negative value of microstrain for NP indicates nanocrystallites under compressive strain leading to compact shrank lattice while the high positive strain value for NF indicates that film structure is under tensile strain [247].

3.1.2.2 Morphological analysis

SEM micrograph of NP (Figure 3.1.3(a)) consists of nanocrystallites and their aggregates. The formation of compact agglomerates and flocks of crystallites in NP may be due to homogeneous precipitation of CdS. The nanocrystallites are embedded

densely in these clusters. SEM micrograph of NF (Figure 3.1.3(b)) shows the surface of film to be homogeneous and uniformly spread, devoid of pores and cracks.

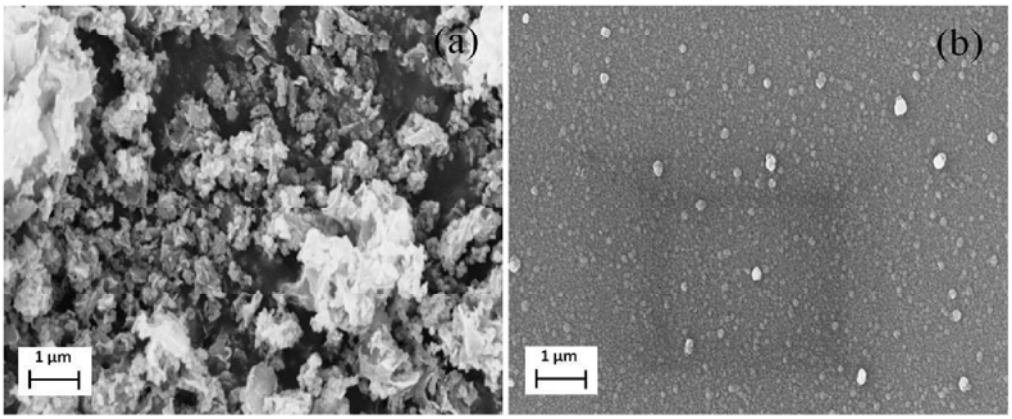

Figure 3.1.3 SEM micrographs for (a) NP and (b) NF

The roughness (R_{rms}) from AFM images for NF has been observed to be 6.80 nm (Figure 3.1.4(a)). The highly organized and densely packed nano CdS facets have been observed. CdS particles grow in columnar structure parallel to the plane of substrate (Figure 3.1.4(b)) indicating the growth of hexagonal–WZ structure with (*002*) orientation. Hence, few grain boundaries are present in NF to disrupt the flow of charge carriers. This may be explored for application of NF in window layers.

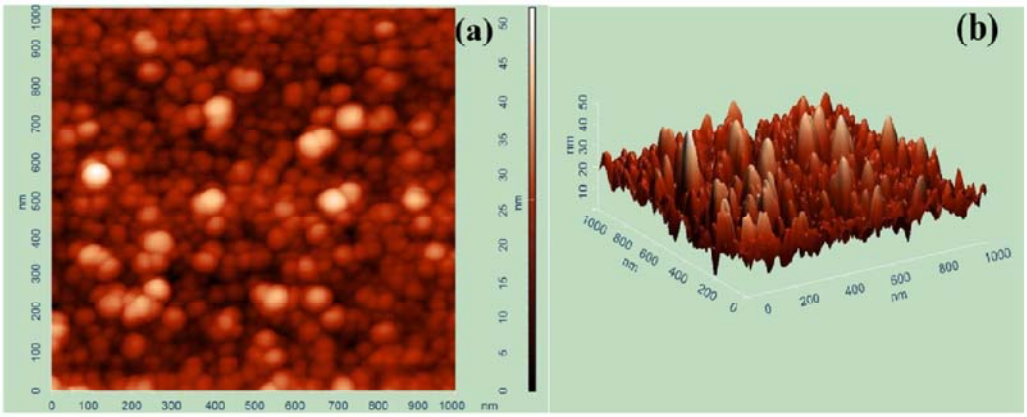

Figure 3.1.4 (a) 2D and (b) 3D AFM images for NF

3.2 Effect of thermal annealing

Annealing is a process of heating the material for a suitable temperature, kept at that temperature for a period of time and then cooling it slowly. During annealing (at high temperature) atoms of the material have high energies which provide freedom to restructure themselves. As the temperature is reduced the energy of these atoms

decreases, until a state of minimum energy is achieved. Annealing is applied to relieve the internal strain and stress of the films after they have been deposited. Annealing occurs by the diffusion of atoms within films, advances them towards equilibrium state, breaking bonds and redistributing the dislocations [248,249]. Annealing treatment affects the surface morphology, grain distribution and crystallization of films. In general, as–deposited films show poor crystallinity and crystal imperfections. Annealing plays an important role in reducing the crystal imperfections and strains, thus, enhancing the crystallinity of films at temperatures higher than the deposition temperature [249–251]. It also improves the quality of the films and on impurity addition, ensures the uniform distribution [249,250]. Practically, thermal treatments are given during the fabrication of several kinds of optoelectronic devices [249–253].

In this section, the effect of annealing at different temperatures (373 K, 473 K, 573 K and 673 K) on the structure, morphology and optical properties of CdS nanofilms has been studied.

3.2.1 Experimental details

CdS nanofilms have been deposited using procedure given in section 3.1.1. The reaction bath has been wrapped tightly to minimize the evaporation of ammonia. The nanofilm has been deposited for a period of 1 h. During the chemical reaction mechanism, large amount of gas bubbles have been formed in the bath. In order to eliminate the gas bubble formation, non–ionic surfactant TX–100 (5%) dissolved in double distilled water (Millipore, 15 MΩcm) has been used. TX–100 completely eliminates the gas bubbles, thus, leading to a good quality of films.

The chemical reactions leading to the film formation may be represented as:
The cadmium tetra–amine complex ion decomposition

$$[Cd(NH_3)_4^{2+}] \rightleftharpoons Cd^{2+} + 4NH_3$$

The hydrolysis of thiourea in alkaline solution with S^{2-} ions generation

$$SC(NH_2)_2 + 2OH^- \rightarrow CH_2N_2 + 2H_2O + S^{2-}$$

The overall reaction is as follows

$$[Cd(NH_3)_4^{2+}] + SC(NH_2)_2 + 2OH^- \rightarrow CdS_{film} + CN_2H_2 + 4NH_3 + 2H_2O$$

The deposition occurs when the ionic product of Cd^{2+} and S^{2-} ions exceeds the solubility product of CdS (10^{-27}) [199].

The obtained films have been observed to be pale yellow, uniform and with a good adherence to the substrate. The obtained films have been thermally annealed at temperatures 373 K, 473 K, 573 K and 673 K ± 5 K for 1 h. Thickness, structural, morphological, compositional and optical measurements have been carried out on these films using stylus profilometer, XRD, SEM, EDAX and UV–Vis–NIR spectrophotometer respectively.

3.2.2 Results and discussion

The thickness of the sample Z0 (as–deposited), annealed samples Z1 (373 K), Z2 (473 K), Z3 (573 K) and Z4 (673 K) has been calculated to be 40 nm, 41 nm, 38 nm, 40 nm and 41 nm ± 0.1 nm respectively.

3.2.2.1 Structural analysis

The films annealed at different temperatures show single broad XRD peak indicating nanocrystalline nature (Figure 3.2.1). The 2θ values for peak position of

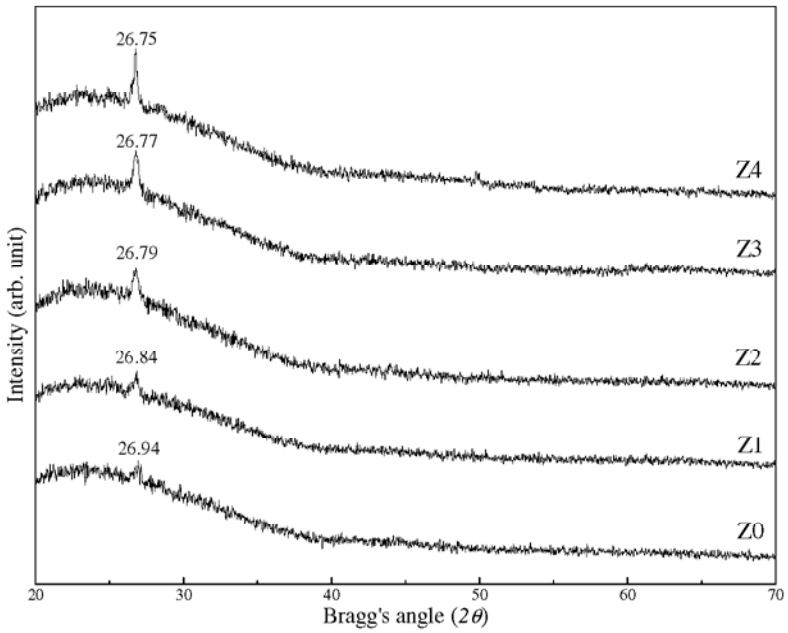

Figure 3.2.1 XRD spectra for as–deposited film (Z0), annealed films (Z1, Z2, Z3 and Z4) CdS nanofilms

films (Table 3.2) have been assigned to the reflection (*111*) of cubic–ZB structure [101]. The preferred (*111*) orientation may be due to the controlled nucleation occurring in the film growth process and reflects the slow growth rate of the film deposition [106]. The sample Z0 has a peak at $2\theta = 26.94°$ with small intensity, which

indicates low crystallinity, while its broader width reflects the nanocrystalline nature. The diffraction peaks have been observed to be more sharp and intense with increasing annealing temperature while their width goes on narrowing enhancing the crystallite size.

The full width half maxima (*FWHM*) values and peak position change with annealing temperature. The *FWHM* values give an estimate of the crystalline quality of the films. The smaller *FWHM* value indicates the better crystallinity of the film. For sample Z0, its value is maximum (0.5722). The *FWHM* values decrease from 0.5425 – 0.3319 with annealing temperature from 373 K – 673 K. At 673 K, the film shows sharp and intense peak with a small *FWHM* indicating high crystallization with a larger crystallite size. The XRD peaks of reflection (*111*) shift towards the lower scattering angle (2θ) with increase in annealing temperature. This shift may be due to an increase in crystallite size, interplanar spacing, while the dislocation densities & microstrain in the film decreases (Table 3.2).

The crystallite size (D_{hkl}) for CdS films calculated using *DS* formula (equation (2.9)) has been given in Table 3.2. The film Z4 has maximum D_{hkl}. The crystallite size increases with the increasing annealing temperature. The grain growth is 7%, 18%, 29% and 72% for films Z1, Z2, Z3 and Z4 respectively. With increasing annealing temperature the grain growth increases. This may be due to coalescence responsible for reorganization of crystallites, leading to densification of film and reduction of voids and strains.

The interplanar spacing (d_{hkl}) and lattice constant (a) for samples have been determined using equations (2.1) and (2.2) respectively. These values have been found to increase with annealing (Table 3.2). The increase in the interplanar spacing and lattice parameter leads to the crystallite growth from 14.12 nm to 24.33 nm. All films have lower lattice parameter in comparison to powder sample (5.82 Å) [242]. Vigil *et al.* and Morales *et al.* have also observed an increase in d_{hkl} and a values with increasing annealing temperature [254,255].

The microstrain (ε_{hkl}) and dislocation density (ρ_{hkl}) have been evaluated from equations (2.5) and (2.6) respectively and are listed in Table 3.2. As the annealing temperature increases, micro strain and dislocation density of the films decreases. This may be due to dominant re–crystallization and reorganization of crystallites which reduce the lattice mismatch of the films [256].

Table 3.2 Values of Bragg's angle (2θ), crystallite size (D_{hkl}), interplanar spacing (d_{hkl}), lattice constant (a), microstrain (ε_{hkl}), dislocation density (ρ_{hkl}), absorption coefficient (α) and optical band gap (E_g) for CdS nanofilms for as–deposited film (Z0) and annealed films (Z1, Z2, Z3 and Z4)

Film	2θ	D_{hkl} (nm)	d_{hkl} (Å)	a (Å)	ε_{hkl} $\times10^{-3}$	ρ_{hkl} $\times10^{15}$ (line/m²)	α $\times10^{5}$ (cm^{-1})	E_g ±0.01 (eV)
Z0	26.94	14.12	3.306	5.727	10.04	5.02	1.37	2.81
Z1	26.84	14.89	3.319	5.748	9.92	4.51	1.59	2.76
Z2	26.79	16.96	3.325	5.759	8.72	3.48	1.68	2.49
Z3	26.77	17.61	3.327	5.763	8.41	3.23	1.71	2.46
Z4	26.75	24.33	3.329	5.766	6.09	1.69	2.17	2.42

3.2.2.2 Morphological analysis

SEM micrographs of nanofilms show homogeneous and continuous surface (Figure 3.2.2). The surface morphology of all films is smooth, uniform without pinholes and cracks. This may be due to the influence of TX–100 which acts as reducing agent and shows low solid–water interfacial tension. The adsorption of TX–100 on glass substrate provides better wetting property and eliminates gas bubbles in the bath [257]. Small nanosized grains with grain boundaries are distributed uniformly. There is change in film surface morphology with annealing. The annealing enhances the tendency of coalescence of small crystallites into larger grains and shows densification of the particles. After annealing, the CdS nanofilms show denser microstructure. These results are in good agreement with XRD results which show that the grain size increases with annealing temperature.

The quantitative elemental analysis of the films carried out using the EDAX is shown in Figure 3.2.3 together with S/Cd elemental ratio (in at. %). EDAX spectra confirm Cd and S elements. EDAX spectrum also shows the signal of other elements such as Si, Na, Ca, Mg, Al, K and O. These elements are observed due to their presence in the glass substrate (Figure 3.2.2). On comparing the EDAX of uncoated glass substrate with the coated sample, the actual elemental composition of the CdS nanofilms has been determined and found to be stoichiometric in at.%. However, sulfur content goes on decreasing with increase in annealing temperature (Figure 3.2.3).

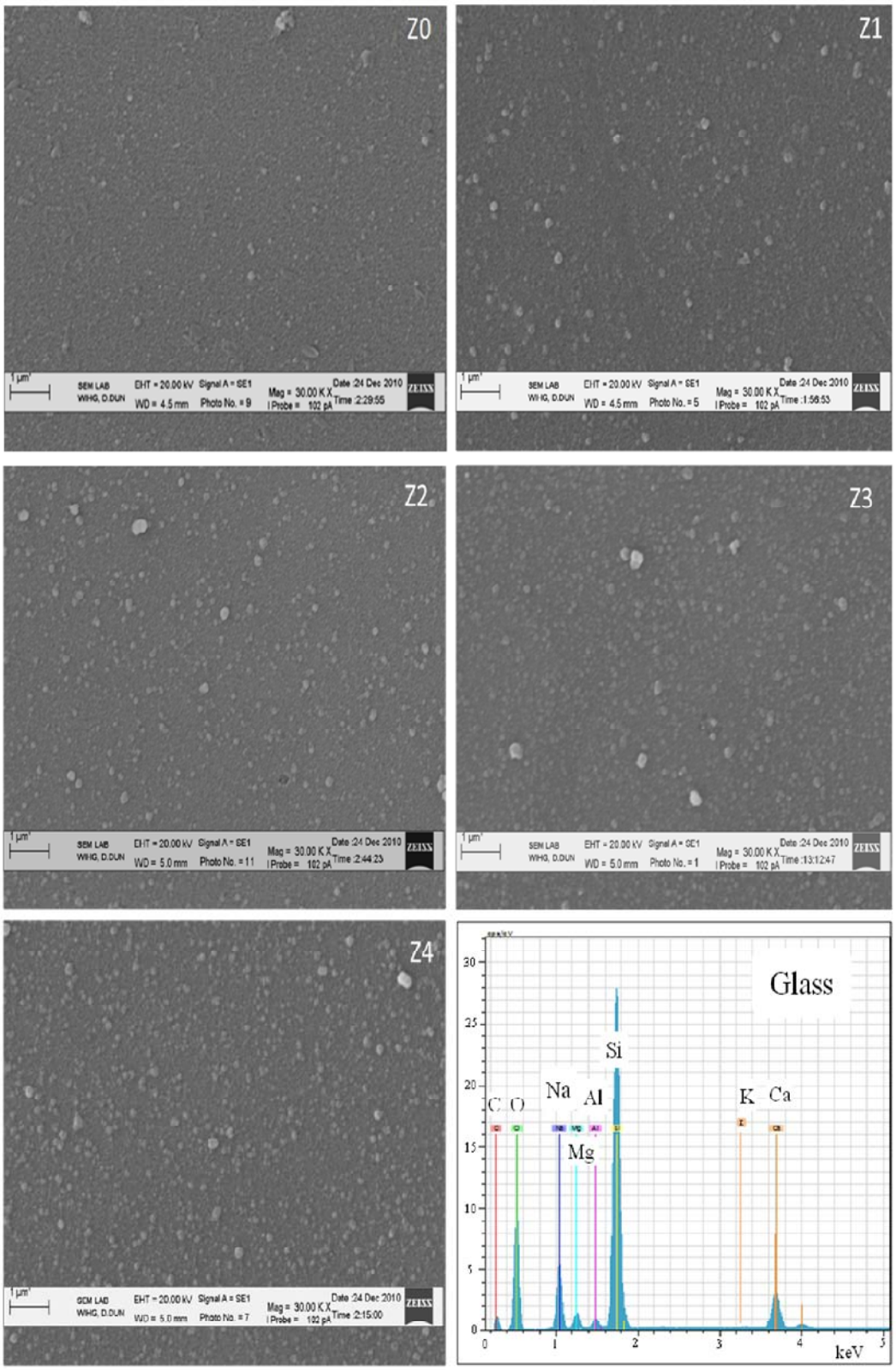

Figure 3.2.2 SEM micrographs of as–deposited film (Z0) and annealed films (Z1, Z2, Z3 and Z4) and EDAX of glass substrate (as reference)

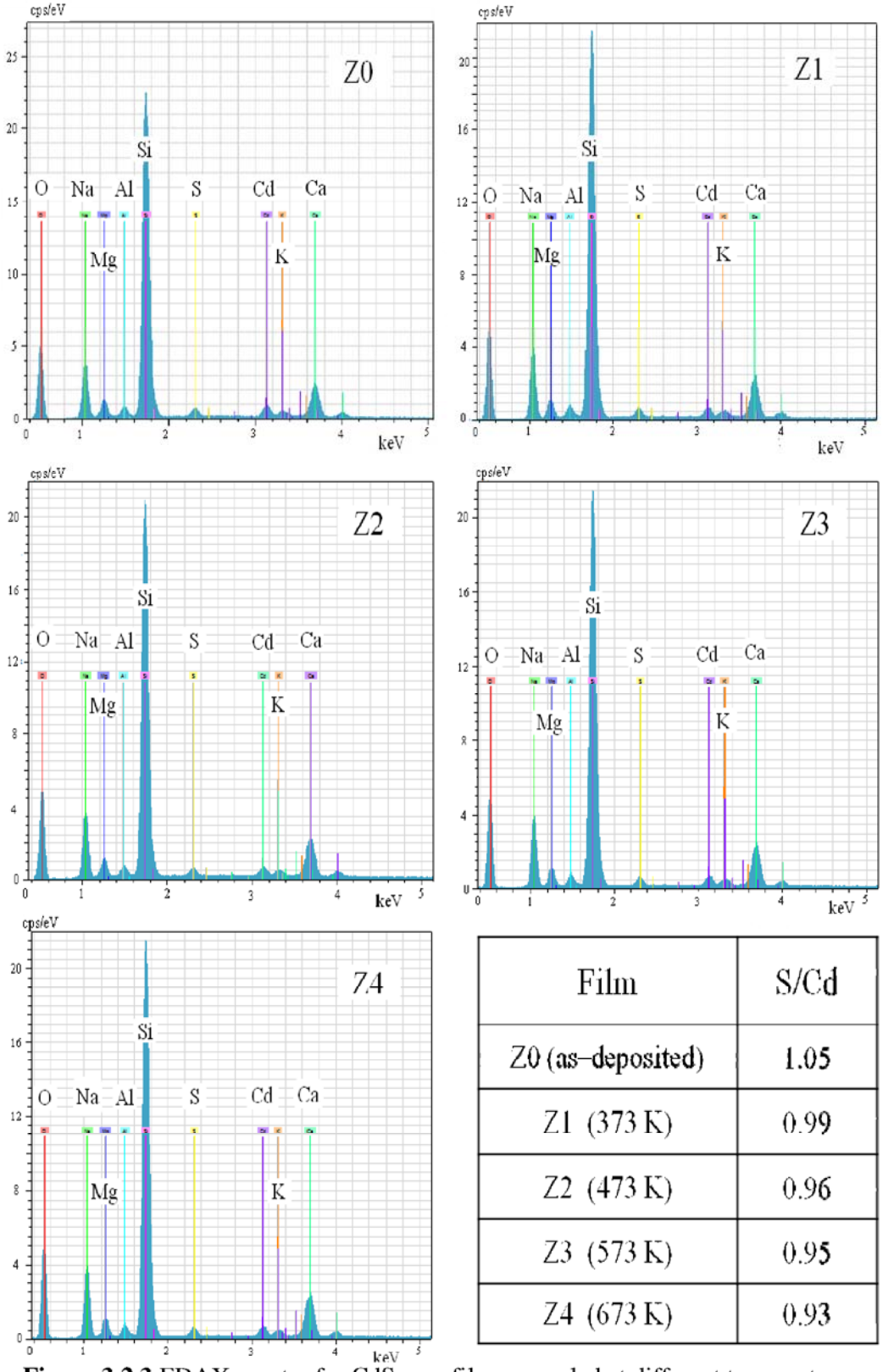

Film	S/Cd
Z0 (as–deposited)	1.05
Z1 (373 K)	0.99
Z2 (473 K)	0.96
Z3 (573 K)	0.95
Z4 (673 K)	0.93

Figure 3.2.3 EDAX spectra for CdS nanofilms annealed at different temperatures

3.2.2.3 Optical analysis

The transmittance (*%T*) of all films is high in visible and NIR region of solar spectrum (Figure 3.2.4). The relative high *%T* of the films and sharp fall in their transmission at band edge indicate low surface roughness and good homogeneity [258]. The *%T* has been observed to decrease with increase in annealing temperature. This may be due to scattering and absorption of light; since after the annealing, films become denser and for denser films scattering and absorption of light is higher [258].

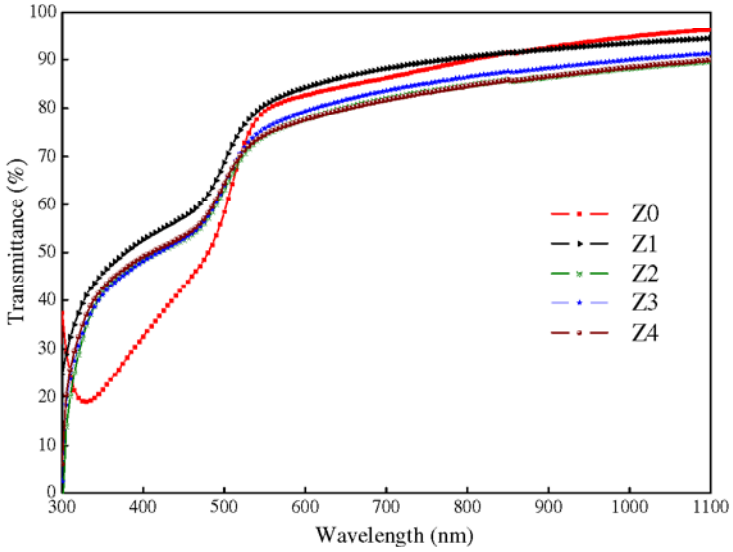

Figure 3.2.4 Transmittance (%) spectra of as–deposited film (Z0) and annealed CdS nanofilms (Z1, Z2, Z3 and Z4)

The optical absorption coefficient (α) due to inter–band transition near the band gap has been calculated using equation (2.18). The value of α is minimum for as–deposited film and increases with increase in annealing temperature (Table 3.2). This may be due to formation of larger crystallites as a result of annealing. These larger crystallites (Table 3.2) lead to an increase in absorption. Similar variation in transmittance and absorption on annealing has been reported [259,260]. The optical absorption edge shows a shift towards longer wavelengths with annealing, *i.e.*, red shift takes place *w.r.t.* as–deposited film. This red shift indicates an increase in crystallite size with increase in annealing temperature. The change in optical behavior may be due to the structural changes occurring as a result of crystallization in the films with an increase in annealing temperature.

The value of optical band gap (E_g) has been determined using equation (2.21) and listed in Table 3.2. Figure 3.2.5 clearly shows that E_g decreases with annealing

temperature. The decrease in E_g with increase in annealing temperature may be due to formation of sharp band edges because of induced recrystallization and an increase in crystallite size. The increase in annealing temperature leads to the reduction of defects and microstrain, resulting in dense homogeneous films with smaller band gap.

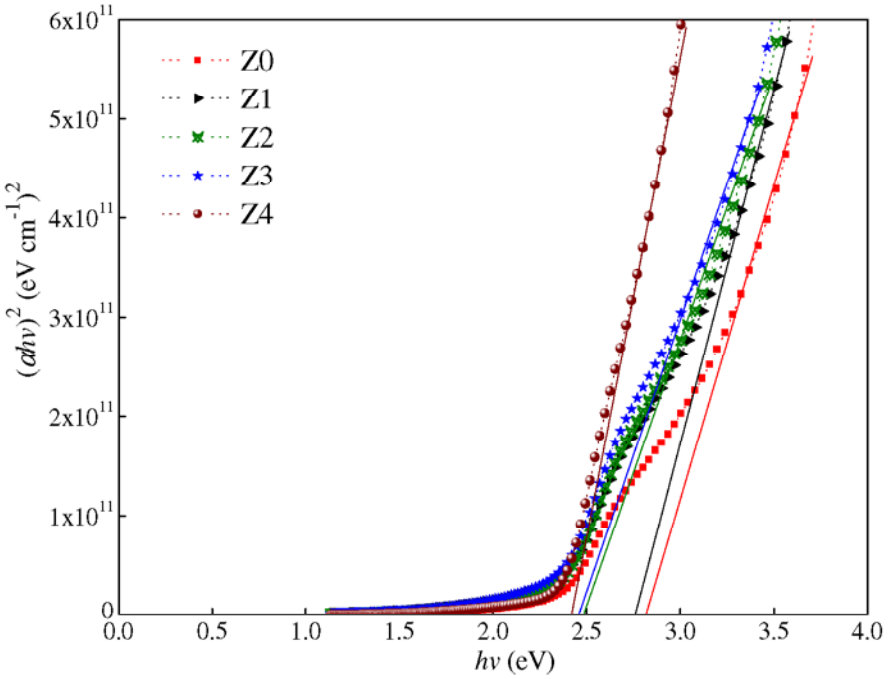

Figure 3.2.5 Plot of $(\alpha h\nu)^2$ *vs. hν* for as–deposited film (Z0) and annealed CdS nanofilms (Z1, Z2, Z3 and Z4)

3.3 Effect of molar ratio (S/Cd)

The nature of the reactants and their concentration has an influence on the rate of deposition, film thickness and stoichiometry of the films [199]. Oztas *et al.* and *Li et al.* have reported that the variation in reagent concentration (atoms/ions) leads to the formation of defects, change in crystallite quality and geometry in the deposited films [261,262]. Hodes G and Cortes *et al.* have reported that a nanocrystalline system can be deposited for a critical concentration ratio of reactants in the solution [200,263]. Marin *et al.* have studied the effect of concentration on CdS–CdTe interface in order to improve the CdS/CdTe solar cell performance [264].

This section presents the effect of S/Cd molar ratio on the structural, morphological and optical properties of CdS nanofilms. The variation in the properties with varying S/Cd ratio has been discussed in terms of quantum confinement.

3.3.1 Experimental details

The procedure for the deposition of CdS nanofilms is given in section 3.1.1. The molarities of thiourea for different S/Cd ratios {Molarity = 0.01 M (S–I), 0.02 M (S–II), 0.04 M (S–III), 0.06 M (S–IV), 0.08 M (S–V), 0.10 M (S–VI)} have been varied to deposit six nanofilms. The nanofilms have been deposited for a period of 45 min each. After deposition, films have been ultrasonically cleaned with 20% methanol solution and finally drip dried in air. The obtained films have been annealed at 573 K ± 5 K for 2 h.

Thickness, structural, morphological, compositional and optical measurements have been carried out using stylus profilometer, XRD, SEM, EDAX and UV–Vis–NIR spectrophotometer respectively.

3.3.2 Results and discussion

The thickness of the deposited nanofilms has been tabulated in Table 3.3.1. The thickness for S–III has been found to be maximum and minimum for S–V film.

3.3.2.1 Structural Analysis

XRD spectra of CdS nanofilms show broad diffraction peak profiles (Figure 3.3.1). The existence of single broad peak in all CdS films indicates nanocrystalline

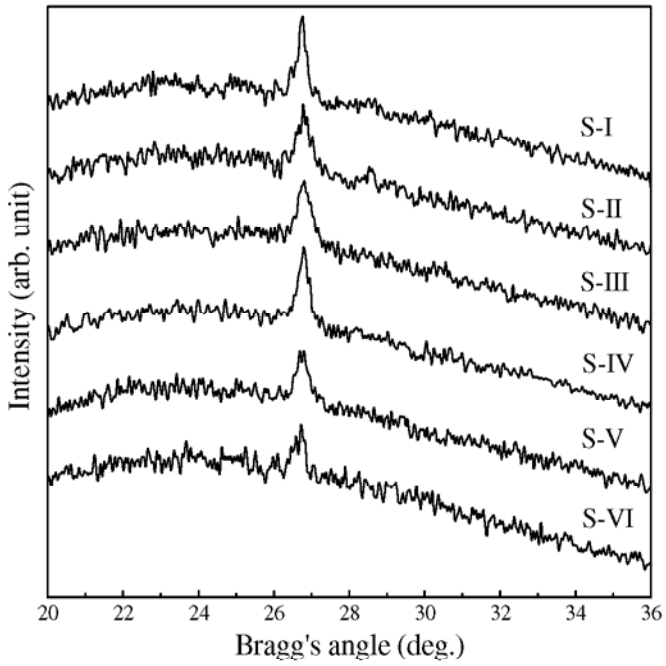

Figure 3.3.1 XRD spectra of CdS nanofilms after thermal treatment for different S/Cd molar ratios

structure. The structural analysis of films deposited for varying thiourea concentration shows a preferential orientation with a single main peak at position 2θ (Table 3.3.1). This corresponds either to hexagonal–WZ (*002*) reflection or to cubic–ZB (*111*) reflection of the CdS structure [99,242]. The more stoichiometric films (Table 3.3.2), *i.e.*, S–II & S–III show high probability for ZB (*111*) lattice reflection of the CdS structure corresponding to peak position $2\theta \approx 26.79°$, while the less stoichiometric films are aligned towards WZ (*002*) reflection corresponding to peak position $2\theta \approx 26.76°$. This behavior indicates the phase transformation, which may be due to varying S/Cd molar ratios. The smaller crystallites having large surface area in as–deposited films are more likely to undergo the phase transformation. By varying S/Cd molar ratio and on annealing their as–deposited films the crystallite size increases.

The crystallite size (D_{hkl}) in CdS thin films has been calculated using equation (2.9). It is observed that for films S–I to S–IV, reflection XRD peak intensity is high in comparison to S–V and S–VI. This indicates an enhanced nucleation and growth in the films S–I to S–IV in comparison to films S–V and S–VI. For S–I, low thiourea concentration is responsible for less release of S^{2-} ions and excess Cd^{2+} agglomerates in the solution. This causes the ionic species to get uniformly associated on the substrate surface, yielding uniform agglomeration with high crystallinity and crystallite size (SEM image, Figure 3.3.2). For film S–II, with little more thiourea decomposition, the solution is less rich in Cd^{2+} free ions. Therefore, smaller fine agglomerates of Cd^{2+} rich particles are uniformly formed with homogeneous CdS deposition. The film shows cubic–ZB (*111*) structure with an increase in crystalline order of S–II film unlike hexagonal–WZ (*002*) of S–I. The deposition conditions for films S–III and S–IV are similar on account of increasing thiourea decomposition in respective solutions indicating Cd^{2+} deficient environment. The decrease of Cd^{2+} free ion concentration with an increase in thiourea decomposition slows down the rate of agglomeration from S–III to S–IV. Therefore, lesser agglomeration of particles takes place on increasing S/Cd ratio from S–III to S–IV. On increasing the S/Cd ratio from S–III, the structural changes show a phase transformation from cubic–ZB (*111*) to hexagonal–WZ (*002*).

For S–I to S–IV (*i.e.* S/Cd molar ratio ≤ 3) the predominant mode of film deposition is *via* ion by ion mechanism [38] yielding high crystallinity and large crystallite size. For S/Cd molar ratio > 3 (S–V and S–VI), cluster by cluster mechanism of film formation is more prevalent [38]. The reaction rate is fast enough

to promote a quick CdS precipitation resulting in agglomeration in the solution rather than nucleation on the substrate. This causes poor homogeneous growth of the film. Hence, films S–V and S–VI get rich in S^{2-} and deficient in Cd^{2+} (Table 3.3.2). The crystallite size decreases to minimum for S–III due to relatively lower S/Cd ratio and optimizes (Table 3.3.1). But the crystallite size increases for S–IV to S–VI on account of high S/Cd ratio in precursor solution. For S/Cd = 2 (S–III), small crystallite size and high thickness favors optimum crystallite growth (Table 3.3.1).

Table 3.3.1 Values of S/Cd molar ratio, film thickness (t), Bragg's angle (2θ), crystallite size (D_{hkl}), interplanar spacing (d_{hkl}), microstrain (ε_{hkl}), dislocation density (ρ_{hkl}) and packing factor (p)

Film	S/Cd molar ratio	t (nm)	2θ (deg.)	D_{hkl} (nm)	d_{hkl} (Å)	ε_{hkl} $\times 10^{-3}$	$\rho_{hkl} \times 10^{15}$ line/m²	P
S–I	0.5	33.7	26.76	19.70	3.329	7.52	2.58	59.17
S–II	1	32.5	26.79	15.83	3.325	9.34	3.99	47.62
S–III	2	35.3	26.79	14.68	3.325	10.08	4.64	44.16
S–IV	3	32.2	26.76	15.53	3.325	9.54	4.15	46.70
S–V	4	31.2	26.76	16.82	3.329	8.81	3.53	50.54
S–VI	5	32.6	26.76	18.35	3.329	8.07	2.97	55.13

The interplanar spacing (d_{hkl}), microstrain (ε_{hkl}), dislocation density (ρ_{hkl}) and packing factor (p) have been determined using equations (2.1), (2.5), (2.6) and (2.7) respectively and are listed in Table 3.3.1. The calculated d_{hkl} values for all films are close to standard cubic and hexagonal values of CdS [242,265]. S–I has maximum number of atomic layers (p = 59.17) in the crystalline domain because of larger crystallites with least microstrain 7.52×10^{-3} and dislocation density of 2.58×10^{15} line/m^2. The reduction in the number of atomic layers for S/Cd $\leq$ 3 ratio (S–I to S–III), enhances the dislocation density and microstrain to maximum for S–III (Table 3.3.1). This may be due to small crystallite size and hence minimum atomic layers in S–III. On increasing the S/Cd > 3 ratio, (S–IV to S–VI), the atomic layers begin to pile up, due to increase in crystallite size, reducing the dislocation density and microstrain to minimum for S–VI. Hence, S–VI has higher number of atomic layers.

3.3.2.2 Morphological Analysis

SEM micrographs show that deposited films are homogeneous, continuous and uniform on the substrate without pinholes and cracks (Figure 3.3.2).

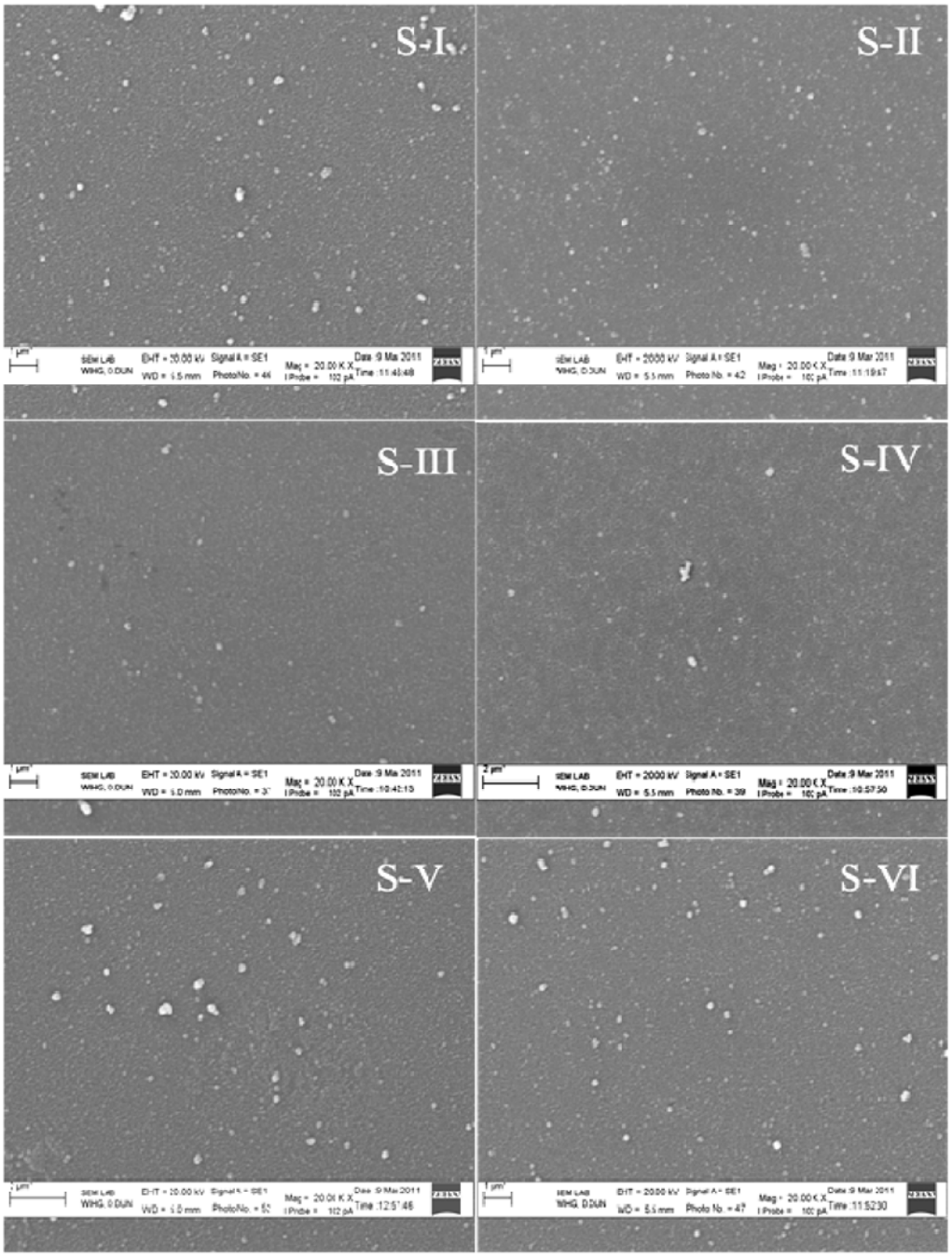

Figure 3.3.2 SEM micrographs of CdS nanofilms for varying S/Cd molar ratios

Nanocrystallites having spherical symmetry are distributed uniformly in the background throughout the surface and are closely packed to each other indicating

good adhesion with the substrate. This spherical symmetry may be due to immense surface energy of nanocrystallites. These spherical nanocrystallites may have both hexagonal and cubic structure. These films are also accompanied by small number of large clusters on the surface. These clusters may be the agglomerated atoms attached to the surface even after post deposition cleaning. The influence of S/Cd molar ratio is noticeable on S–I, S–V and S–VI, which shows large crystallite size (Table 3.3.1) and abundance of big clusters. Films S–I, S–II, S–V and S–VI show similar surface morphology having large number of nano clusters of different sizes. This may be due to the reaction between ionic species in the abundant environment of free Cd^{2+} ions for S–I and S–II and free S^{2-} ion for S–V and S–VI (Table 3.3.2). The S–III and S–IV films have identical morphology having uniform distribution of nanocrystallites with few large clusters. This type of morphological behavior of films may be due to the effect of S/Cd concentration on the nucleation and growth mechanism.

Table 3.3.2 EDAX analysis, values of absorption coefficient (α), optical band gap (E_g) and blue shift (ΔE_g) for all nanofilms

Film	EDAX analysis (at.%)			$\alpha \times 10^5$ (cm^{-1})	E_g ±0.01 (eV)	ΔE_g (eV)
	Cd	S	S/Cd			
S–I	51.14	48.86	0.96	1.12	2.58	0.16
S–II	50.60	49.40	0.98	1.43	2.67	0.25
S–III	49.60	50.40	1.02	1.59	2.88	0.46
S–IV	48.90	51.10	1.04	1.52	2.76	0.34
S–V	48.35	51.65	1.07	1.44	2.64	0.22
S–VI	47.07	52.93	1.12	1.11	2.60	0.18

EDAX spectra (Figure 3.3.3) confirm the presence of Cd and S elements in the films. It also shows small peaks of other elements as Si, Na, Ca, Mg, Al, K and O on account their presence in glass substrate. On comparing the EDAX of glass substrate with that of coated film, the actual elemental composition of the CdS thin film has been calculated (Table 3.3.2). EDAX analysis shows nearly stoichiometric S–II and S–III films in at.%. S–I is found to be sulfur deficient and S–IV to S–VI are sulfur rich. Homogeneous film formation is more probable in CBD since both Cd^{2+} and S^{2-} ion are obtained from same solution. The overall film formation shows S^{2-} deficient behavior *w.r.t.* thiourea concentration in the solution.

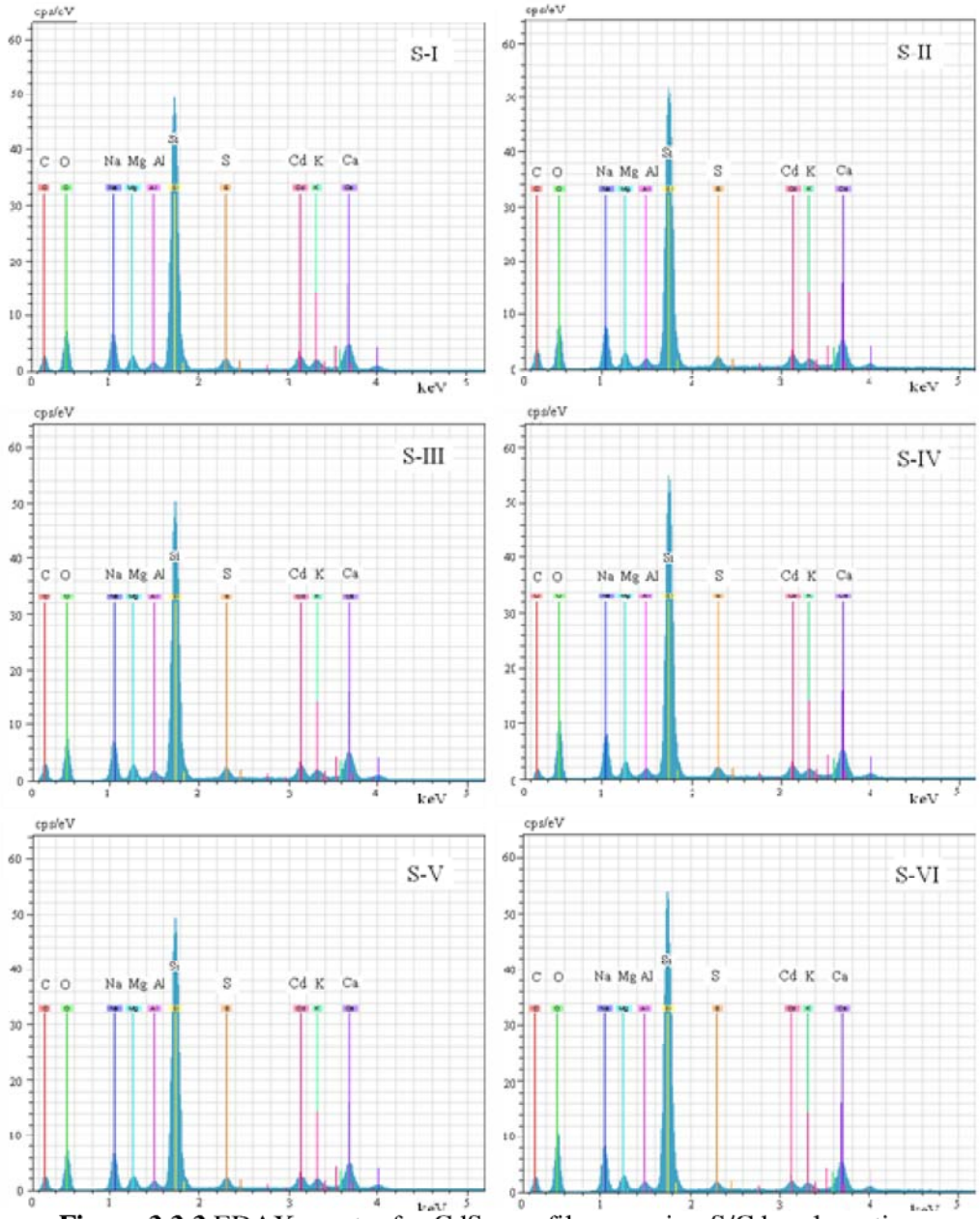

Figure 3.3.3 EDAX spectra for CdS nanofilms varying S/Cd molar ratios

3.3.2.3 Optical analysis

All films have high *%T* in visible and NIR region of spectrum (Figure 3.3.4). These have 80% average transmission for visible spectrum with highest *%T* for S–VI. There is high *%T* for S–I, S–II, S–V and S–VI in comparison to S–III & S–IV. This may be due to excess of constituent ions in the films. Moreover, increase in *%T* may also be due to an increase in the crystallite size (Table 3.3.2). The extension of *%T*

observed in high energy region up to 300 nm is an evidence of disorder or presence of amorphous component in films [208].

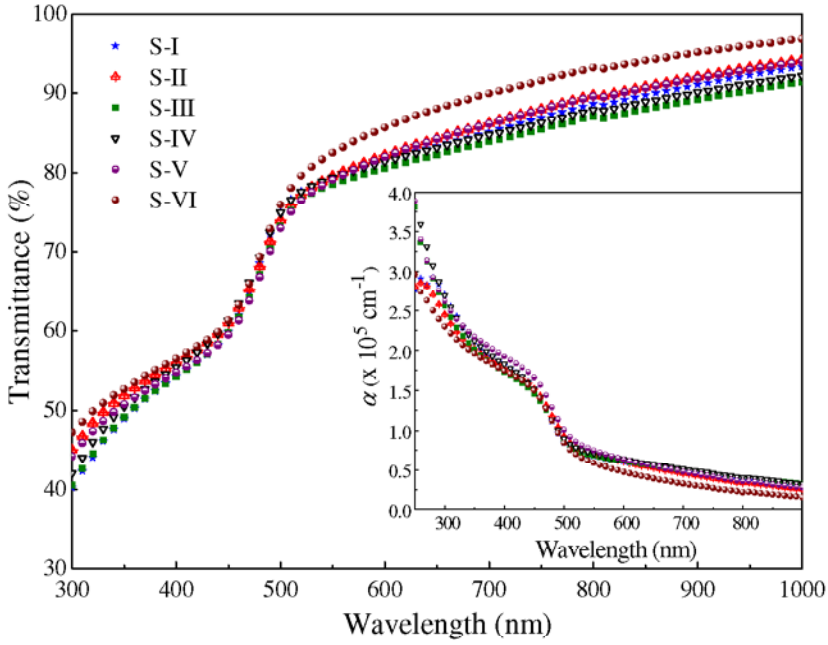

Figure 3.3.4 Transmittance (%) spectra of CdS nanofilms for varying S/Cd molar ratios and inset show plot of α *vs.* wavelength

In semiconductor nanocrystallites, a shift in absorption edge *w.r.t.* the bulk material towards shorter wavelength, *i.e.* blue shift has been reported [266]. Bulk CdS has a band gap of 2.42 eV ± 0.01 eV, corresponding to an absorption cut–off wavelength of 512 nm [116]. A blue shift (Figure 3.3.4) has been observed in all nanofilms *w.r.t.* bulk and is used to evaluate the crystallite size. The cut off wavelengths at absorption edge have been found to be 480 nm (S–I), 460 nm (S–II), 430 nm (S–III), 450 nm (S–IV), 470 nm (S–V) and 475 nm (S–VI) respectively. The absorption edge shifts toward shorter wavelength from S–I to S–III with respective increase in S/Cd molar concentration from 0.5 to 2. As a result, the crystallite size decreases, which is in agreement with XRD results (Table 3.3.1). The absorption edge shows a change in its behavior after S–III with a shift towards longer wavelength on increasing S/Cd ratio from 3 to 5 (S–IV to S–VI). This may be due to higher crystallite growth (Table 3.3.1).

The absorption coefficient (α) is influenced by scattering losses and fundamental absorption. The absorption coefficient in the strong absorption region has been calculated using equation (2.18). The type of electron transition indicating

the nature of band gap has been estimated from the value of α. Absorption coefficient has been found to be of the order of ~ 10^5 cm^{-1} for all films (Table 3.3.2) indicating direct transition. It has been observed that α increases to maximum for S–III followed by a decrease. This may be due to small nanocrystallites (Table 3.3.1) in S–III, which provide large collective surface area leading to an increase in surface to volume ratio and hence, results in a large number of absorption centers. While for other films with large crystallite size and agglomerated nano clusters, surface energy is reduced resulting in low α values.

The direct energy gap exhibits two linear region (Figure 3.3.5) one lying in the low energy range and other in high energy. This may be due to the existence of amorphous character leading to the degradation of structure and crystallites size in the

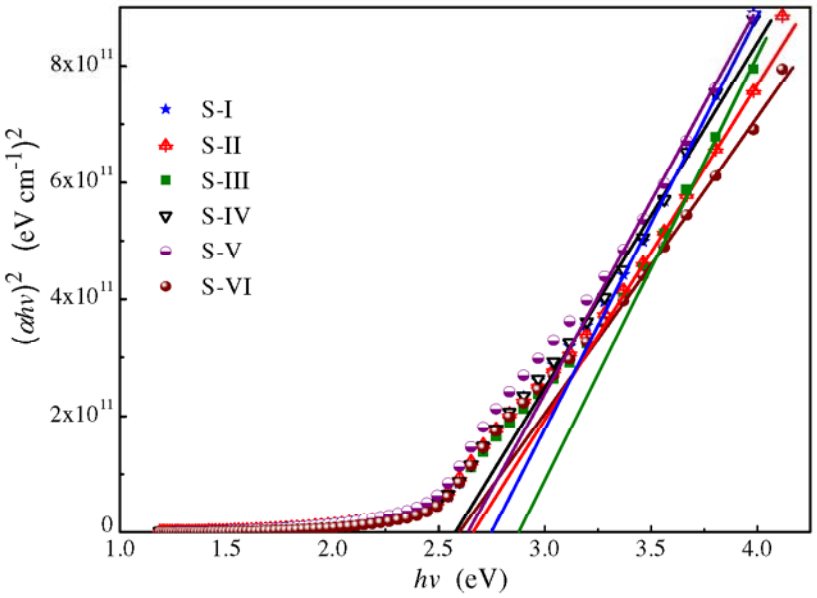

Figure 3.3.5 Plot of $(\alpha h\nu)^2$ *vs.* $h\nu$ for varying S/Cd molar ratios

films with varying S/Cd concentration. The E_g values have been estimated using equation (2.21) and are listed in Table 3.3.2. There is a shift in band gap (ΔE_g) of all films *w.r.t.* bulk CdS. The maximum blue shift has been observed for S–III and may be attributed to band gap dependence on crystallite size. With decrease in particle size, the number of constituent atoms decreases. Hence, fewer energy levels may be occupied, increasing the band gap [267]. The band gap of hexagonal phase is slightly less than the cubic phase (Table 3.3.2) and similar results have been reported by Hodes *et al.*[268].

The blue shift with decrease in crystallite size may also be explained using quantum confinement. The excitonic transitions, *i.e.*, electron transition energy between quantized valence and conduction bands [269] have been used to theoretically estimate the size of nanocrystallites. The variation in electronic structure of nanocrystallites as a function of its size has been explained on the basis of theoretical approaches; effective mass approximation (EMA) [111,112] and tight binding model (TBM) [270,271].

The parabolic band model EMA is used to explain the blue shift or change in energy gap as a function of crystallite size. According to EMA, depending upon the crystallite size, there are two limiting type of confinement regimes [112]. First the '*strong confinement regime*' applicable, when the radius of crystallite $R < a_B$, the exciton Bohr radius. For bulk CdS, the value of a_B = 3 nm [28]. In this regime, electrons and holes are considered as two confined particles. The band gap energy (E_g^{nano}) in this regime is approximated using the relation [62]

$$E_g^{nano} = E_g^{bulk} + \frac{\hbar^2\pi^2}{2\mu R^2} - \frac{1.786e^2}{\varepsilon R} \tag{3.3.1}$$

where E_g^{bulk} is the bulk band gap, μ is the effective mass of the CdS system, $\mu = m_e^* m_h^* \Big/ \left(m_e^* + m_h^*\right)$, m_e^* is the effective mass of electron (0.19 m_e), m_h^* is the effective mass of hole (0.8 m_h), R is the radius of the nanocrystallites. The second and third terms in equation (3.3.1) represent kinetic energy and coulomb interaction of the electron and holes respectively. Second is '*weak confinement regime*', for $R > a_B$. This regime is characteristic of exciton existence, treated as spheres. These spheres are confined as quasi–particles with quantized motion. The band gap energy (E_g^{nano}) in this regime is approximated using the relation [62]

$$E_g^{nano} = E_g^{bulk} + \frac{\hbar^2\pi^2}{2MR^2} \tag{3.3.2}$$

where M is the mass of exciton, given by $M = m_e^* + m_h^*$.The latter regime of EMA has been used for size calculation since the observed radius of nano crystallites $R > a_B$.
TBM is based on the atomic orbital and hopping interactions defined over a predetermined range.

According to TBM approach, the variation in blue shift (ΔE_g) with diameter of nanocrystallites (d) is estimated using relation [270]

$$\Delta E_g = a_1 e^{-d/b_1} + a_2 e^{-d/b_2} \quad (3.3.3)$$

where a_1, a_2, b_1 and b_2 are constants having values 2.83, 1.96, 8.22 and 18.07 for CdS respectively [270].

The values of blue shift as a function of crystallite size calculated from EMA and TBM have been plotted in the Figure 3.3.6. EMA underestimates the blue shift for much smaller crystallite size in comparison to experimentally obtained results from XRD [272]. In contrast, TBM results are in good agreement with experimental results. The quantum confinement in deposited films confirms low dimension structure and nanocrystallites of small volume.

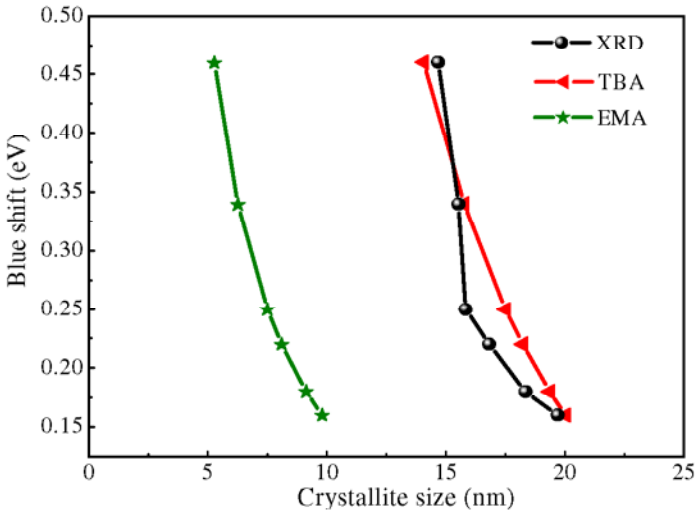

Figure 3.3.6 Plot of blue shift *vs.* crystallite size obtained by XRD, EMA and TBM

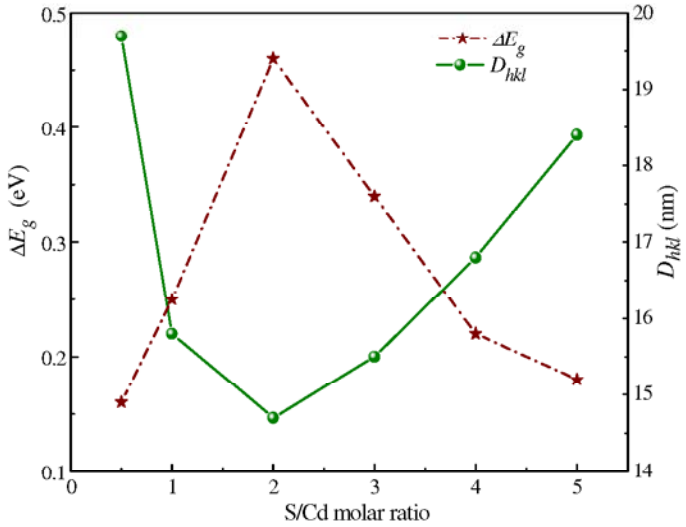

Figure 3.3.7 Dependence of ΔE_g and D_{hkl} of CdS nanofilms on S/Cd molar ratios

There is systematic change in blue shift for all films with varying S/Cd concentration in the solution (Figure 3.3.7). ΔE_g increases to maximum for S–III and the crystallite size decreases to minimum for S–III with the S/Cd molar ratio (0.5 to 2). For S/Cd molar ratio 3 to 5, there is an increase in crystallite size.

3.4 Effect of deposition temperature

Deposition temperature significantly influence the structural growth, deposition rate and reaction kinetics. The role of deposition temperature (T_d) is extremely critical in CBD for the film growth and controlling different properties of the films [208,273–275]. In this section, CdS nanofilms have been deposited at different deposition temperatures *i.e.*, T_d = 323 K, 333 K, 343 K, 353 K and 363 K. The deposited nanofilms have been studied for their structural, morphological and optical properties.

3.4.1 Experimental details

The CdS nanofilms have been deposited using experimental detail given in section 3.1.1. The solution is heated up to the deposition temperature *i.e.*, T_d = 323 K, 333 K, 343 K, 353 K and 363 K. Aqueous solution of $SC(NH_2)_2$: 0.04 M has been added and depositions have been carried out for a period of 40 min. The post deposition thermal treatment has been performed on the as–deposited films at 573 K ± 5 K for 2 h. The structural, morphological, compositional and optical measurements have been carried out using XRD, SEM & AFM, EDAX and UV–Vis–NIR spectrophotometer respectively.

3.4.2 Results and discussion

The film thickness (t) has been measured using stylus profilometer and listed in Table 3.4.1. The film thickness increases to saturation with increasing T_d from 323 K to 343 K, followed by a decrease (Figure 3.4.2).

3.4.2.1 Structural analysis

XRD spectra (Figure 3.4.1) shows that film deposited at 323 K corresponds to cubic–ZB (β–CdS) or hexagonal–WZ (α–CdS) structure [242]. With an increase in deposition temperature, *i.e.*, $T_d \leq$ 343 K, there is appearance of β/α–CdS and β–CdS phases. Films deposited for $T_d >$ 343 K have prominent α–CdS phase. The films deposited at $T_d <$ 343 K have cubic structure predominantly whereas polymorph

(cubic/hexagonal) CdS structure for T_d = 343 K. For T_d > 343 K, hexagonal phase dominance is evident from the appearance of other reflections peaks associated with α–CdS phase in the polymorph. The d_{hkl} values (Table 3.4.1) calculated using equation (2.1) are within 1% error *w.r.t.* standard d_{hkl} values of CdS [242]. The d_{hkl} values increase with rise of T_d, which may be attributed to phase alteration from cubic to polymorph.

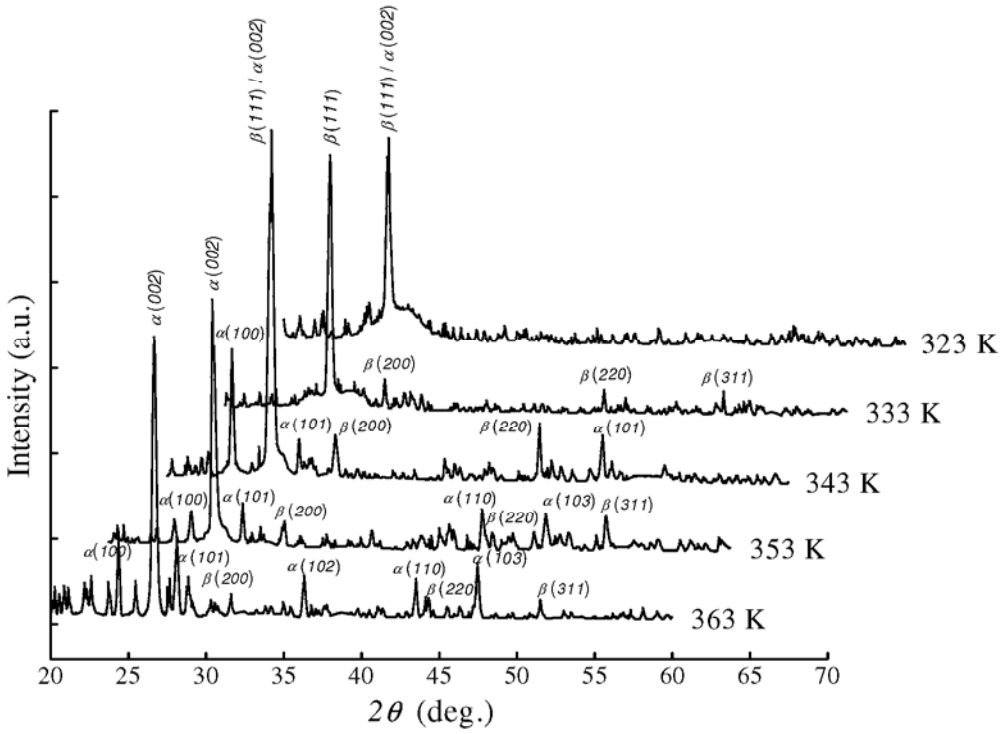

Figure 3.4.1 XRD spectra for CdS nanofilms at different T_d = 323 K, 333 K, 343 K, 353 K and 363 K

The D_{hkl} for different T_d has been determined (Table 3.4.1) using equation (2.9). The significant broad profile of XRD peaks (Figure 3.4.1) may be due to the presence of nanocrystallites, lattice defects and strain in the films. The crystallite size (D_v) and microstrain (ε_{hkl}) have been calculated (Table 3.4.1) using *WH* method (equation (2.11)). The value of the dislocation density ($\rho_{hkl} = 1/D^2_v$) has been calculated for all the films. As T_d increases from 323 K to 343 K, D_v decreases to minimum while ε_{hkl} and ρ_{hkl} increase to maximum (Table 3.4.1). For T_d > 343 K, D_v increases while ε_{hkl} and ρ_{hkl} decrease. The high dislocation density and microstrain at T_d = 343 K may be attributed to strain hardening and strengthening of the film

structure due to restriction in dislocation and its movement within grain dimensions [277].

Table 3.4.1 Values of the CdS nanofilms parameters: film thickness (t), interplanar spacing (d_{hkl}), crystallite size (D_{hkl}) by DS method, crystallite size (D_v) and microstrain (ε_{hkl}) by WH method, dislocation density (ρ_{hkl}) and AFM analysis with deposition temperature (T_d).

T_d (K)	t (nm)	d_{hkl} (Å)	D_{hkl} (nm)	D_v (nm)	ε_{hkl} $\times 10^{-3}$	$\rho_{hkl} \times 10^{15}$ (line/m^2)	AFM	
							D_{AFM} (nm)	R_{rms} (nm)
323	46.20	3.326	34.51	25.40	0.67	1.55	39	15.56
333	54.80	3.326	30.04	22.81	1.78	1.92	32	6.87
343	63.60	3.334	21.93	20.63	1.89	2.35	21	5.65
353	61.10	3.339	26.93	28.90	0.85	1.20	33	11.73
363	55.30	3.339	37.64	35.61	0.48	0.78	38	16.84

The structure formation under the influence of T_d has been discussed in terms of deposition activation energy (E_a) using Arrhenius equation [273]

$$\ell n(dr) = -\frac{E_a}{RT_d} + \ell n(A) \tag{3.3.3}$$

where dr, R, T_d and A are deposition rate, gas constant (= 8.31 Jmol^{-1}K^{-1}), deposition temperature and pre–exponential factor respectively.

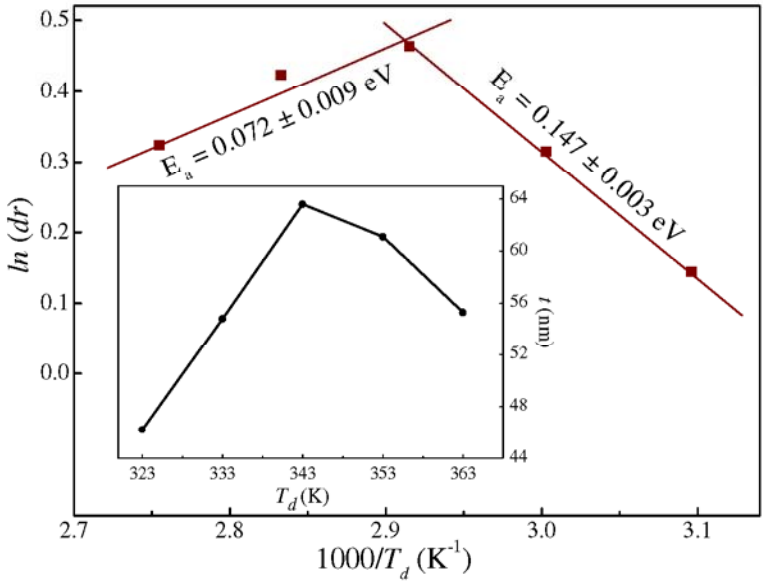

Figure 3.4.2 $ln(dr)$ *vs.* inverse of T_d. Inset shows the variation of t with T_d

The values of E_a have been observed to be 0.147 eV for deposition temperatures ranging from 323 K – 343 K and 0.072 eV for T_d = 343 K – 363 K respectively (Figure 3.4.2). The high value of E_a promotes cluster by cluster growth leading to cubic structure, whereas low E_a value corresponds to ion by ion growth favoring hexagonal structure [273]. The chemical reactions are temperature dependent. For T_d (= 323 K – 343 K), E_a has positive value and this deposition temperature range accelerates the chemical reaction. Further increase in T_d (343 K – 363 K) leads to the negative E_a values suggesting that the reaction process may be slowing down. This negative E_a value for CdS growth for temperature 343 K to 363 K suggest that there is no energy barrier to the growth, but rather that this may be due to some other factors such as running out of reactants, steric hindrance, increased desorption etc.

EDAX analysis indicates the films deposited at T_d < 343 K are rich in sulfur content while for T_d > 343 K, films are rich in cadmium (Figure 3.4.3). The ratio Cd/S (at.%) → 1.0 as T_d → 343 K and the film becomes homogeneous in nature. The change in the composition of nanofilms may be associated with the availability of free Cd^{2+} and S^{2-} ions in the reaction solution at different T_d.

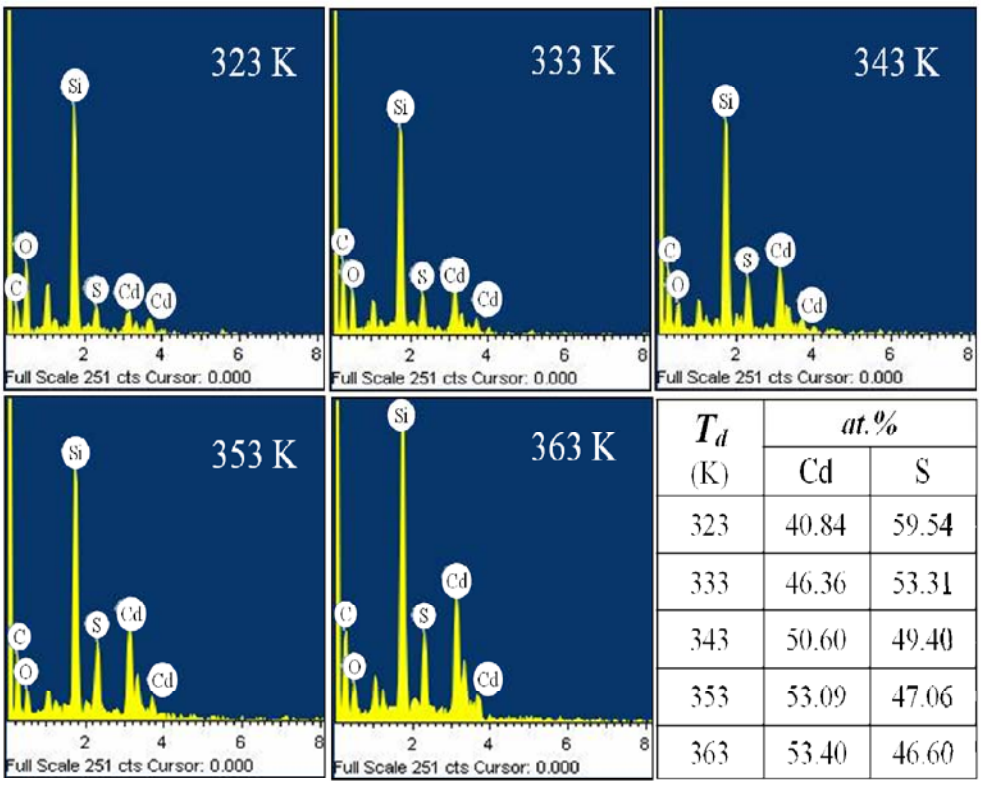

T_d (K)	at.%	
	Cd	S
323	40.84	59.54
333	46.36	53.31
343	50.60	49.40
353	53.09	47.06
363	53.40	46.60

Figure 3.4.3 EDAX spectrum of CdS nanofilms deposited at different deposition temperatures with quantized value in at.%

3.4.2.2 Morphological analysis

SEM micrographs of CdS nanofilms (Figure 3.4.4) show smooth and homogeneous surface free of pores and cracks. The spherically symmetric nanocrystallites are uniformly distributed in the background throughout the surface which produces densely packed film structure. There is presence of few clusters due to agglomeration of crystallites. The average crystallite size estimated from SEM images for films deposited at $T_d \neq 343$ has been found to be large in comparison to film deposited at $T_d = 343$ K (Figure 3.4.4).

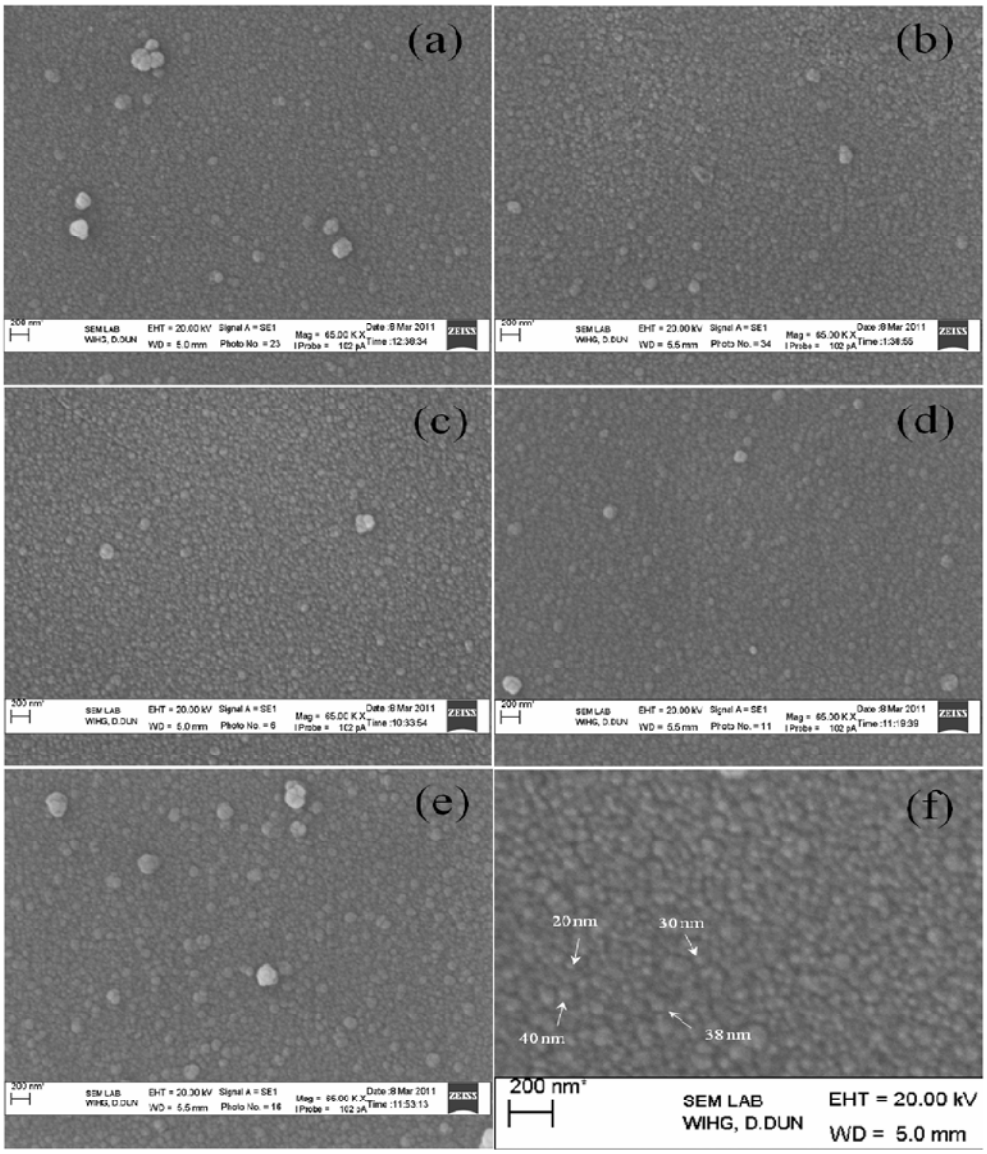

Figure 3.4.4 SEM images of CdS nanofilms deposited at different T_d: (a) 323 K, (b) 333 K, (c) 343 K, (d) 353 K, (e) 363 K and (f) zoomed image (343 K) with estimated crystallite size

Topographic images (Figure 3.4.5) for films deposited at $T_d \neq 343$ K show compact and rough surfaces with large crystallites. Nanofilm at $T_d = 343$ K show less compact but smooth surface with spherical and uniform nanocrystallites which acquire hexagonal shape for $T_d \rightarrow 363$ K (Figure 3.4.5). The size of crystallites (D_{AFM})

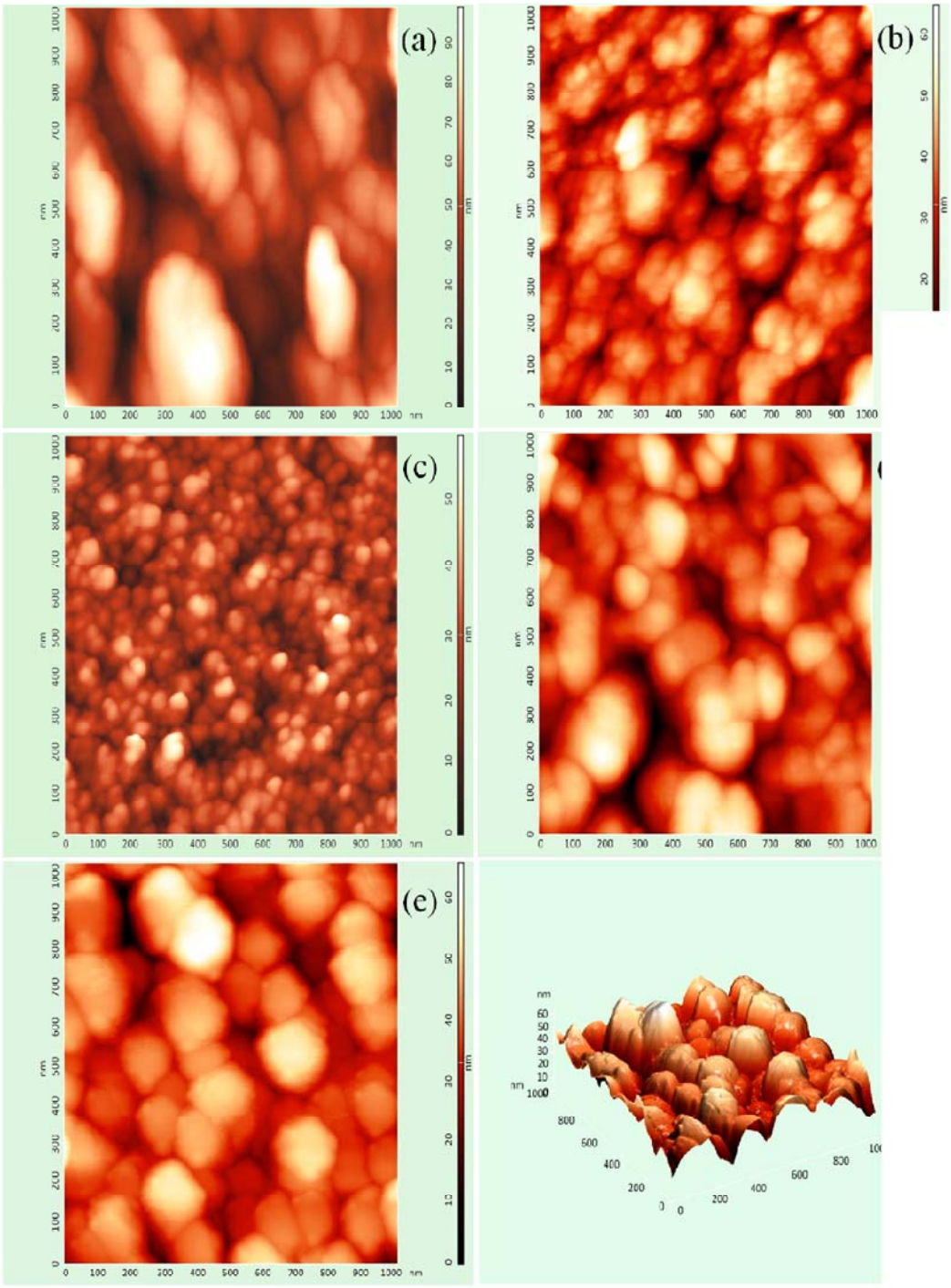

Figure 3.4.5 2D AFM images of CdS nanofilms deposited at (a) 323 K, (b) 333 K, (c) 343 K, (d) 353 K, (e) 363 K and (f) 3D AFM image of nanofilm deposited at 363 K

CHAPTER 4

Ni doped CdS nanofilms

- **Suresh Kumar**, Pankaj Sharma and Vineet Sharma, "Phase Transition in II–VI Nanofilms of Dilute Magnetic Semiconductors: $Cd_{1-x}Ni_xS$" **Science of Advanced Materials**, 5, 713 (2013).

- **Suresh Kumar**, Pankaj Sharma and Vineet Sharma, "Red shift in absorption edge of $Cd_{1-x}Ni_xS$ dilute magnetic semiconductor nanofilms" **Journal of Nanoparticle Research**, 15, 1662 (2013).

JAYPEE UNIVERSITY OF INFORMATION TECHNOLOGY
juit
विद्या तत्व ज्योतिसमः

In recent years, group II–VI semiconductors have been widely studied in various forms like quantum dots, nanorods, nanotubes, coreshells and thin films because of their applications in solar energy, optoelectronics, photochemistry, nonlinear optics, laser, etc. [7,11,71,298,299]. The optical band gap engineering in semiconductor research plays an important role towards device fabrication and their utilization. Tailoring of the band gap of semiconductor material is mainly based on the size of particles and the type of dopants [300–302]. The transition metal (TM; commonly Cr^{2+}, Mn^{2+}, Fe^{2+}, Co^{2+} and Ni^{2+}) dopants in host II–VI semiconductor introduces defects/disorders and the spin–orbit interactions may induce magnetic ordering leading to dilute magnetic semiconductors (DMS) [119,124,126,127,131,167,303–305]. Group II–VI based DMS show distinct magnetic phases like diamagnetic, paramagnetic, spin–glass like antiferromagnetic and ferromagnetic at low temperature as well as at/above room temperature [23, 124,126,127,131,159,306–308]. The spin–exchange interaction between the semiconductor charge carriers and dopant ions (*sp–d* exchange interaction) modify DMS properties making them useful for spintronics, non–volatile memories, magneto–optical devices, etc. [79,119,304–308]. The introduction of TM dopants in CdS semiconductors is an extensive route to tune them *w.r.t.* the phase, morphology and crystallite size. Therefore, it is very important to investigate how the TM dopants influence the optical and magnetic properties.

4.1 Influence of Ni^{2+} dopant on CdS nanofilms

Among the various TM ions, Ni^{2+} ions are efficient dopants for controlling the properties of various semiconductors. The presence of Ni^{2+} ions suppress the recombination of electron–hole pairs on the surface of the photocatalyst, partially increase surface area of the films and enhance the photocatalysis [85]. Ming *et al.* have observed the band gap narrowing effect in SnO_2 nanopowder with increasing nickel doping [309]. Misra *et al.* have been reported that Ni doping in CeO_2 produces weak room temperature ferromagnetism and the saturation magnetization is maximum for $Ce_{0.96}Ni_{0.04}O_2$, above which the magnetization decreased gradually [310]. Singhal *et al.* have observed paramagnetic behaviour in as–synthesized Ni doped ZnO pellets ($Zn_{0.95}Ni_{0.05}O$) however, with annealing ferromagnetic behaviour enhanced followed by a significant drop in resistance [311].

Ni^{2+} ions in CdS act as quenching centres which lead to short carrier life, thus, useful in fast optoelectronic devices. Their incorporation results in localized states in the band gap due to 3*d*–shell of Ni^{2+} ions under the action of the surrounding crystal field [312]. Ni^{2+} ions in fractional amount may able to induce magnetic character in CdS along with its semiconducting nature. This dual character may increase applicability of Ni doped CdS towards spintronics and magneto–optical applications.

In this chapter, the influence of Ni^{2+} ions in CdS nanofilms have been studied for structure, surface morphology, optical band gap and magnetic behaviour. The $Cd_{1-x}Ni_xS$ nanofilms for $0 \leq x \leq 0.09$ have been deposited by CBD technique and characterized for the above said properties.

4.1.1 Experimental details

The basic process of film deposition in CBD proceeds by the slow release of anions with a free metal cation in the presence of a complexing agent [38,200]. The chemical reactions leading to the deposition of Ni doped CdS film may be expressed as:

The cadmium/nickel tetra–amine complex ion decomposition

$$[Cd(NH_3)_4^{2+}] + [Ni(NH_3)_4^{2+}] \rightleftharpoons Cd^{2+} + Co^{2+} + 4NH_3$$

The hydrolysis of thiourea in alkaline solution with S^{2-} ions generation

$$SC(NH_2)_2 + 2OH^- \rightarrow CH_2N_2 + 2H_2O + S^{2-}$$

The overall reaction for varying molar concentration of Co^{2+} ions (x) is as follows

$$(1-x)[Cd(NH_3)_4^{2+}] + x[Ni(NH_3)_4^{2+}] + SC(NH_2)_2 + OH^- \xrightarrow[\text{TEA and TX–100}]{\text{at 343 K \& } p\text{H 11}} (Cd_{1-x}Ni_xS)_{film} + CN_2H_2 + 4NH_3\uparrow + 2H_2O$$

The experimental procedure for the deposition of undoped CdS nanofilms is given in section 3.1.1 and 3.3.1. Ni doped CdS films have been deposited by adding $NiCl_2.6H_2O$ (1 mM to 5 mM), with Ni to Cd ratio $x_m = Ni/(Cd+Ni)$ varied in the range of 0 – 0.2, into reaction bath. Few drops of triethanolamine (TEA; 4%) have been added to the final solution to control the release of metal complex during the reaction.

The films have been grown at a constant temperature (343 K ± 2 K), *p*H (= 11) and for a deposition period of 80 min under constant stirring. After deposition, the films have been ultrasonically washed with acetic acid (5%) to remove the poorly adherent particles and dried. Post deposition annealing has been performed at 573 K ± 5 K.

The deposited films have been characterized using XRD, FTIR, FE–SEM, EDAX, AFM, UV–Vis–NIR double beam spectrophotometer and VSM.

4.1.2 Results and discussion

The thickness of the deposited films has been measured by stylus profilometer (Table 4.1). The results have been verified by the tilted SEM images of the nanofilms (Figure 4.1) and found to be in agreement with profilometer measurement with accuracy of ± 2 nm.

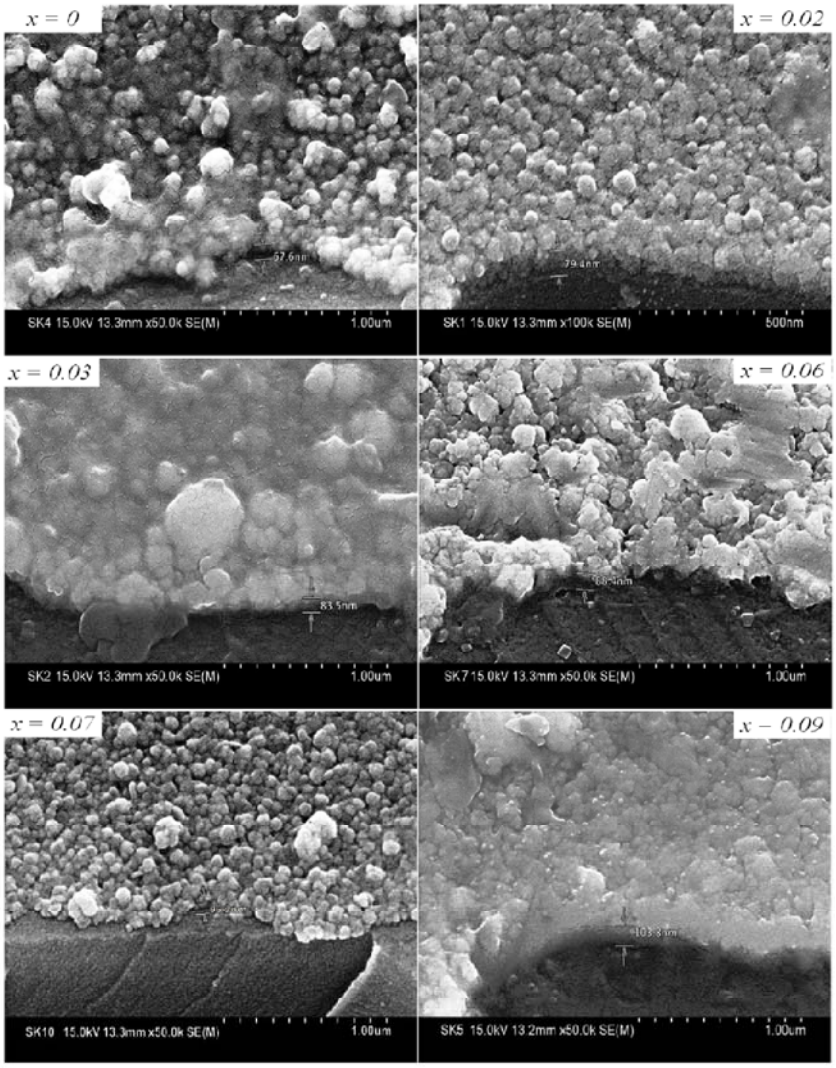

Figure 4.1 Tilted SEM images for thickness of $Cd_{1-x}Ni_xS$ ($0 \leq x \leq 0.09$) nanofilms

4.1.2.1 Structural analysis

GAXRD spectra shows that all the deposited nanofilms contain (*100*) and (*002*) reflection peaks which belong to α–CdS structure [242] in conjunction with other reflection peaks shared by either α–CdS or both α and β–CdS (Figure 4.2). The existence of multiple reflection peaks show the polycrystalline nature of the deposited nanofilms comprising of preferred orientation along (*002*) direction. The intensity of reflection peaks of $Cd_{1-x}Ni_xS$ ($0 \leq x \leq 0.09$) reduces, while the 2θ position of prominent (*002*) peak shifts to higher diffraction angle with increase in Ni content. The Ni content in CdS structure is responsible for structural disorder and hence, results in degradation of crystallinity. The shifting of diffraction peaks is attributed to the incorporation of Ni^{2+} ions into host CdS lattice. The small cation size of Ni^{2+} ($r_{Ni}^{2+} = 0.69$Å) in comparison to Cd^{2+} ($r_{Cd}^{2+} = 0.95$Å) [313] contracts the lattice (Table 4.1). No characteristic peak associated with Cd, Ni, NiS or their oxide phase has been observed in GAXRD spectra, which suggests a thorough distribution of Ni^{2+} in CdS. The α–CdS phase in nanofilms remain dominant on addition of Ni^{2+} impurities, but the reflection peaks (Figure 4.2) become broad leading to a decrease in crystallite size and abundance of lattice defects. A stable CdNiS structure may also be formed by the release of internal strain and hence, the grain size reduces with increasing Ni content.

Table 4.1 Values of film thickness (t), Bragg's angle (2θ), interplanar spacing (d_{hkl}), lattice constants (a & c), crystallite size (D_{hkl}), microstrain (ε_{hkl}) and dislocation density (ρ_{hkl}) for $Cd_{1-x}Ni_xS$ ($0 \leq x \leq 0.09$) nanofilms

Film	t (nm)	2θ (deg.)		d_{hkl} (Å)	Lattice Parameter		D_{hkl} (nm)	ε_{hkl} $\times 10^{-3}$	ρ_{hkl} $\times 10^{15}$ (line/m^2)
		(*100*)	(*002*)		a (Å)	c (Å)			
CdS	67.6	24.13	26.73	3.332	4.255	6.665	21.17	3.46	2.23
$Cd_{0.98}Ni_{0.02}S$	79.4	24.17	26.82	3.321	4.248	6.643	16.83	4.34	3.53
$Cd_{0.97}Ni_{0.03}S$	83.5	24.20	26.85	3.318	4.243	6.636	15.84	4.61	3.99
$Cd_{0.94}Ni_{0.06}S$	88.4	24.21	26.89	3.313	4.242	6.626	14.69	4.96	4.64
$Cd_{0.93}Ni_{0.07}S$	92.2	24.24	26.92	3.309	4.236	6.619	13.46	5.41	5.52
$Cd_{0.91}Ni_{0.09}S$	103.8	24.30	27.00	3.309	4.236	6.619	11.54	6.31	7.51

The crystallite size (D_{hkl}) and interplanar spacing (d_{hkl}) have been calculated using equations (2.9) and (2.1) respectively (Table 4.1). The values of D_{hkl} as well as

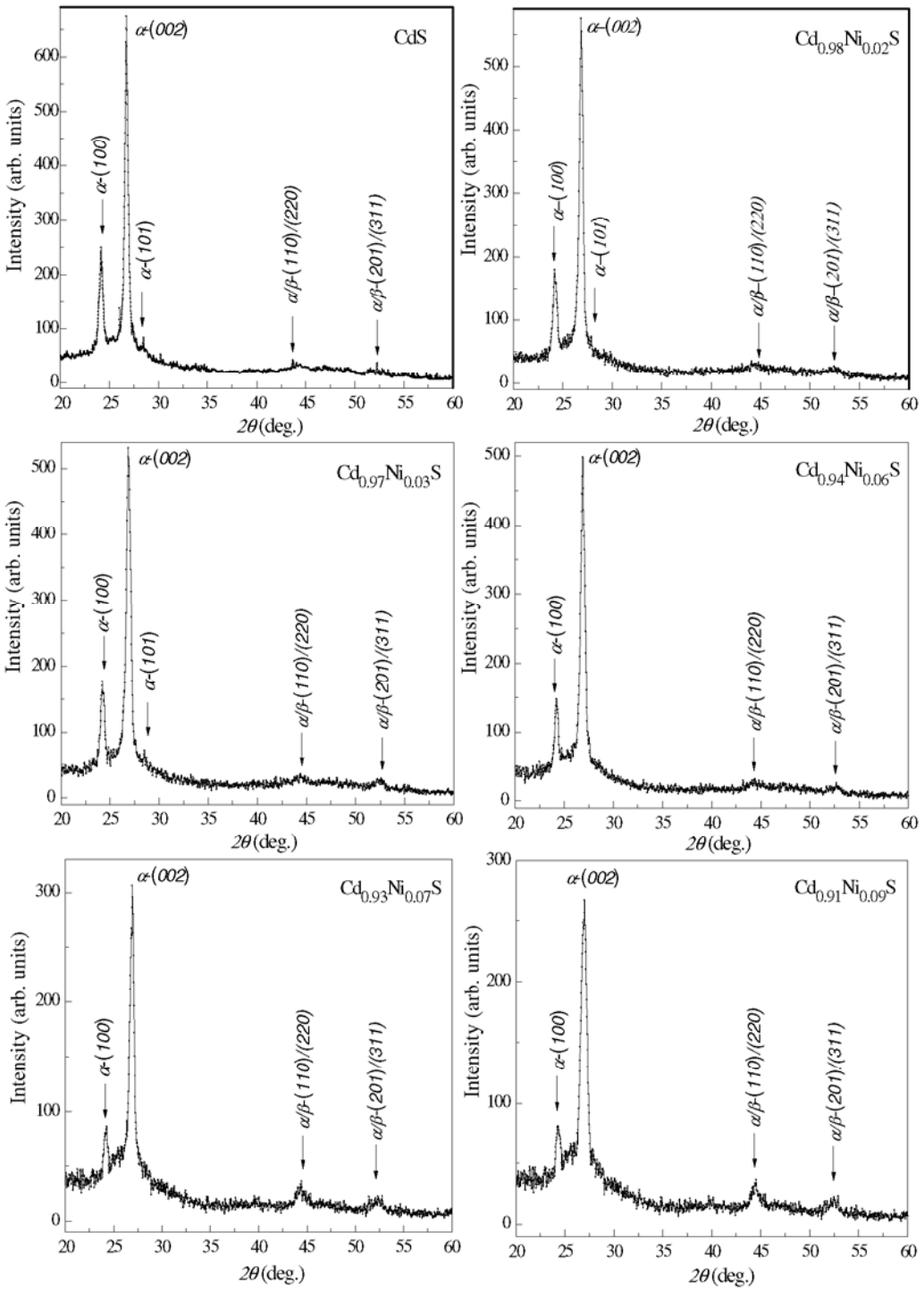

Figure 4.2 GAXRD spectra for $Cd_{1-x}Ni_xS$ ($0 \leq x \leq 0.09$) nanofilms

d_{hkl} (Table 4.1) decrease with the increase in Ni concentration and are responsible for variation in lattice parameters. The lattice parameters ($a = 2d_{100}/\sqrt{3}$ and $c = 2d_{002}$) have been calculated (Table 4.1) using the values of d_{002} and d_{100} [105]. The *c/a* ratio has been observed to be < 5% for $Cd_{1-x}Ni_xS$ nanofilms in comparison to the ideal *c/a*

value for the WZ–CdS structure [242]. The low *c/a* values and shift of 2θ to higher value indicate that the nanofilms are under tensile strain along (*002*) orientation. The decrease in *c/a* value indicates a lattice contraction due to substitution of large Cd^{2+} ions by the small Ni^{2+} ions in the α–CdS structure. This lattice contraction results in solidification of nanocrystallites.

However, the reduced crystallite size due to Ni^{2+} doping may be responsible for variation in microstrain (ε_{hkl}) and dislocation density (ρ_{hkl}) (Table 4.1) which shows an increase with Ni content. This reflects towards growing number of structural defects in CdS structure with Ni incorporation. The surface energy of the nanocrystallites decrease, which leads to size contraction and solidification by distorting their crystal lattice elastically. A correlated arrangement of nanoparticles is responsible for the random structural disorder. The defects may be formed in grain boundaries due to an increase in microstrain and dislocation density on Ni doping, play an important role.

FTIR spectra for $Cd_{1-x}Ni_xS$ nanofilms (Figure 4.3) show various absorption bands/peaks at different frequencies. The absorption bands/peaks at ~ 3400 cm^{-1} – 3430 cm^{-1}, 1438 cm^{-1} – 1450 cm^{-1}, 860 cm^{-1} – 900 cm^{-1}, 1370 cm^{-1} – 1400 cm^{-1}, 1990 cm^{-1} – 2150 cm^{-1} and weak doublet at 2920 cm^{-1} and 2851 cm^{-1} have been assigned to the O–H stretching, asymmetric scissor deformation (δ_{as}–CH_2), hydrogen bound O–H out of plane bending, primary or secondary OH in–plane bending, isothiocyanate (–NCS) formed due to the thiourea dissociation, the asymmetrical and symmetrical vibration of the CH_2 group (υ_{as}–CH_2 and υ_s–CH_2) respectively [314–316]. The peak at ~ 1011 cm^{-1} ($x = 0$) and ~ 1075 cm^{-1} ($x = 0.02 – 0.09$) belongs to primary amine C–N stretch [314] and also shared by C–O stretching [315]. However, secondary amine C–N stretch is indicated by peaks at 1399 cm^{-1} ($x = 0$) and ~ 1370 cm^{-1} ($x = 0.02$ – 0.09) [314]. These peaks of C–N stretching are evolved due to alkaline nature of solution because of the presence of TEA and NH_3. The $Cd_{1-x}Ni_xS$ ($x \geq 0.03$) nanofilms have small peaks in the region 470 cm^{-1} – 600 cm^{-1} belonging to S–S stretch [314]. All nanofilms have an absorption peak at ~ 650 cm^{-1} associated with Cd–S stretching [315]. No peak for the Ni–S stretching has been observed which may be due to the homogeneous substitution of Ni^{2+} ions in CdS structure. The shift of Cd–S stretch (~ 650 cm^{-1}) towards the lower wavenumbers with increasing x indicates the incorporation of Ni^{2+} ions in the CdS structure.

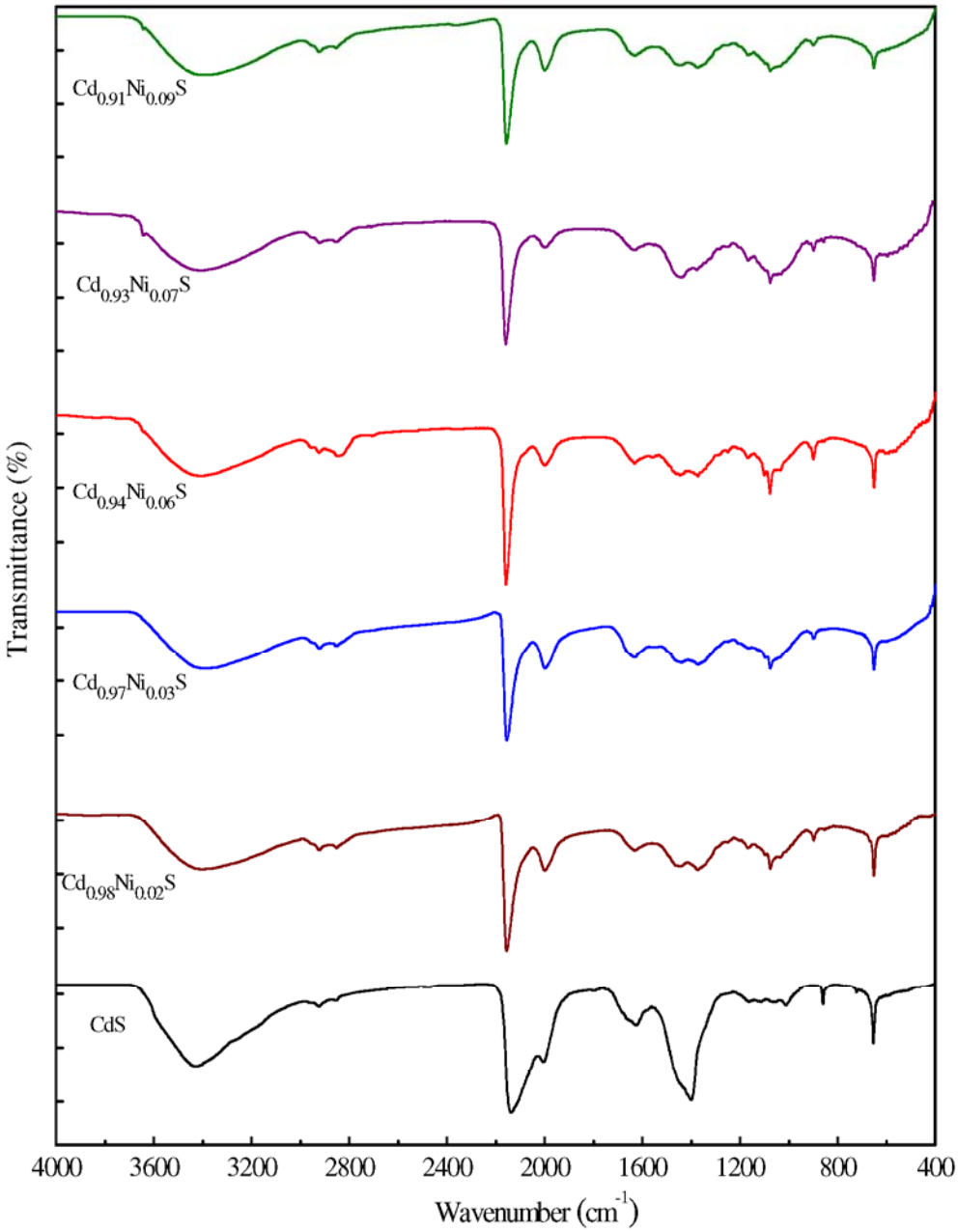

Figure 4.3 FTIR spectra for $Cd_{1-x}Ni_xS$ ($0 \leq x \leq 0.09$) nanofilms (The ordinate scale for different x vales is shifted for clarity)

4.1.2.2 Morphological analysis

Figure 4.4 shows the surface morphology for $Cd_{1-x}Ni_xS$ nanofilms at a scale of 1μm (50K×). All nanofilms show uniformly distributed spherical nanocrystallites on the surface of substrate with good adhesion. The surface of all films is compact, densely packed, continuous and barren free which may be attributed to the chemical activity of triton (TX–100) (section 3.2.2.2). The surface morphology of nanofilms is

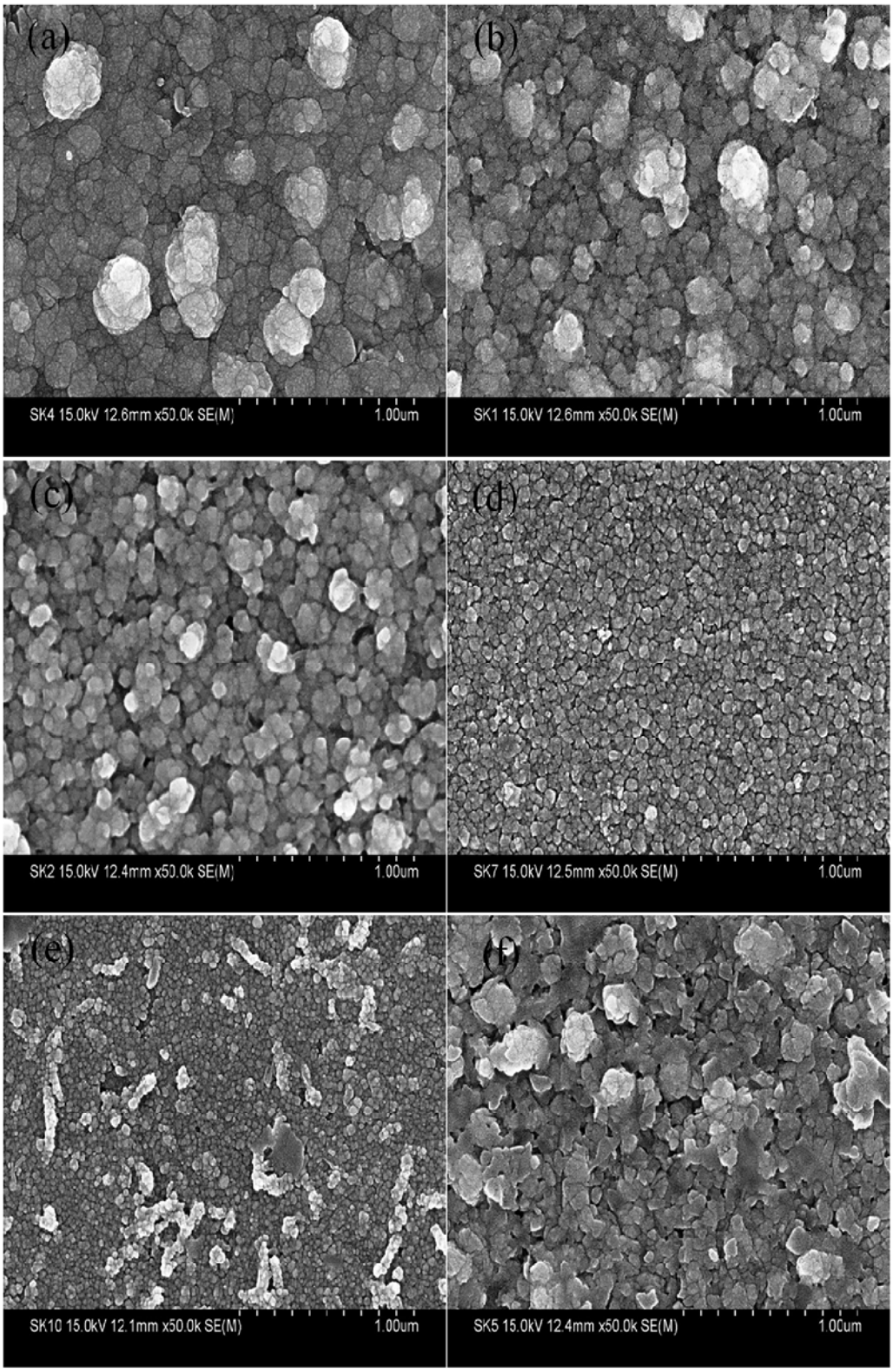

Figure 4.4 SEM micrographs for $Cd_{1-x}Ni_xS$ nanofilms ((a): $x = 0$, (b): $x = 0.02$, (c): $x = 0.03$, (d): $x = 0.06$, (e): $x = 0.07$ and (f): $x = 0.09$)

strongly dependent on Ni content. The substitution of Ni^{2+} ions in CdS structure produces substantial surface changes with less agglomeration of the crystallites *i.e.*, reduction in crystallite size and increase in grain boundaries. The nanofilm $x = 0.07$ shows sphere–like crystallite chains in an irregular spatial distribution. However, the surface morphology for $x = 0.09$ is quite different, showing sheet like structural growth.

EDAX spectra (Figure 4.5) confirm the presence of Cd, S and Ni elements in the deposited films. EDAX results for Ni doped CdS films ($x_f = Co/(Cd + Co)$) are in accordance with the molar ratio of Ni^{2+} ions in solution ($x_m = Co/(Cd + Co)$) and the constituent elements have been observed as expected (Figure 4.6). The Ni^{2+} ions get substituted in host CdS structure with decreasing Cd^{2+} leading to the variation in Cd and S content (Table 4.2).

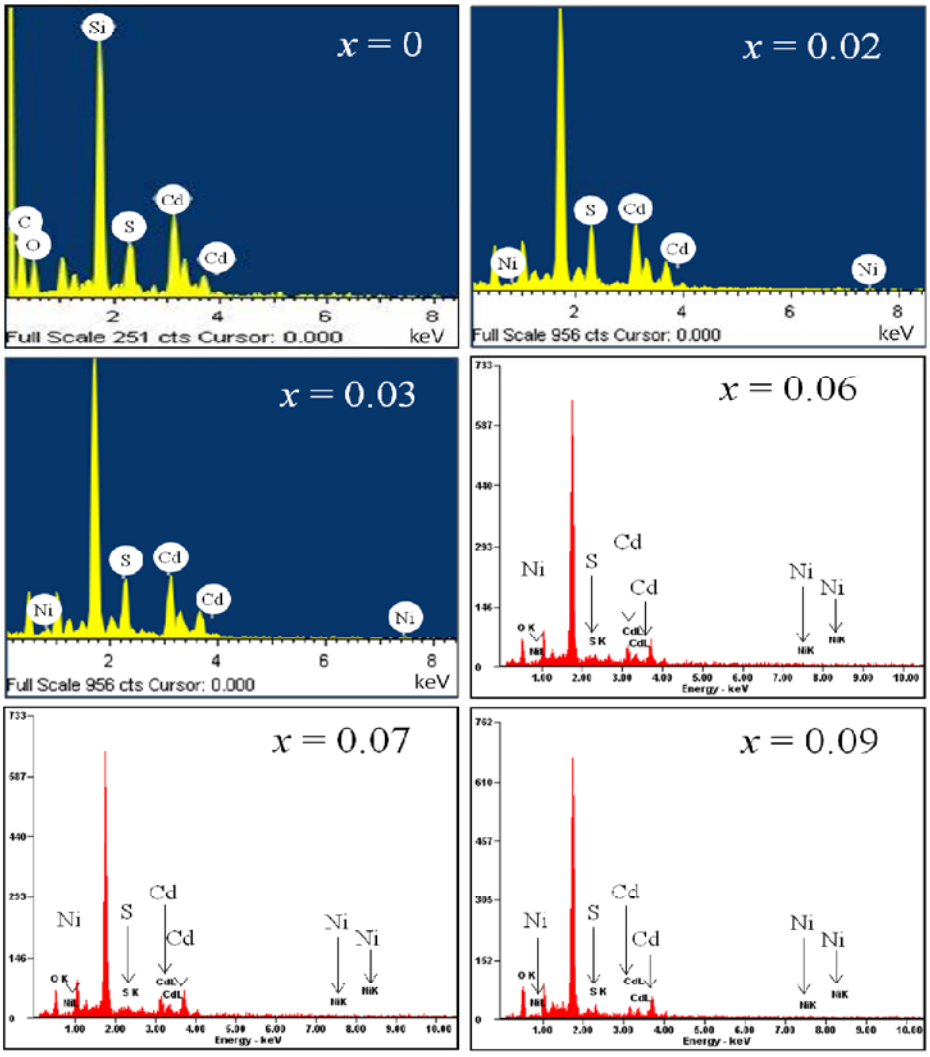

Figure 4.5 EDAX spectra for $Cd_{1-x}Ni_xS$ ($0 \leq x \leq 0.09$) nanofilms

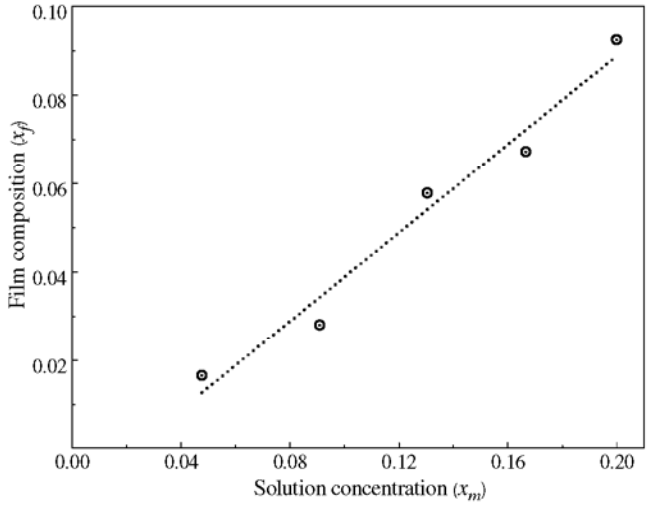

Figure 4.6 Plot of solution concentration (x_m) from molarities and film composition (x_f) from EDAX for $Cd_{1-x}Ni_xS$ nanofilms

The surface topography and structure of $Cd_{1-x}Ni_xS$ DMS nanofilms surfaces are shown in Figure 4.7 (3D AFM images) and Figure 4.8 (2D AFM images). All nanofilms grow with columnar structure along the *c*–axis perpendicular to the substrate (Figure 4.7) which confirms the prominent hexagonal–WZ structure in the deposited nanofilms [107,287]. The low values of surface skewness ($S_{sk} < 0.7$) and

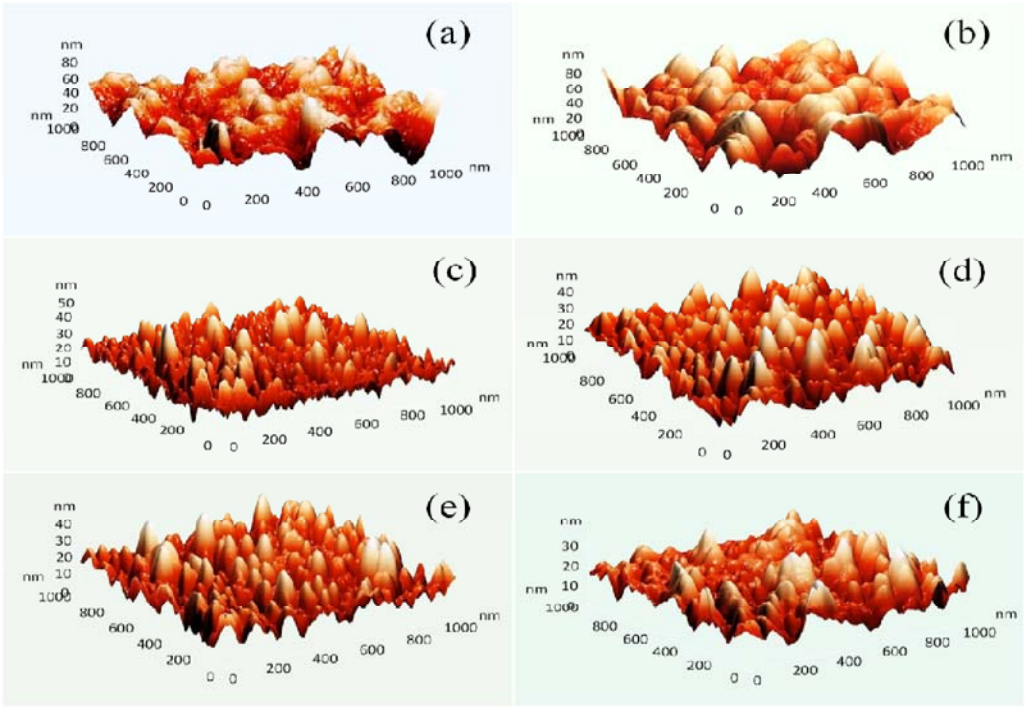

Figure 4.7 3D AFM images for $Cd_{1-x}Ni_xS$ nanofilms ((a): $x = 0$, (b): $x = 0.02$, (c): $x = 0.03$, (d): $x = 0.06$, (e): $x = 0.07$ and (f): $x = 0.09$)

kurtosis coefficient ($S_{ka} \geq 3$) for all nanofilms indicate that the height distribution is uniform, with approximately equal number of high peaks to deep valleys (Figure 4.7(a–f)) over the scanned area (1 μm × 1 μm). Nanofilm with $x = 0$ (Figure 4.8(a))

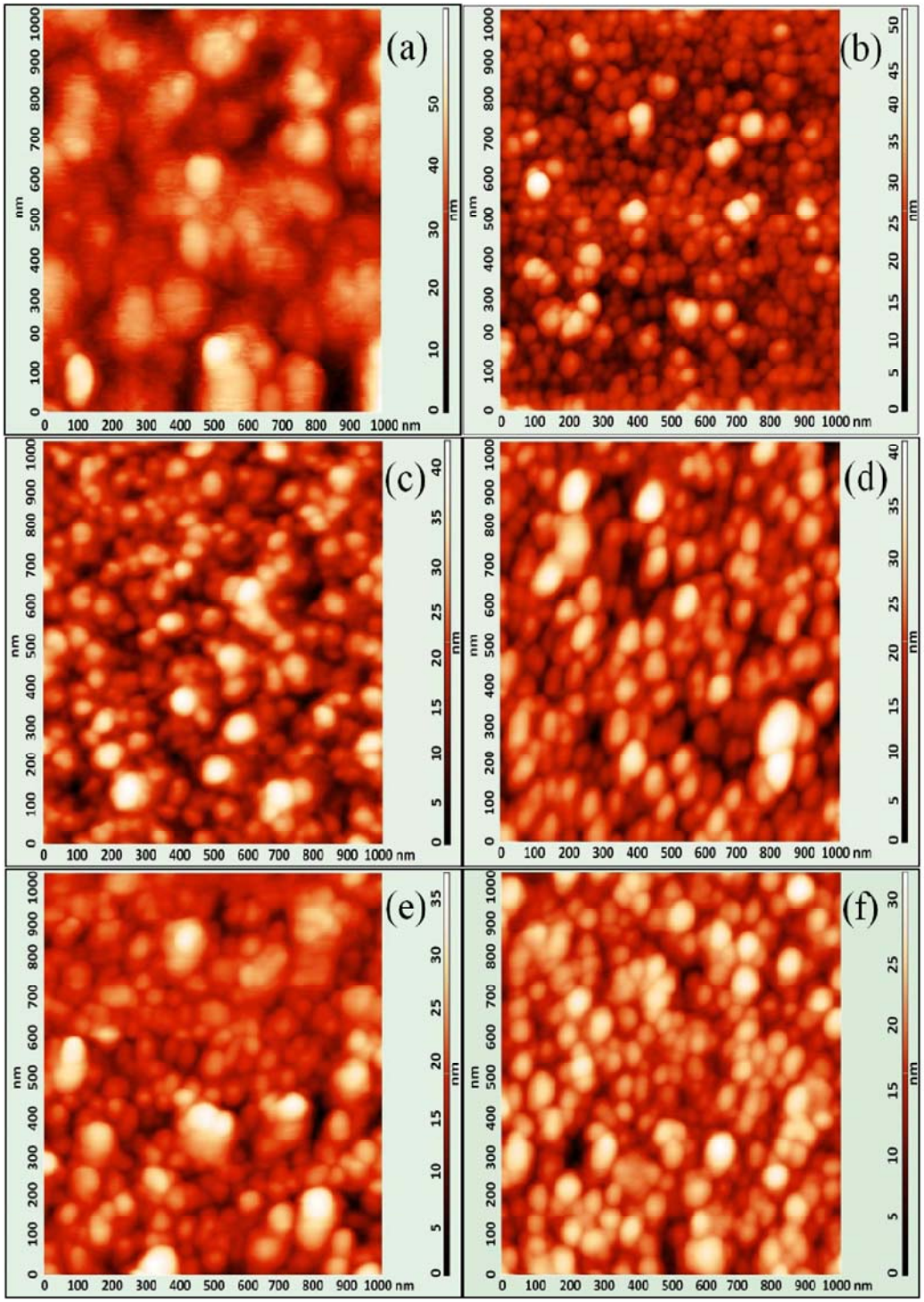

Figure 4.8 2D AFM images for $Cd_{1-x}Ni_xS$ nanofilms ((a): $x = 0$, (b): $x = 0.02$, (c): $x = 0.03$, (d): $x = 0.06$, (e): $x = 0.07$ and (f): $x = 0.09$)

possess larger crystallites (D_{AFM}) and high average surface roughness (R_f) (Table 4.2). However, with increasing Ni^{2+} concentration (Figure 4.8(b–f)) the D_{AFM} of $Cd_{1-x}Ni_xS$ nanofilms decreases. R_f also decreases up to $x = 0.07$. Initially, with increase in Ni^{2+} concentration from $x = 0$ to $x = 0.06$, the incorporation of Ni^{2+} ions in CdS structure deteriorate the larger crystallite into smaller one (Figure 4.8).

Table 4.2 The compositional, morphological and optical parameters of $Cd_{1-x}Ni_xS$ ($0 \leq x \leq 0.09$) nanofilms

Film	*at.*% from EDAX			AFM		$\alpha \times 10^4$ at absorption edge (cm^{-1})	E_g (eV)	E_u (eV)
	Cd	Ni	S	D_{AFM} (nm)	R_f (nm)			
CdS	53.40	....	46.60	26	9.6	1.01	2.80	0.282
$Cd_{0.98}Ni_{0.02}S$	52.17	0.88	46.95	21	5.2	2.65	2.65	0.291
$Cd_{0.97}Ni_{0.03}S$	51.17	1.48	47.35	17	5.1	2.73	2.53	0.332
$Cd_{0.94}Ni_{0.06}S$	46.58	2.86	50.56	15	5.0	2.77	2.49	0.372
$Cd_{0.93}Ni_{0.07}S$	45.47	3.28	51.25	15	3.1	5.32	2.40	0.490
$Cd_{0.91}Ni_{0.09}S$	47.66	4.86	47.48	10	4.5	6.80	2.33	0.509

4.1.2.3 Optical analysis

Figure 4.9 shows *%T* and *%R* spectra of DMS nanofilms grown on glass substrate. The occurrence of low *%T* interference pattern in spectra indicates that the deposited nanofilms are ultra thin, smooth and homogeneous. But, in the visible region, the relatively high *%T* (> 65%) and low *%R* (< 20%) make these films good candidate for solar energy applications.

The optical behavior of deposited DMS nanofilms have been analyzed in terms of optical absorption coefficient (α) calculated using equation (2.19). The value of α for all nanofilms (Table 4.2) has been found to be of the order of 10^4 cm^{-1} in the visible region, and at absorption edge, α increases with increasing Ni content (Figure 4.10). This may be due to decrease in crystallite size which provides large collective surface area and number of absorption/scattering centers for light.

The exponential dependence of α on photon energy ($h\nu$) near the band edge has been studied in terms of Urbach energy (E_u) by Urbach–Martienssen model (equation 2.22). A systematic increase in E_u (Table 4.2) may be attributed to the

creation of more localized states within the band tails of valence band and conduction band due to the existence of defects and disorders.

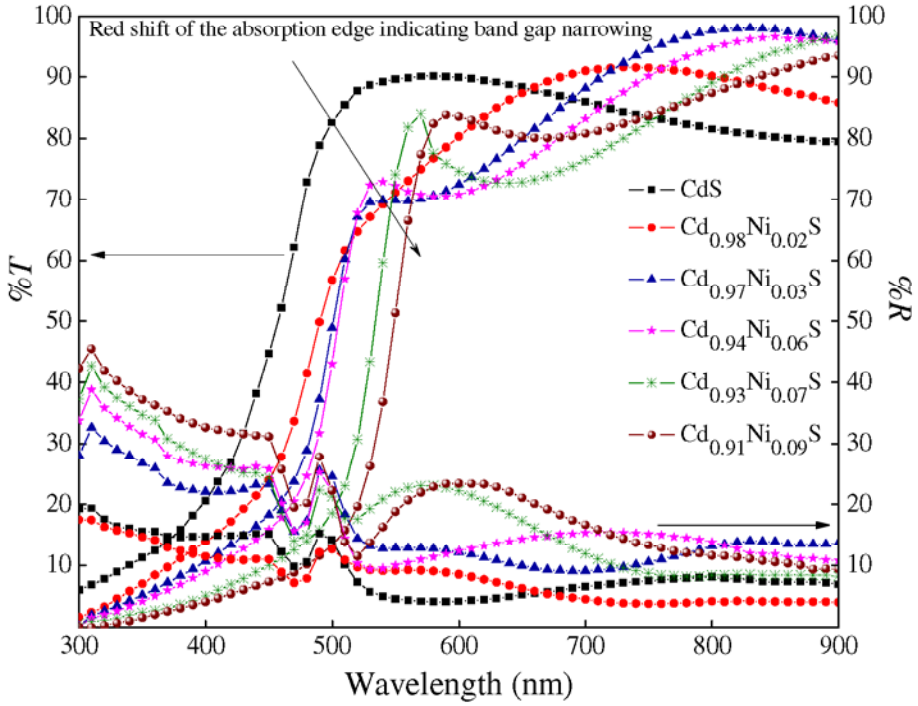

Figure 4.9 *%T* and *%R* spectra for $Cd_{1-x}Ni_xS$ nanofilms ($0 \leq x \leq 0.09$)

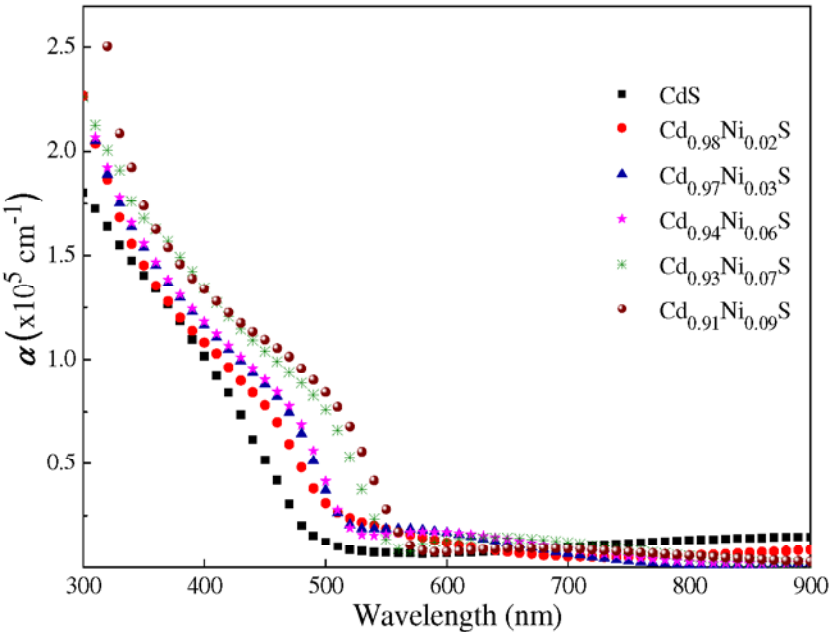

Figure 4.10 The variation of α with wavelength

A sharp fall in $\%T$ (Figure 4.9 & Figure 4.10) near the fundamental absorption edge indicates a direct energy transition in the forbidden gap. The optical band gap (E_g) for direct transition has been determined using Tauc's equation (2.21). The E_g values have been estimated by extrapolating $(\alpha h\nu)^2 \rightarrow 0$ (Figure 4.11). The band gap decreases with increasing Ni content in CdS nanofilms (Table 4.2).

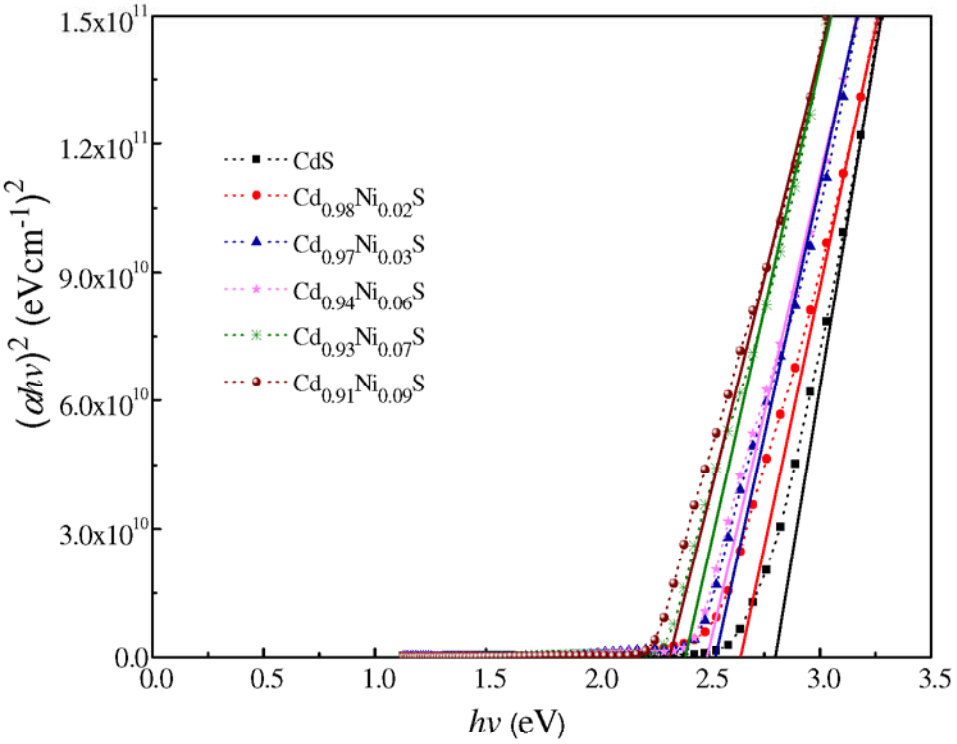

Figure 4.11 Tauc's plot $(\alpha h\nu)^2$ *vs.* $h\nu$ for $Cd_{1-x}Ni_xS$ $(0 \leq x \leq 0.09)$ nanofilms

The variation of $E_g(x_f)$ with film composition (x_f) (Figure 4.12), indicates non–linear behavior and shows bowing phenomenon following Vegard's law [317]

$$E_g(x_f) = x_f E_{NiS} + (1 - x_f)E_{CdS} - bx_f(1 - x_f) \qquad (4.1)$$

where E_{NiS} (= 0.8 eV) is band gap of NiS [318], E_{CdS} is band gap of CdS (experimental) and b (= 2.78 eV) is the bowing parameter defined as the coefficient of parabolic term in phenomenological expression of band gap on doping.

The red shift in band edge on Ni doping (Figure 4.9 and Figure 4.13) indicates the narrowing of band gap even with decrease in crystallite size. This may be attributed to structural disorders, increased tail width of localized states (E_u) (Table 4.2) and *sp–d* hybridization effect. The Ni^{2+} ions in the host CdS crystal form new localized electronic states in the band gap, which arise from the 3*d*–shell of Ni^{2+} ion under the action of surrounding CdS crystal field [312].

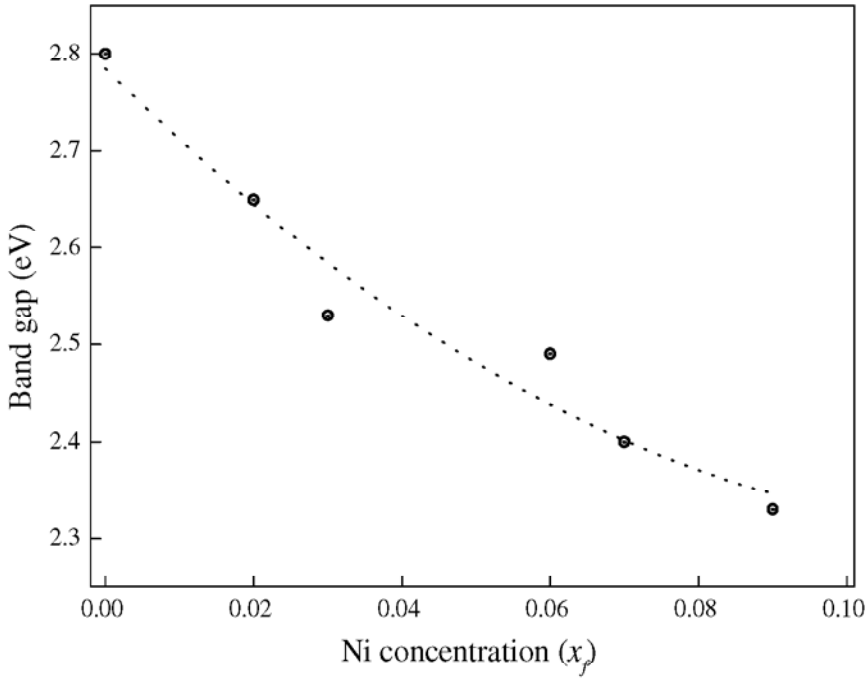

Figure 4.12 The band gap bowing with Ni concentration

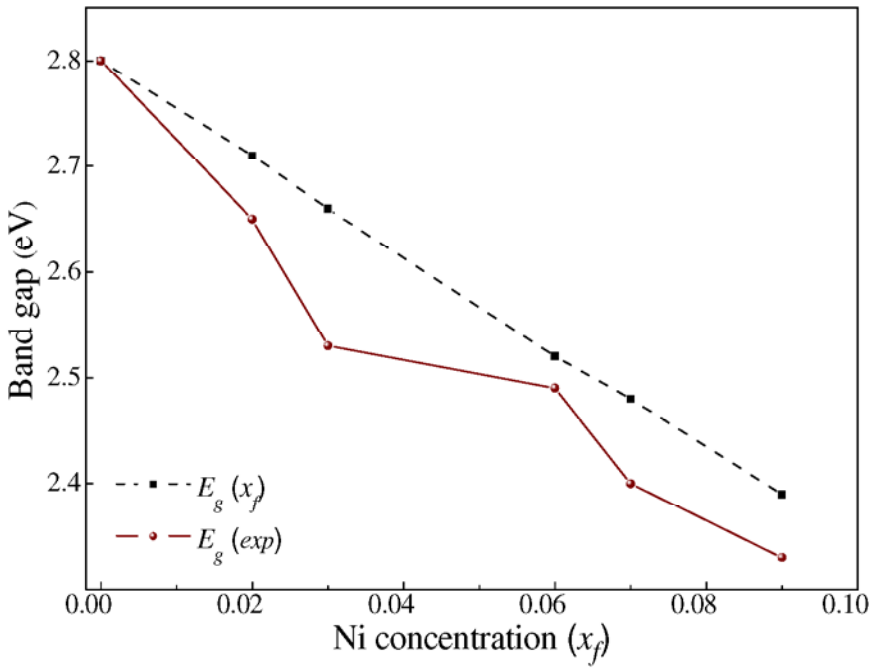

Figure 4.13 Variation of band gap with Ni concentration (x_f)

With an increase in Ni^{2+} ion concentration, the *sp–d* exchange interaction between the band electrons and the localized *d*–electrons of Ni^{2+} ions increase [305,319]. The strength of this interaction strongly depends on the number of *d*–electrons [320]. The reduction of crystallite size with doping of Ni^{2+} ions also leads to an increase in surface to volume ratio. As a result, the surface states corresponding to Ni^{2+} ions in CdS increase and reduce the excitonic emission *via* non–radiative surface recombination [312]. The Ni doping creates high density of impurity states in the nanofilms, which may also perturbate the band structure in the energy gap. The impurity band merges with the nearest intrinsic band and the Fermi level may lie inside the parabolic portion of the valence band [261]. Thus, less energy will be required for the electrons to move from the Fermi level into the conduction band [261].

4.1.2.4 Magnetic analysis

The *M–H* curves (Figure 4.14) obtained using vibrating sample magnetometer at room temperature show the nature of magnetic behaviour in Ni doped CdS semiconductor. This behaviour depends upon the magnitude of Ni^{2+} ion exchange coupling with the electronic levels. The partial substitution of Ni^{2+} ions result in the

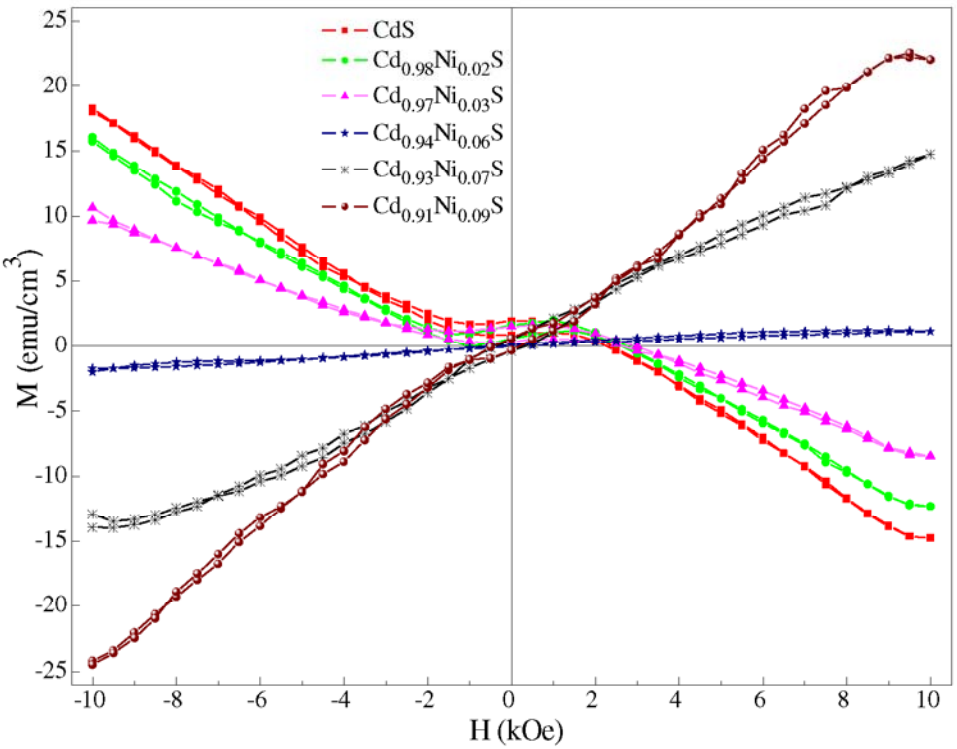

Figure 4.14 *M–H* curves for $Cd_{1-x}Ni_xS$ ($0 \leq x \leq 0.09$) nanofilms

creation of various defects and disorders in the host CdS (Table 4.2) and exhibit diverse magnetic phases ranging from diamagnetic to weak ferromagnetic *via* paramagnetism. For $x < 0.06$, nanofilms exhibit diamagnetic behaviour as illustrated by second quadrant of *M–H* curve (Figure 4.14) with negative magnetic susceptibility (χ_m). The bulk CdS has been reported to show diamagnetic behaviour with $\chi_m = -1.5\times10^{-6}$ cgs [161]. The extent of diamagnetic character goes on decreasing with increase in Ni content. A transition from diamagnetism to para/weak ferromagnetism has been observed for $x \geq 0.06$, as indicated by first quadrant *M–H* curve. For $x \geq 0.06$, *i.e.*, $Cd_{0.94}Ni_{0.06}S$, *M–H* curve is linear which exhibit prominent paramagnetism. However, for $Cd_{0.93}Ni_{0.07}S$ and $Cd_{0.91}Ni_{0.09}S$ nanofilms, the linearity is reduced and a mixture of paramagnetism/weak ferromagnetism is found. The low field *M–H* curve (Figure 4.15) for $x > 0.06$ clearly displays the saturation magnetism (M_s), remanent magnetization (M_r) and coercivity (H_c) (Table 4.3).

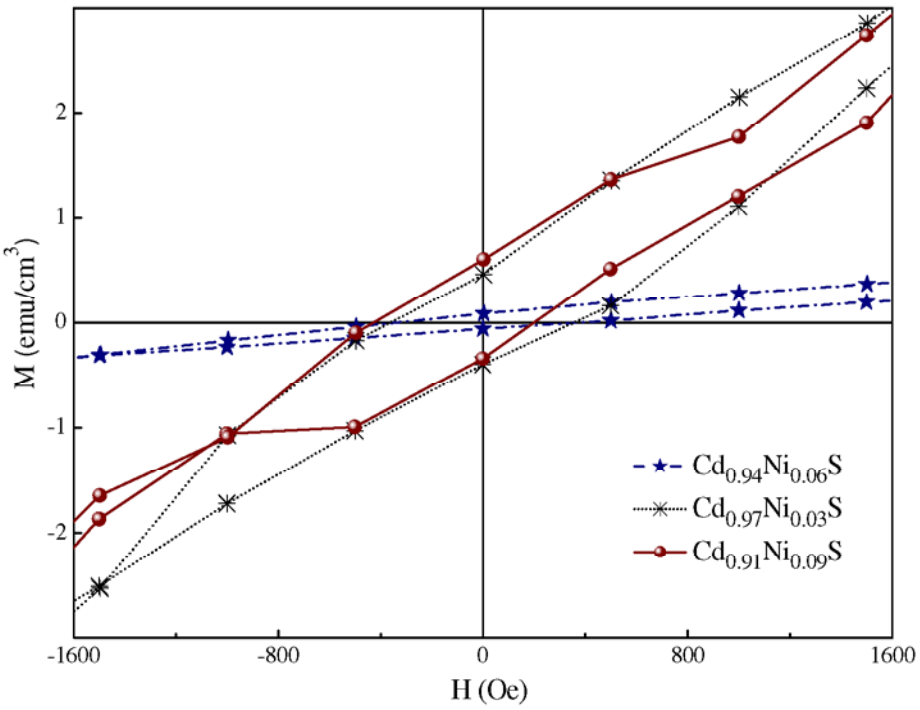

Figure 4.15 Low field *M–H* curves for $Cd_{1-x}Ni_xS$ ($x \geq 0.06$) nanofilms

An increase in para/weak ferromagnetism for $x = 0.07$ and 0.09 is due to an increase in non–equilibrium states for unpaired *d*–orbital electrons with increasing Ni content. This may be due to the replacement of Cd^{2+} ions with Ni^{2+} ions and Ni—Ni exchange interaction at higher Ni content.

Table 4.3 Magnetic parameters; saturation magnetism (M_s), remanent magnetization (M_r), coercivity (H_c) and squareness ratio (M_r/M_s) of $Cd_{1-x}Ni_xS$ ($x \geq 0.06$) nanofilms

Film at x	M_s (emu/cm^3)	M_r (emu/cm^3)	H_c (G)	M_r/M_s
0.06	1.16	0.072	362	0.062
0.07	14.5	0.421	360	0.029
0.09	22.45	0.477	319	0.021

In dilute magnetic semiconductors, the *sp–d* interactions are responsible for magnetism. Since, Ni^{2+} has $3d^8$ spin states, this leads to unoccupied or partially occupied spin up and spin down states. For $x = 0$, the Cd^{2+} has $4d^{10}$ electronic configuration leaving no unpaired *d*–electron. Hence, host CdS with $x = 0$ shows diamagnetic behavior (Figure 4.16). At low Ni concentration ($x = 0.02$ & 0.03), the Ni^{2+} ions are tetrahedrally coordinated to CdS structure, thus increasing the possibility

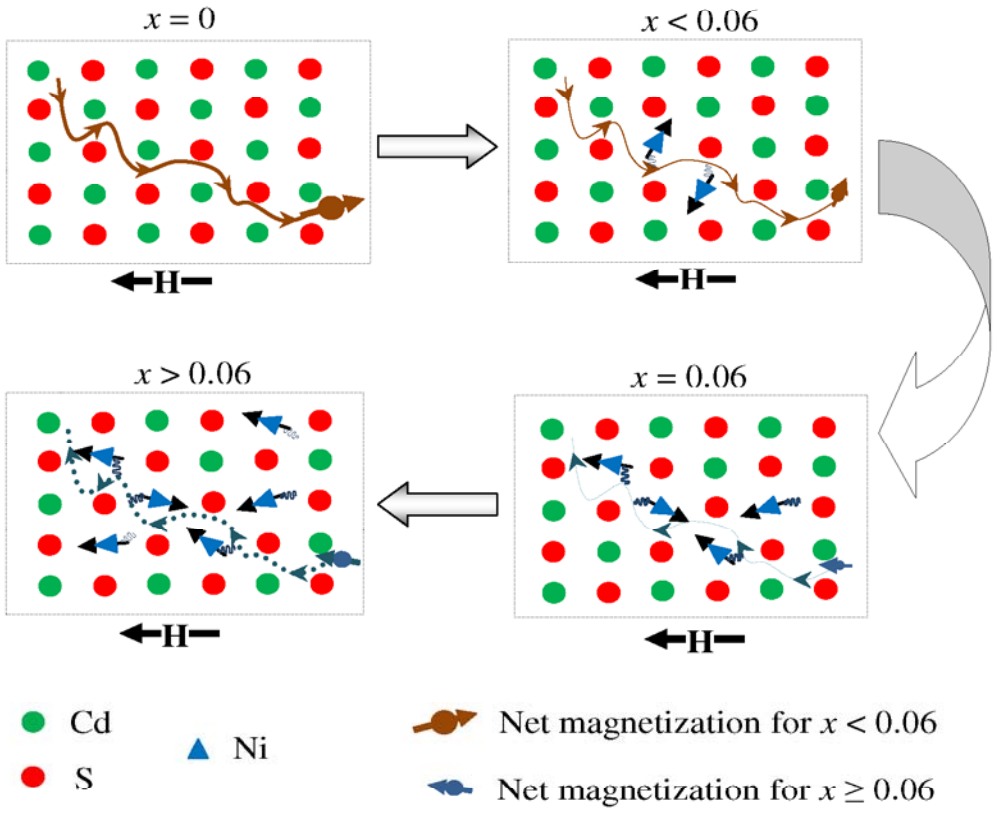

Figure 4.16 Scheme of magnetic behaviour of $Cd_{1-x}Ni_xS$ DMS nanofilms representing: magnetic phase transition (i) prominent diamagnetic phase at $x = 0$ and diminishingly extended upto $x < 0.06$, (ii) paramagnetic phase at $x = 0.06$ and weak ferromagnetic phase for $x > 0.06$

of *sp–d* interaction. But, due to the strong diamagnetic nature of host CdS and the substantial influence of substrate on nanofilms, these films show diamagnetic behaviour (Figure 4.16). For $x = 0.06$, the Ni^{2+} spins act as stray magnetic domains resulting in paramagnetic behavior, with a non–saturated *M–H* curve (Figure 4.14 & Figure 4.15). For $x > 0.06$ (high Ni concentration), the decrease in M_r/M_s values (Table 4.3) is due to an increase in the fraction of paramagnetic Ni^{2+} ions, giving a clear indication of weak ferromagnetism arising due to spin canting (Figure 4.16). Also, Ni^{2+} dopant causes a short range of antiferromagnetic coupling *via* a superexchange *d–d* mechanism. The antiparallel spin of Ni^{2+} ions does not perfectly orient, but, remain canted under the influence of deficient magnetic field. This may be due to induced defects in the lattice associated with reduction in the size of nanocrystallites and an increase in the percentage of spins on the surface [321]. Moreover, spin canting may also be induced due to cationic vacancy disorder on Ni^{2+} substitution in the host CdS lattice. These films exhibit stronger coupling due to an enhanced Ni^{2+} *d*–orbital mixing with the valence and conduction band of the host CdS, splitting the valence band *via* *sp–d* mechanism, conforming to the ferromagnetism. Therefore, for $x \geq 0.06$, *d–d* interactions along with *sp–d* interaction cause a change in the magnetic susceptibility. Thus, high Ni content nanofilms show a transition from dia to para/weak ferro–magnetism.

4.1.3 Conclusion

The Ni content in CdS is responsible for structural disorder and hence, results in degradation of crystallinity. The crystallite size decreases while microstrain and dislocation density increase with increase in Ni content. The Ni^{2+} ions in CdS show change in absorption peak position (~ 650 cm^{-1}) and the strength of respective vibrational bands indicate the incorporation of Ni in host CdS lattice. The surface morphology depends on Ni^{2+} concentration and shows less agglomeration of the crystallites with an increase in grain boundaries and decrease in surface roughness on increasing Ni content. The red shift in band edge on incorporation of Ni^{2+} ions in CdS shows band gap narrowing (2.80 eV to 2.33 eV). A transition in magnetic phase from diamagnetism to para/weak ferromagnetism with Ni content in CdS nanofilms has been observed. *M–H* curves for $x > 0.06$ show remnant magnetization and coercive field. An additional magnetism with an increase in Ni content ($x > 0.06$) comes into play leading to a small ferromagnetic order.

CHAPTER 5

Co doped CdS nanofilms

- **Suresh Kumar**, Pankaj Sharma and Vineet Sharma, "Redshift in Absorption Edge of $Cd_{1-x}Co_xS$ Nanofilms" **IEEE Transactions on Nanotechnology**, 13, 343 (2014).

- **Suresh Kumar**, N.S. Negi, Pankaj Sharma and Vineet Sharma, "Structural, Morphological and Magnetic Analysis of Cd–Co–S Dilute Magnetic Semiconductor Nanofilms" **Journal of Magnetism and Magnetic Materials**, 367, 1 (2014).

JAYPEE UNIVERSITY OF INFORMATION TECHNOLOGY
juit
विद्या तत्व ज्योतिसमः

The functional behavior of dilute magnetic semiconductor (DMS) depends upon the concentration and type of transition metal (TM) doping. TM ions have half metallic character and their presence in semiconductors is able to perturb Fermi energy and lead to band gap tuning. In addition, interaction of 3*d* electrons of TM ions with the free charge carriers of host semiconductor leads to magnetic influence in DMS. In the present chapter, Cobalt has been selected as another TM dopant to study its influence on structural, morphological, optical and magnetic properties in CdS nanofilms.

5.1 Influence of Co^{2+} dopant on CdS nanofilms

Co^{2+} ions have $3d^7$ spin states which lead to unoccupied or partially occupied spin up and spin down states with paramagnetic nature [322]. The Co^{2+} ion has an orbital singlet ground state in tetrahedrally coordinated lattice. The Co^{2+} ions tend to coordinate tetrahedrally in CdS structure by occupying the sites of Cd^{2+} ions. Hence, Co based CdS may be expected to exhibit phenomena related to magnetic ordering. Chandermohan *et al.* have observed that with the increase of Co concentration, from 0.34 at.% – 10.8 at.% in CdS thin films prepared by ion implantation, the optical band gap decreases from 2.39 eV – 2.26 eV [79]. Thambidurai *et al.* have reported that the band gap of 1.20% Co–, 5.02% Co–, and 7.25% Co–doped CdS quantum dots to be 3.91 eV, 3.85 eV and 3.80 eV, respectively in comparision to 3.97 eV of undoped CdS quantum dots [120]. Zhang *et al.* have reported the absence of ferromagnetism in Co ions doped ZnO [323]. Santara *et al.* have reported high temperature ferromagnetism in Co (3% and 8%) doped TiO_2 nanoparticles grown by ball milling method [324]. The magnetic ZnS thin films doped with 2.5% Co fabricated by pulsed laser deposition exhibit a paramagnetic behaviour at room temperature [37]. Therefore, the existence of magnetic behaviour in Co doped DMS is a topic of interest. The influence of Co dopant concentration ($0 \leq x \leq 0.08$) on the structural, morphological, optical and magnetic properties of CdS nanofilms has been investigated.

5.1.1 Experimental details

$Cd_{1-x}Co_xS$ nanofilms have been deposited on glass substrates using CBD at a constant temperature (343 K ± 2 K), *p*H (= 11) for a deposition period of 1 h under constant stirring. Analytical grade reagents (Merck, India), $CdCl_2.H_2O$ (0.02 M;

Cd^{2+} ion source), $SC(NH_2)_2$ (0.04 M; S^{2-} ion source), $CoCl_2.6H_2O$ (Co^{2+} dopant ion source), NH_4OH and TX–100 have been used. The experimental procedure for deposition of undoped CdS nanofilms has been given in sections 3.1.1 and 3.3.1. The Co doped CdS nanofilms have been deposited by adding $CoCl_2$, in Co to Cd ratio $x_m = Co/(Cd + Co)$ varied in the range of 0 – 0.2, into the reaction bath containing the solution for CdS deposition. Few drops of triethanolamine (TEA; 4%) have been added to the final solution to control the release of metal complex during the reaction and to provide better wettability to the substrate. The overall reaction for the deposition of $Cd_{1-x}Co_xS$ films by varying molar concentration of Co^{2+} ions (x) may be expressed as

$$(1-x)[Cd(NH_3)_4^{2+}] + x[Co(NH_3)_4^{2+}] + SC(NH_2)_2 + OH^- \xrightarrow[\text{TEA and TX–100}]{\text{at 343 K \& } p\text{H 11}} (Cd_{1-x}Co_xS)_{film} + CN_2H_2 + 4NH_3\uparrow + 2H_2O$$

After deposition, the films have been washed with acetic acid (5%) ultrasonically to remove the poorly adherent particles and dried out in the air. The obtained films have been found to be yellow in color with good adherence to the substrate. Post deposition annealing of as–deposited films has been performed at 573 K ± 5 K for 2 h.

XRD & FTIR, EDAX, SEM & AFM, UV–Vis–NIR spectrophotometer and VSM have been used for structural, compositional, morphological, optical and magnetic measurements respectively.

5.1.2 Results and discussion

5.1.2.1 Structural analysis

The diffraction peaks for (*100*) and (*002*) reflections in GAXRD spectra for pure and Co doped CdS nanofilms (Figure 5.1) have been indexed to α–CdS structure with hexagonal unit cell in conjunction with other reflection peaks shared by either α–CdS or both α and β–CdS [242]. No characteristic peak associated with cobalt metal, oxides or other cadmium–cobalt metallic phase has been observed within the detection limit of GAXRD. This may suggest that Co content is thoroughly

distributed in $Cd_{1-x}Co_xS$ nanofilms with prominent WZ phase. The existence of multiple reflection peaks shows the polycrystalline nature of the deposited nanofilms with preferred orientation along (*002*) direction.

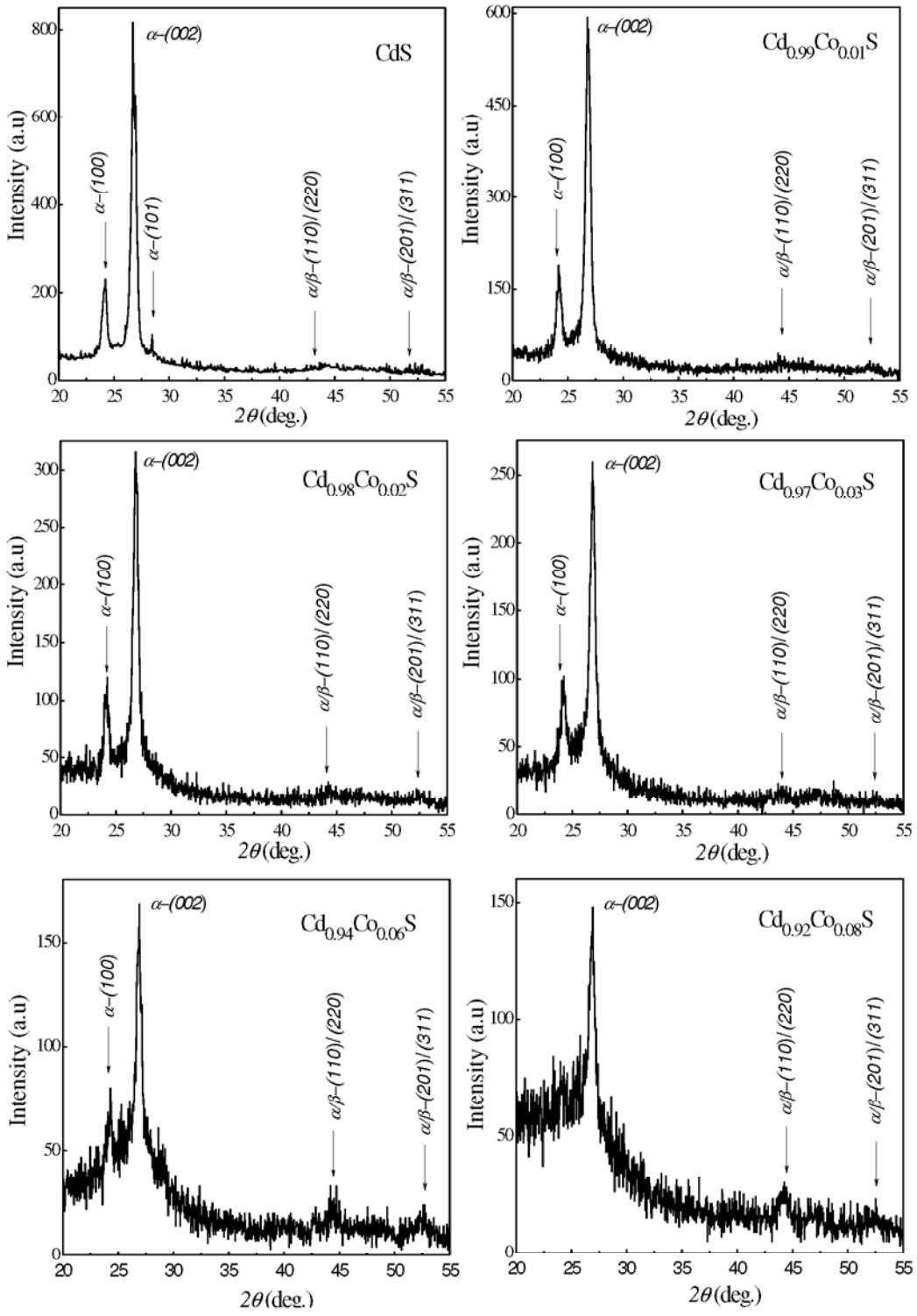

Figure 5.1 GAXRD spectra for $Cd_{1-x}Co_xS$ ($0 \leq x \leq 0.08$) nanofilms

The intensity of reflection peaks of $Cd_{1-x}Co_xS$ nanofilms has been observed to reduce, while the 2θ position of prominent (*002*) peaks (26.74°, 26.76°, 26.81°, 26.85°, 26.91° and 26.94°) shift towards higher 2θ with increase in Co concentration. The shift of GAXRD peaks may be attributed to the incorporation of small Co^{2+} ions (r_{Co}^{2+} = 0.72 Å) into host CdS lattice by occupying the sites of large Cd^{2+} ions (r_{Cd}^{2+} = 0.97 Å) [325]. A similar shift in GAXRD peak with TM doping has also been reported in literature [326]. The decrease in intensity of reflection peaks is related to the change in the scattering intensity of the crystal structure (*hkl*) components and their arrangement in the lattice [215,327]. The substitution of Cd^{2+} ions by Co^{2+} ions may lead to change in the structure factor of CdS lattice, causing the reduction of reflection peak intensity because the atomic scattering factor for Co atom (= 27) is almost half to that of the Cd atom (= 48) [215]. Another possibility for the decrease of diffraction intensity is an increased texturing of the nanofilms [328]. The texture coefficient has been calculated (equation (2.12)) and found to be 2.99, 2.90, 3.23, 3.15, 3.39 and 3.53 for x = 0, 0.01, 0.02, 0.03, 0.06 and 0.08 respectively.

The prominent α–CdS phase in nanofilms remains unaltered with Co addition, but the reflection peaks (Figure 5.1) become broad indicating a decrease in crystallite size and abundance of lattice defects.

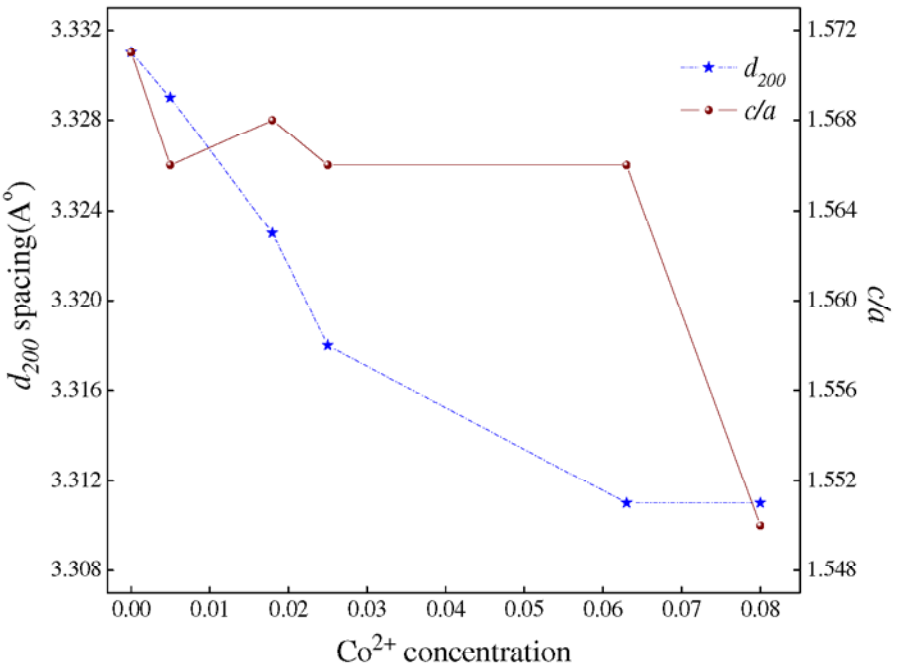

Figure 5.2 Variation of d_{200} spacing and *c/a* ratio with Co concentration

The average crystallite size (D_{hkl}) (Table 5.1) and interplanar spacing (d_{hkl}) (Figure 5.2) have been calculated using *DS* formula (equation 2.9) and Bragg's law (equation 2.1) respectively. The decrease of d_{002}–spacing with increasing Co^{2+} concentration (Figure 5.2) leads to a change in lattice parameters. The lattice parameters ($a = 2d_{100}/\sqrt{3}$ and $c = 2d_{002}$) have been calculated (Table 5.1) using the values of d_{100} and d_{002} respectively [105]. The lattice parameter (c/a) ratio has been observed to be < 5% for the $Cd_{1-x}Co_xS$ nanofilms in comparison to the ideal c/a value

Table 5.1 The values of film thickness (t), Bragg's angle (2θ), interplanar spacing (d_{hkl}), lattice constants (a & c), crystallite size (D_{hkl}), microstrain (ε_{hkl}) and dislocation density (ρ_{hkl}) for $Cd_{1-x}Co_xS$ ($0 \leq x \leq 0.08$) nanofilms

x	t (nm)	2θ (deg.)		d_{hkl} (Å)	Lattice Parameter		D_{hkl} (nm)	ε_{hkl} $\times 10^{-3}$	ρ_{hkl} $\times 10^{15}$ (line/m^2)
		(*100*)	(*002*)		a (Å)	c (Å)			
0.00	55.58	24.22	26.74	3.331	4.240	6.662	16.01	4.161	3.901
0.01	51.21	24.16	26.76	3.329	4.250	6.657	14.33	4.647	4.872
0.02	52.61	24.23	26.81	3.323	4.238	6.645	14.08	4.719	5.044
0.03	59.20	24.24	26.85	3.318	4.236	6.636	13.61	4.875	5.397
0.06	58.25	24.29	26.91	3.311	4.228	6.621	12.76	5.188	6.139
0.08	58.60	24.03	26.94	3.311	4.273	6.621	10.08	6.566	9.833

for WZ CdS structure [242]. A decrease in the value of d_{002} and c/a (Figure 5.2) indicates the incorporation of Co^{2+} ions into CdS lattice and shows lattice contraction. A shrinkage in d_{002} spacing and shift in the position of peaks to higher 2θ values signify that the nanofilms are under tensile strain along the substrate–film interface (*i.e.*, along the (*002*) direction) [329]. This may be due to the substitution of small size Co^{2+} ions taking place more prominently in the α–CdS structure [330]. The substitution of Co^{2+} ions at Cd^{2+} sites and difference of their ionic radii may be responsible for lattice defects. The microstrain (ε_{hkl}) and dislocation density (ρ_{hkl}) of nanofilms have been calculated (Table 5.1). With Co content, ε_{hkl} and ρ_{hkl} increase indicating an increase in lattice defects.

FTIR spectra for $Cd_{1-x}Co_xS$ nanofilms (Figure 5.3) show a broad absorption band in the higher energy region of ~ 3430 cm^{-1} – 3330 cm^{-1} and peaks at ~ 1625 cm^{-1} which have been assigned to O–H stretching [314–316]. The peaks between 895 cm^{-1}

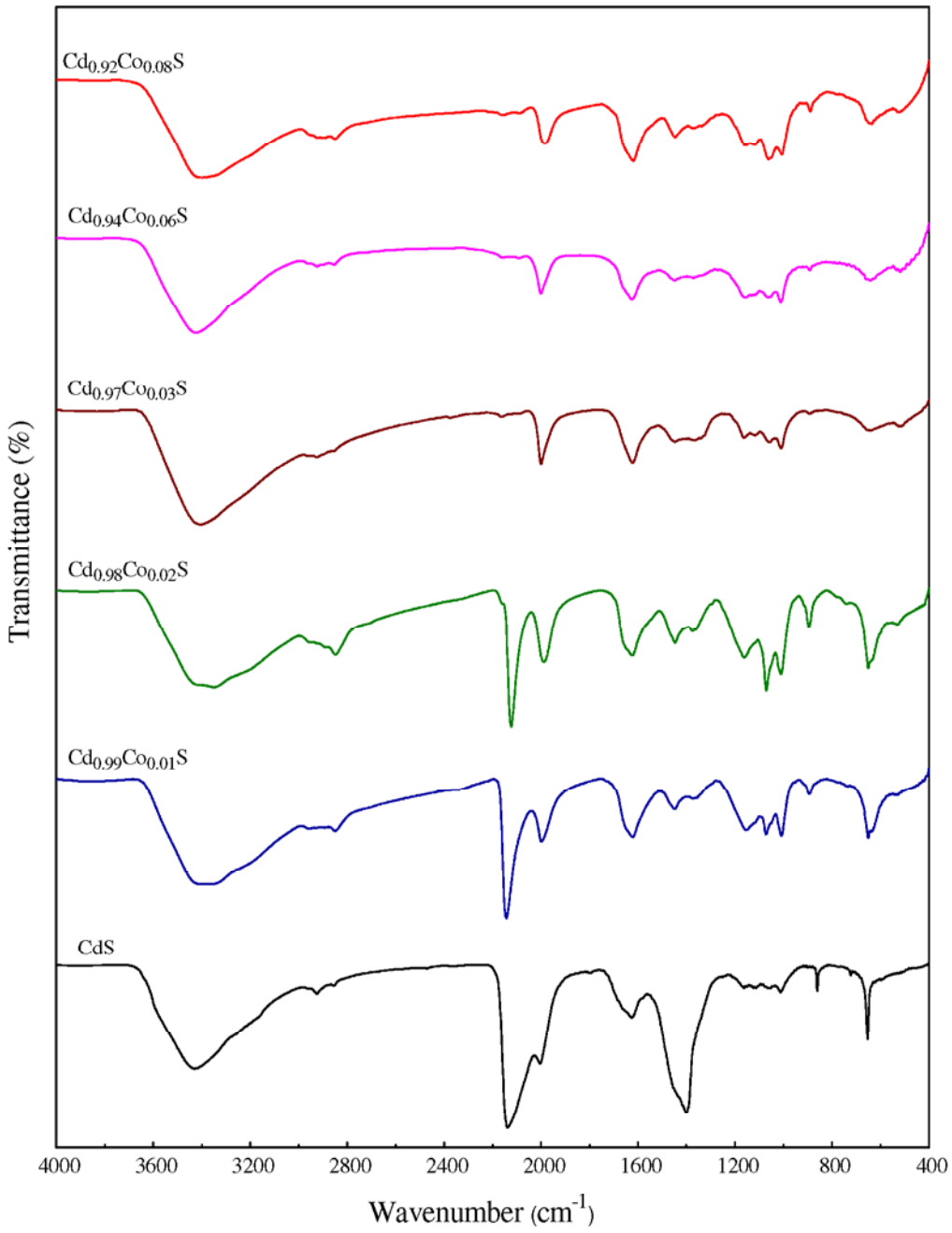

Figure 5.3 FTIR spectra for undoped and Co doped CdS nanofilms

– 860 cm^{-1} belong to O–H out of plane bending of water molecules present in the films. The peaks between ~ 1072 cm^{-1} – 1009 cm^{-1}, ~ 1399 cm^{-1} – 1370 cm^{-1} and ~2160 cm^{-1} – 1900 cm^{-1} belong to the primary amine C–N stretch/C=S of thiourea, the tris–amine C–N stretch shared by C–O stretching and N=C stretch or isothiocyanate (–NCS) formed due to thiourea dissociation respectively [314]. The weak doublet at 2920 cm^{-1} and 2851 cm^{-1} has been assigned to asymmetrical and symmetrical

vibration of CH group while asymmetric scissor deformation vibration lies between 1450 cm^{-1} – 1399 cm^{-1}[316]. For all nanofilms an absorption peak at ~ 650 cm^{-1} associated with Cd–S stretching has been observed [315]. The shift of Cd–S stretch (~ 650 cm^{-1}) towards lower wavenumber (red shift) and decrease of peak intensity *w.r.t.* undoped CdS film indicates the incorporation of Co^{2+} ions in the CdS structure [325]. The lattice of the host CdS semiconductor may be perturbed on the addition of Co^{2+} ions [331]. These perturbations lead to frequency shift depending upon concentration and size of impurity atoms [331]. With increasing Co concentration, the lattice of host CdS become compact leading to red shift of Cd–S stretch.

5.1.2.2 Morphological analysis

The surface morphology of $Cd_{1-x}Co_xS$ nanofilms have been observed by SEM (Figure 5.4). All nanofilms show uniformly distributed nanocrystallites on the surface. The surface of the films is compact, densely packed and continuous. SEM images reveal that the surface morphology of $Cd_{1-x}Co_xS$ nanofilms changes with Co concentration. The introduction of Co^{2+} ions in CdS structure produces substantial surface changes with lesser agglomeration of the crystallites which decreases the compactness and surface roughness while increases the grain boundaries. For $x = 0$, the large CdS crystallites in dense and compact form are observed (Figure 5.4). The Co^{2+} incorporation in CdS results in deterioration of large crystals due to formation of structural defects. With increase in Co concentration ($x \geq 0.01$) a reduction in the crystallite size and compactness has been observed (Figure 5.4 & Table 5.2).

EDAX spectra of $Cd_{1-x}Co_xS$ nanofilms (Figure 5.5) show different peaks ((*K*–series; 2.4 keV for S, 1.8 keV, 7 keV and 7.6 keV for Co) and (*L*–series; 3.2 keV and 4 keV for Cd)) which suggest the presence of Cd, S and Co elements in the deposited films. EDAX analysis reveals that the Co content in $Cd_{1-x}Co_xS$ nanofilms *i.e.*, $x_f = Co/(Cd + Co)$ increases from 0 to 0.08 in accordance with an increase in molar concentration of Co^{2+} ions *i.e.*, $x_m = Co/(Cd + Co)$ in the solution (0 to 0.2) (Figure 5.6). The decreases of Cd content with an increase in Co concentration may be due to the introduction of Co^{2+} ions in CdS structure (Table 5.2). The fractional presence of Co^{2+} ions may also be seen from the low intensity peak in EDAX *w.r.t.* Cd and S (Figure 5.5). The remaining peaks in EDAX spectra correspond to various elements (mainly Si, O and C etc.) present in the glass substrate and carbon coating.

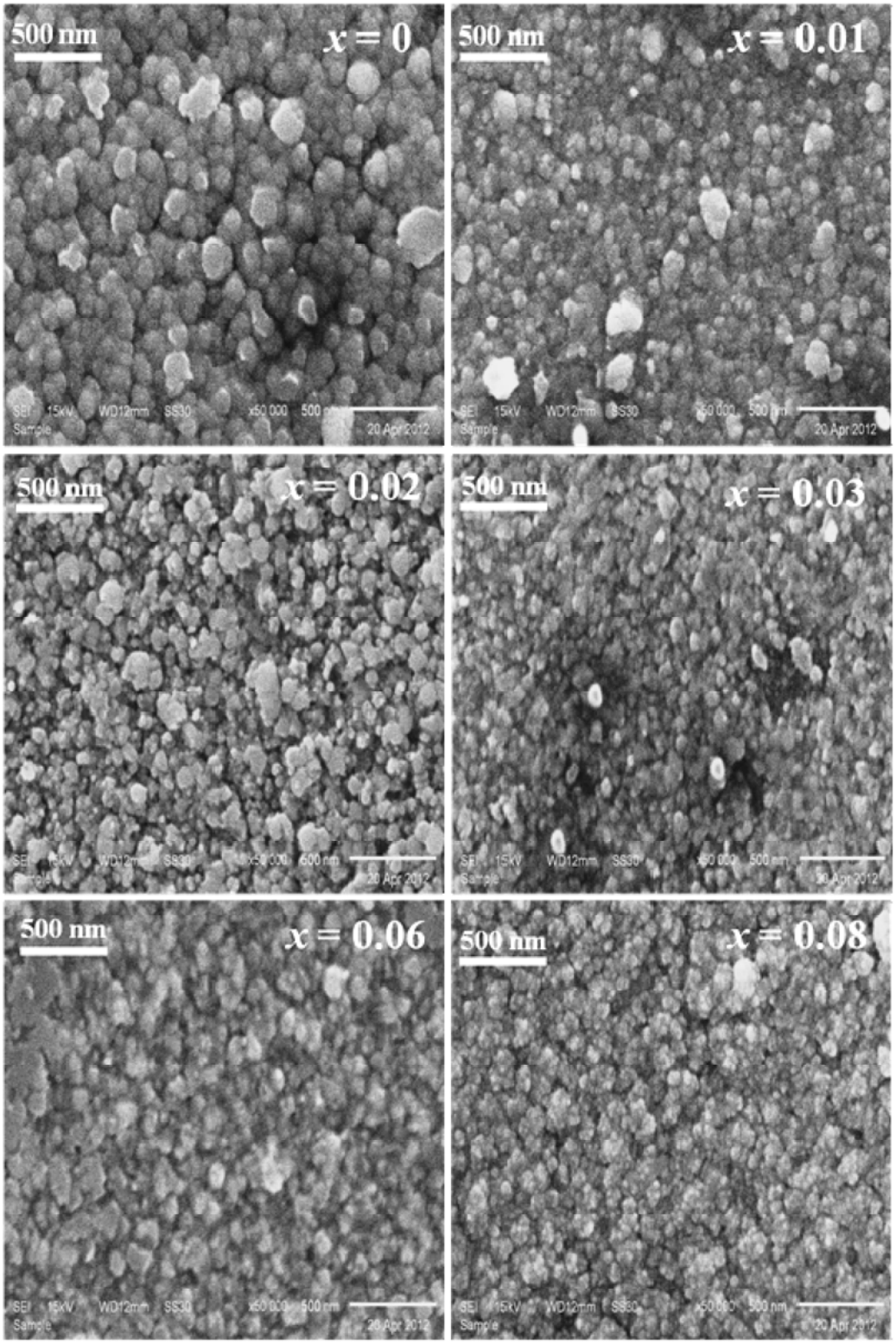

Figure 5.4 SEM micrographs for $Cd_{1-x}Co_xS$ ($0 \leq x \leq 0.08$) nanofilms

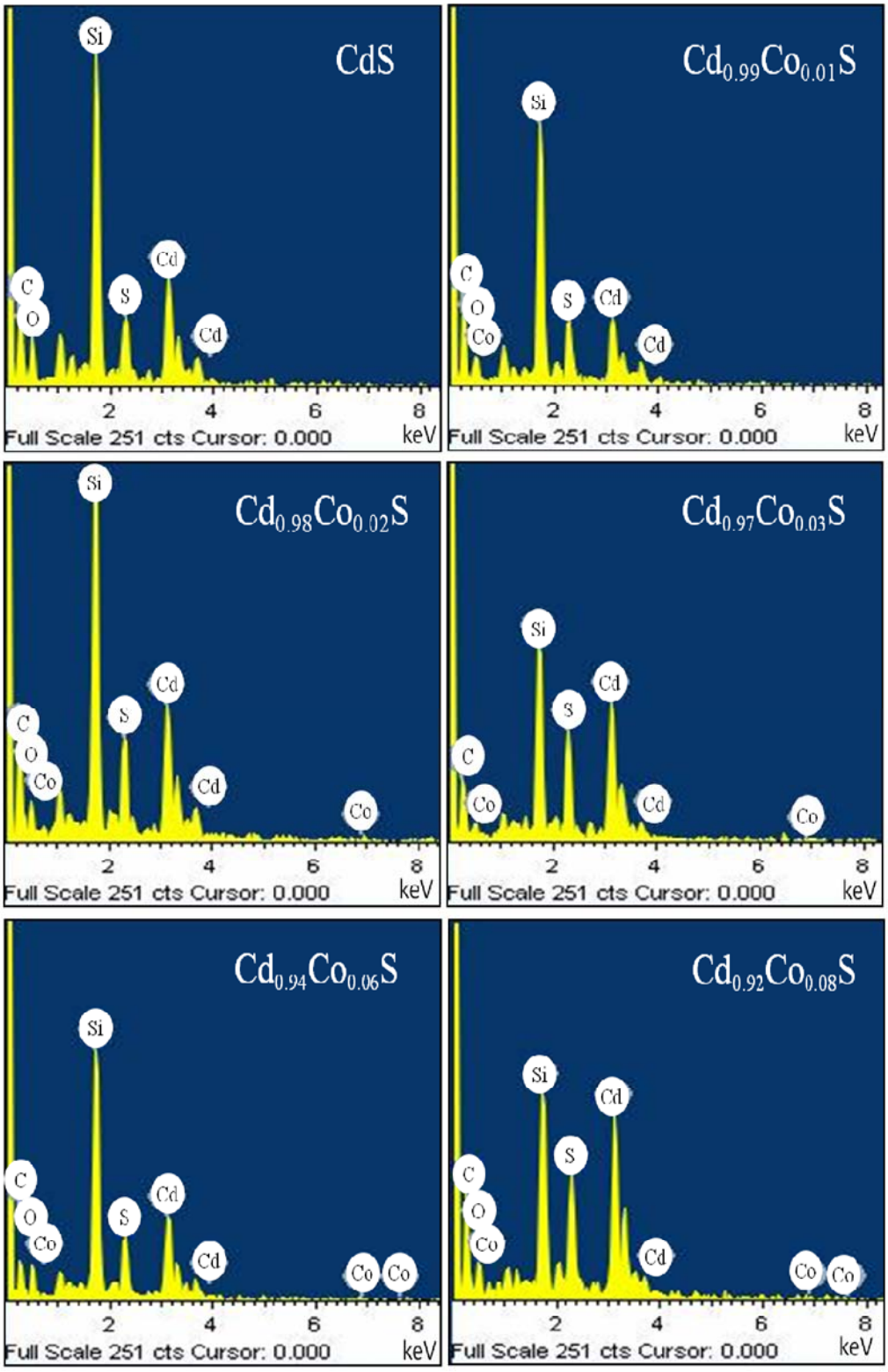

Figure 5.5 EDAX spectra for $Cd_{1-x}Co_xS$ ($0 \leq x \leq 0.08$) nanofilms

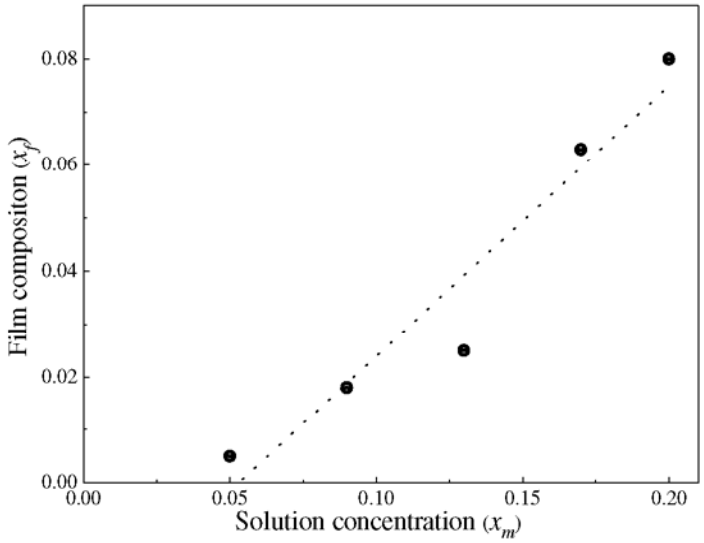

Figure 5.6 Plot of solution concentration from molarities and film composition from EDAX for $Cd_{1-x}Co_xS$ nanofilms

Figure 5.7 and 5.8 show 2D and 3D images respectively for $Cd_{1-x}Co_xS$ nanofilms obtained by AFM. AFM study reveals that the crystallite size (D_{AFM}) and root mean square roughness (R_{rms}) of $Cd_{1-x}Co_xS$ nanofilms vary with Co concentration (Table 5.2). Undoped CdS nanofilm possesses larger crystallites and high surface roughness (Figure 5.7(a) and 5.8(a)). However, with the increase in Co concentration ($x \geq 0.01$), D_{AFM} of nanofilms decreases (Figure 5.7(b–f)). From Figure 5.7 it is clear that the morphology of nanofilms change beyond $x = 0.02$ which may be due to the phase separation with increase in Co concentration. R_{rms} decreases with increasing Co concentration (Figure 5.8(a–c)) and reaches a minimum of 6.16 nm for $x = 0.02$ and then increases for $x > 0.02$ (Figure 5.8(d–f)). The change in the R_{rms} with varying Co^{2+}

Table 5.2 Composition and morphological parameters for $Cd_{1-x}Co_xS$ ($0 \leq x \leq 0.08$) nanofilms

Film	Composition (at.%)			D_{AFM} (nm)	R_{rms} (nm)	S_{sk}	S_{ka}
	Cd	Co	S				
CdS	50.64	0	49.36	21.5	8.26	1.02	3.04
$Cd_{0.99}Co_{0.01}S$	50.52	0.46	49.02	19.3	7.42	0.94	3.23
$Cd_{0.98}Co_{0.02}S$	49.66	0.91	49.43	18.8	6.16	0.64	2.87
$Cd_{0.97}Co_{0.03}S$	48.85	1.31	49.84	16.3	7.72	0.79	2.75
$Cd_{0.94}Co_{0.06}S$	47.65	3.21	49.14	15.8	8.28	0.49	2.63
$Cd_{0.92}Co_{0.08}S$	47.26	4.12	48.62	12.2	8.85	0.66	2.89

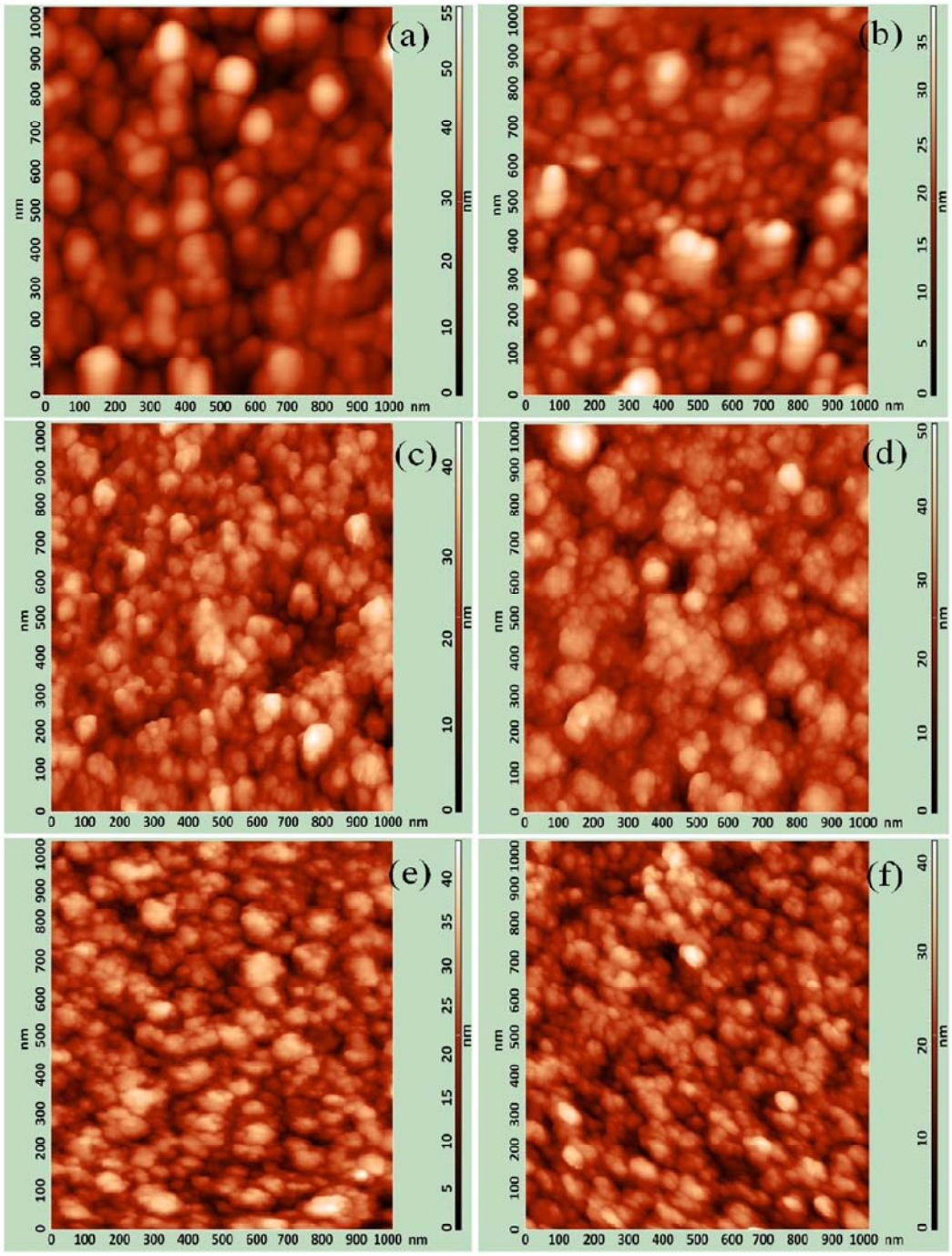

Figure 5.7 2D AFM images for $Cd_{1-x}Co_xS$ nanofilms ((a): x = 0, (b): x = 0.01, (c): x = 0.02, (d): x = 0.03, (e): x = 0.06 and (f): x = 0.08)

concentration may be due to the random distribution of Co^{2+} ions in the CdS structure signified by the variation of peak to valley distribution in the film morphology (Figure 5.8(a–f)). The low surface skewness (S_{sk}) and kurtosis coefficient (S_{ka}) values for all nanofilms (Table 5.2) indicate that height distribution is uniform, with approximately

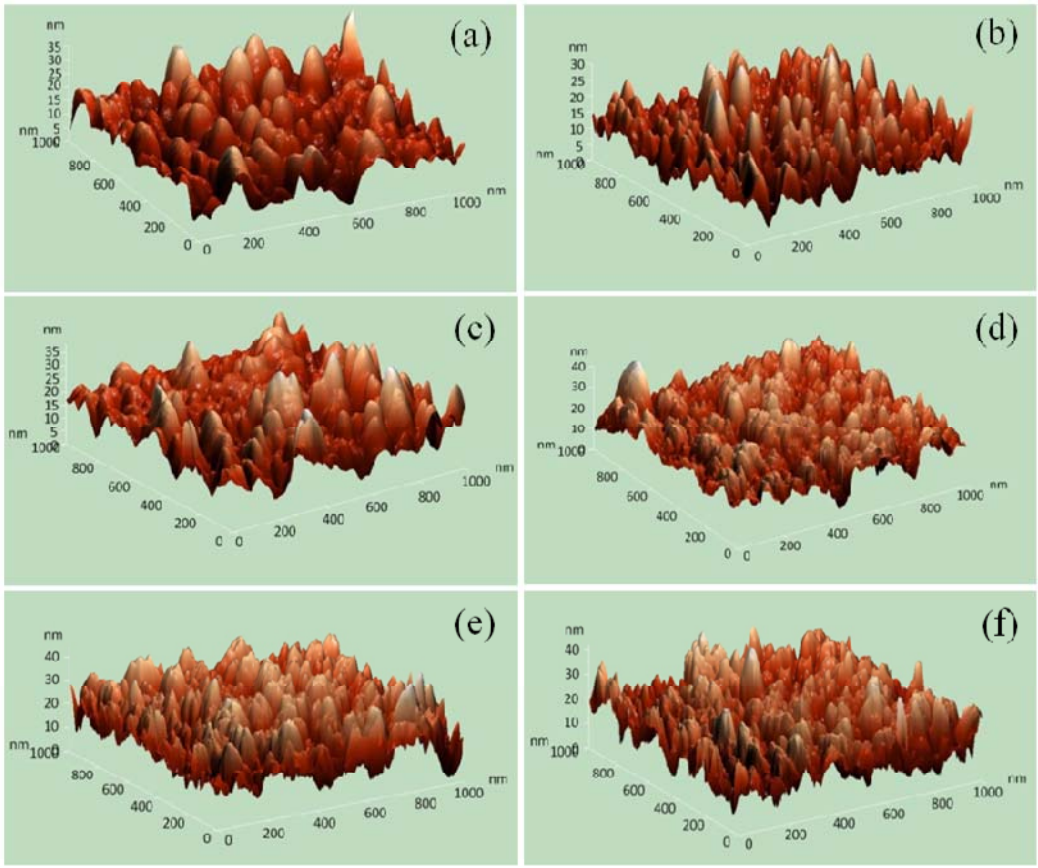

Figure 5.8 3D AFM images for $Cd_{1-x}Co_xS$ nanofilms ((a): x = 0, (b): x = 0.01, (c): x = 0.02, (d): x = 0.03, (e): x = 0.06 and (f): x = 0.08)

equal number of high peaks to deep valleys over the scanned area (1×1 μm^2) [332]. 3D AFM images (Figure 5.8(a–f)) show that the deposited films grow with columnar structures along the *c*–axis perpendicular to the substrate which confirms the prominent WZ structure in the $Cd_{1-x}Co_xS$ nanofilms [287]. This is also supported by high intensity curve at (*100*) and (*002*) reflection in XRD spectra (Figure 5.1).

5.1.2.3 Optical analysis

Figure 5.9 shows *%T* and *%R* spectra of $Cd_{1-x}Co_xS$ nanofilms. The *%T* of $Cd_{1-x}Co_xS$ nanofilms in the wavelength range 500 nm – 900 nm varies with increasing Co concentration. This variation may be attributed to an increase in structural disorder due to deteriorating the crystallite size (Figure 5.7), which leads to enhanced absorption/scattering of light. Further, the increase of Co^{2+} ions in CdS structure may cause the localization of light due to the formation of traps (point defects) for optical confinement [333]. The occurrence of low interference patterns in *%T* spectra indicate that deposited nanofilms are ultra thin, smooth and homogeneous.

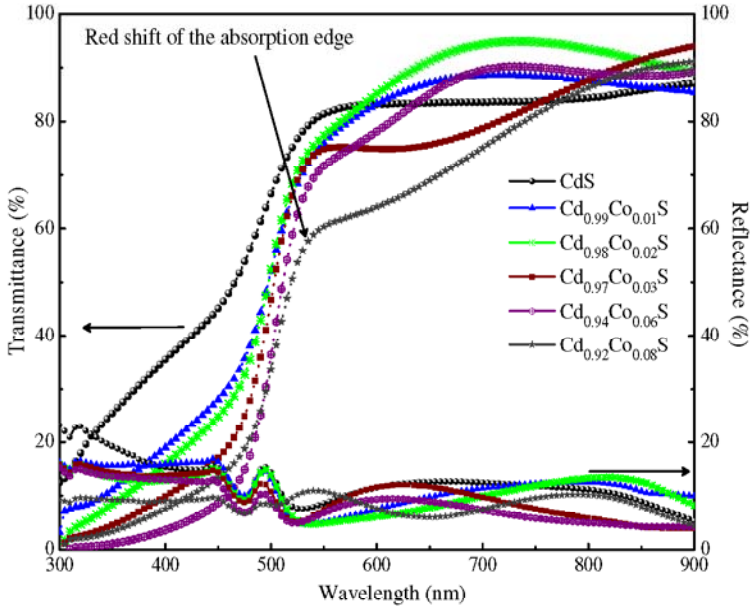

Figure 5.9 Transmittance (%) and reflectance (%) spectra for $Cd_{1-x}Co_xS$ nanofilms

The values of absorption coefficient (α) at a frequency of radiation has been calculated using equation (2.19) and found to be ~ 10^5 cm^{-1} in the visible region. The value of α at absorption edge increases with increasing Co content (Table 5.3). This may be attributed to the decrease in crystallite size which provides large collective surface area and number of absorption/scattering centers for light. A sharp fall in $\%T$ (Figure 5.9) near the fundamental absorption edge indicates a direct energy transition in the forbidden gap [294]. However, the absorption edge is red shifted with increasing Co concentration (Figure 5.9).

Table 5.3 The values of absorption coefficient (α), optical band gap (E_g), Urbach energy (E_u) and structural disorder (X) for $Cd_{1-x}Co_xS$ ($0 \leq x \leq 0.08$) nanofilms

Film	$\alpha \times 10^5$ (cm^{-1})	E_g (eV)	E_u (eV)	X
CdS	1.31	2.88	0.497	46.31
$Cd_{0.99}Co_{0.01}S$	1.74	2.64	0.524	48.88
$Cd_{0.98}Co_{0.02}S$	1.80	2.60	0.533	49.74
$Cd_{0.97}Co_{0.03}S$	1.95	2.61	0.575	53.74
$Cd_{0.94}Co_{0.06}S$	2.51	2.46	0.617	57.74
$Cd_{0.92}Co_{0.08}S$	2.68	2.43	0.705	66.12

According to the inter–band transition theory, the optical band gap (E_g) for direct transition can be determined using Tauc's equation (2.21). The E_g values have been estimated by extrapolating the straight line of plot $(\alpha hv)^2$ *vs.* hv to $(\alpha hv)^2 \rightarrow 0$ (Figure 5.10). All plots show a straight line (for $\alpha \geq 10^4$ cm^{-1}) signifying direct allowed band gap transition in $Cd_{1-x}Co_xS$ nanofilms. A decrease of band gap on Co doping in CdS nanofilms has been observed. Similar behavior of band gap in DMS has been reported [79,302,325].

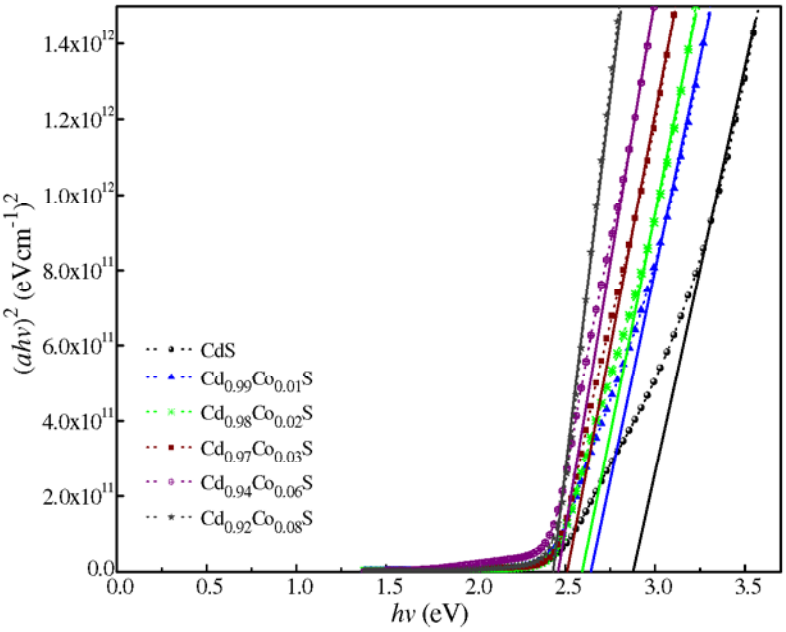

Figure 5.10 Plot $(\alpha hv)^2$ *vs.* hv for $Cd_{1-x}Co_xS$ nanofilms

The absorption profile within the band tail region can be explained in terms of Urbach energy (E_u) by Urbach–Martienssen model equation (2.22). E_u originates from the structural disorders, compositional fluctuations, point defects (e.g., vacancies, interstitials, and antisites defects), grain boundaries, strain etc. [79]. The value of E_u has been calculated from the plot of $ln(\alpha)$ *vs.* hv (Figure 5.11). An increase in the value of E_u with increasing Co concentration has been found (Table 5.3).

According to Cody's model, the Urbach energy is related to degree of structural disorder, lattice ionicity and temperature as [334]

$$E_u = \frac{E_p}{2\sigma_o}\left[X + \coth\left(\frac{E_p}{2k_BT}\right)\right] \tag{5.1}$$

where T is the room temperature (300 K), E_p the photon energy (25 meV) [334] and k_B the Boltzmann constant (1.38×10^{-23} J/K). The parameter σ_o depends on lattice

ionicity of material (1.19) [334]. *X* is a measure of structure disorders and its values with Co^{2+} concentration are given in Table 5.3. An increase in the value of E_u and *X* with Co content may be attributed to the creation of more and more localized states within the tail region of valence and conduction band.

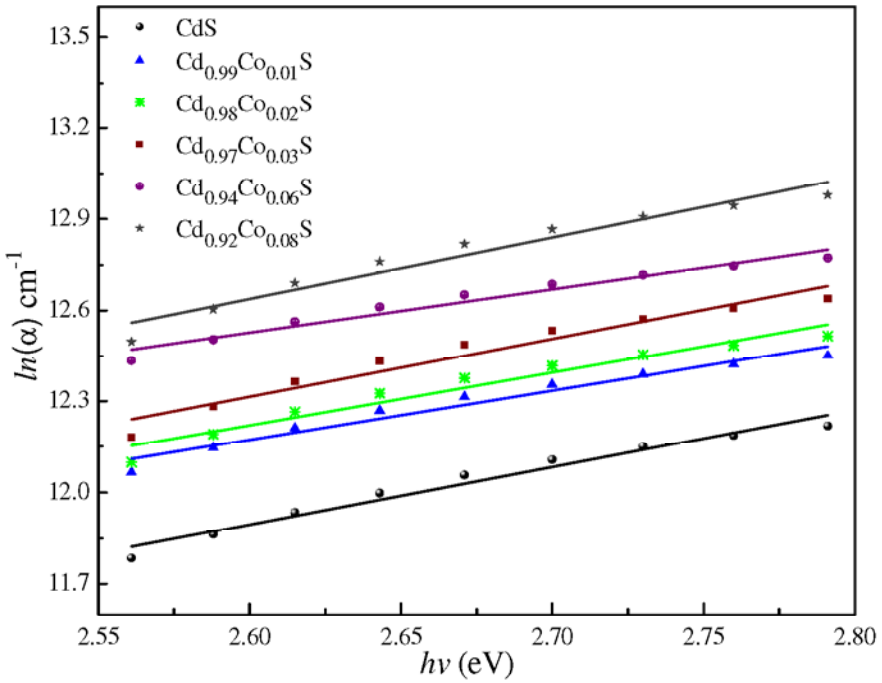

Figure 5.11 Plot $ln(\alpha)$ *vs. hv* for $Cd_{1-x}Co_xS$ ($0 \leq x \leq 0.08$) nanofilms

The variation of $E_g(x_f)$ with composition (x_f), indicates non–linear behaviour showing bowing phenomenon following Vegard's law, (Figure 5.12) as [317]

$$E_g(x_f) = x_f E_{CoS} + (1 - x_f)E_{CdS} - bx_f(1 - x_f) \qquad (5.2)$$

where x_f is film composition, E_{CoS} is band gap of CoS (0.6 eV) [318], E_{CdS} is band gap of CdS. *b* is the bowing parameter and its value has been calculated to be 2.83 eV. The variation of band gap with increasing Co concentration (Figure 5.12) indicates that both experimental and theoretical observations for band gap show similar behaviour.

The red shift of band edge in Co added CdS (Figure 5.9 and Figure 5.10) clearly indicate the narrowing of optical band gap. This may be attributed to increase in impurities, structural disorders, increased tail width of localized states and may be explained by *sp–d* hybridization effect [319]. Co^{2+} ions in host CdS form new localized electronic states in the band–gap region, which arise from the *3d*–shell of Co^{2+} ions under the action of surrounding CdS crystal field [320]. With an increase in

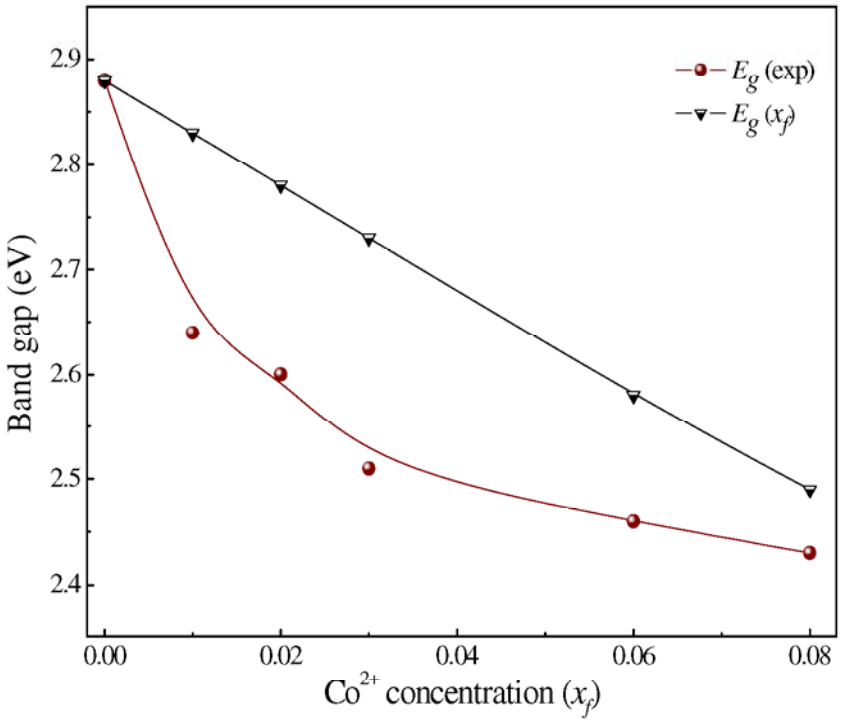

Figure 5.12 Band gap dependence on Co^{2+} concentration (x_f) for $Cd_{1-x}Co_xS$ nanofilms

Co^{2+} ions concentration, the *sp–d* exchange interaction (*sp–d* hybridization effect) between the band electrons and the localized *d*–electrons of Co^{2+} ions increases. The strength of this interaction strongly depends on the number of *d*–electrons [320]. The Co doping creates high density of impurity states in the nanofilms, which may also perturb the band structure in the energy gap. The impurity band merges with the nearest intrinsic filled band and the Fermi level may lie inside the parabolic portion of the valence band for *n*–type dopant [261]. Thus, less energy will be required for the electrons to move from the Fermi level to the conduction band.

5.1.2.4 Magnetic analysis

The field dependent magnetization (*M–H* curves) of $Cd_{1-x}Co_xS$ nanofilms at room temperature (Figure 5.13) have been calculated after subtracting the diamagnetic contribution of the glass substrate. The magnetic parameters like saturation magnetization (M_s), remanent magnetization (M_r), magnetic coercivity (H_c) and squareness ratio (M_r/M_s) have been calculated from *M–H* curves. The magnetic properties in DMS strongly depend on different factors such as concentration of TM impurities, defect structure, secondary phase formation and metallic clustering, etc.

[79]. Since, no impurity peak or secondary phase formation has been observed in the GAXRD spectra, therefore, the magnetic behaviour of the nanofilms may be associated with Co^{2+} ion concentration and the lattice defects/disorders evolved thereof. In CdS, Cd^{2+} has electronic configuration $4d^{10}$ with fully paired *d*–electrons. Hence, CdS shows diamagnetic behavior and same has been detected in experimental results (Figure 5.13).

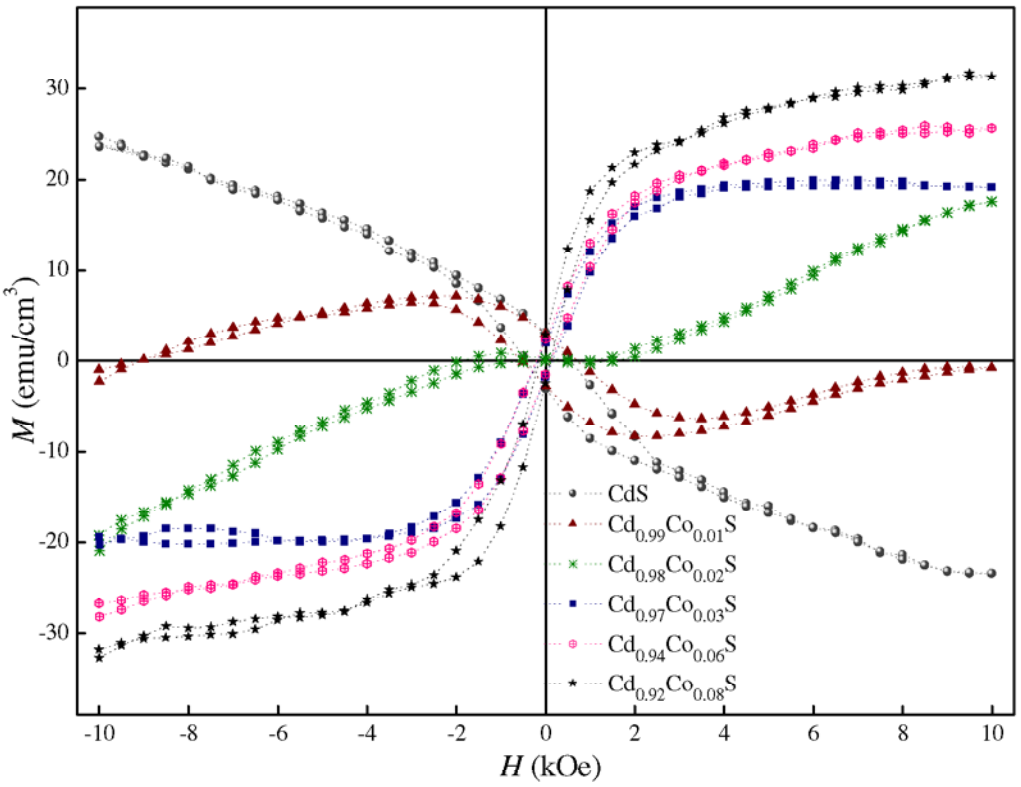

Figure 5.13 Room temperature *M–H* curves for $Cd_{1-x}Co_xS$ ($0 \leq x \leq 0.08$) nanofilms

The diamagnetism in pure CdS (bulk) with magnetic susceptibility of -1.5×10^{-6} (cgs units) has already been reported [159,161]. For $x = 0.01$, the observation of an anti S–type *M–H* curve (Figure 5.13) indicates that the nanofilm is still in diamagnetic state. The existence of diamagnetism in $x = 0.01$ may be due to strong influence of the host CdS towards magnetic behaviour. For $x = 0.02$, the *M–H* curve (Figure 5.13 and inset of Figure 5.14) exhibits linearity in hysteresis indicating paramagnetic state. The lattice defects (vacancies or interstitials) induced by Co^{2+} ion in the CdS structure may be responsible for the progressive alignment of the neighboring Co^{2+} pair spin components along the direction of magnetic field. Consequently, the Co^{2+} ions exhibit nearest–neighbor interaction *via* superexchange

mechanism resulting in short range anti–ferromagnetic coupling in them and the spins remain canted to some extent [322]. Hence, no significant hysteresis is observed for $x = 0.02$. The nanofilms acquire enhanced magnetic properties (*i.e.*, definite value of M_s, M_r and H_c) with further increase of Co content ($x > 0.02$) in the CdS structure. As a result, the *M–H* curve gradually makes transition into S–type hysteresis, indicating the growth of ferromagnetic long range order in Co doped CdS films. For $x > 0.02$, the narrow magnetic hysteresis loop shows a clear transition to ferromagnetic state in these films (Figure 5.13).

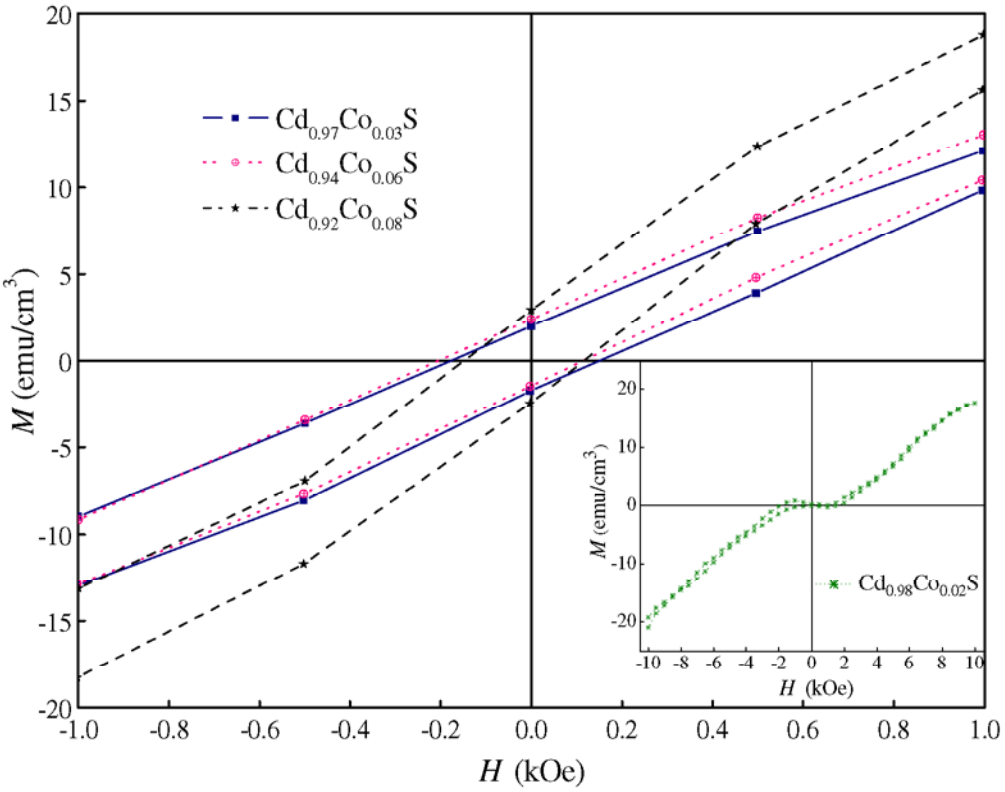

Figure 5.14 Low field *M–H* curves of $Cd_{1-x}Co_xS$ nanofilms for $x \geq 0.03$ and inset show *M–H* curve for $Cd_{0.98}Co_{0.02}S$ nanofilm

The calculated values of saturation magnetism (M_s), remanent magnetization (M_r), coercivity (H_c) and squareness ratio (M_r/M_s) of $Cd_{1-x}Co_xS$ ($x > 0.02$) nanofilms are listed in Table 5.4. The squareness ratio (M_r/M_s) represents how square the hysteresis loop is and has been found to be very low ($M_r/M_s \leq 0.09$) for $x > 0.02$. The M_s and M_r increase while H_c decreases with increase in Co concentration for $x > 0.02$. The low values of H_c and M_r/M_s indicate that $Cd_{1-x}Co_xS$ nanofilms for $x > 0.02$ exhibit soft magnetic behavior which increases with cobalt content [335].

For $x > 0.02$, the free delocalized carriers of host CdS lattice and the localized *d* spins of Co^{2+} ions interact through a double exchange interaction mechanism (*sp–d*) [151,322] and become stronger with Co content. This exchange interaction leads to the spin polarization of the free delocalized carriers with local spin polarized electrons of Co^{2+} ions in the same spin direction under the influence of external magnetic field [151], which results in ferromagnetism for $x > 0.02$. It has been reported that M_s values for oxide based DMS lie in the range of 1 emu/cm^3 – 10 emu/cm^3 [336], but, in the present case the range of M_s lies in ~ 20 emu/cm^3 – 30 emu/cm^3 for $x > 0.02$.

Table 5.4 Magnetic parameters: saturation magnetism (M_s), remanent magnetization (M_r), coercivity (H_c) and squareness ratio (M_r/M_s) of $Cd_{1-x}Co_xS$ ($x > 0.02$) nanofilms

Film	M_s (emu/cm^3)	M_r (emu/cm^3)	H_c (G)	M_r/M_s
$Cd_{0.97}Co_{0.03}S$	19.65	1.84	164.87	0.09
$Cd_{0.94}Co_{0.06}S$	25.33	1.94	160.94	0.08
$Cd_{0.92}Co_{0.08}S$	29.78	2.41	131.84	0.09

Moreover, the decrease in the crystallite size with Co content enhances the surface spin disorder in the films because of lattice defects/disorder associated with the increase in microstrain and dislocations (Table 5.1) [337,338]. Thus, the increase in percentage of spins on the surface may generate magnetic frustration in the films enhancing the ferromagnetism. This results in hysteresis loop that appears along hard axis for $x > 0.02$. Therefore, the substitution of Co^{2+}in CdS leads to the spin–orbit interaction for doping $x > 0.02$, which induces ferromagnetism in $Cd_{1-x}Co_xS$ nanofilms.

5.1.3 Conclusion

The lattice defects associated with the introduction of Co^{2+} ions in CdS lattice bring significant structural and morphological changes. The introduction of Co^{2+} in CdS structure increases structural disorder and hence, results in degradation of crystallinity. The incorporation of Co^{2+} ions in CdS lattice deteriorates large crystallites, decreasing the surface roughness with an increase in grain boundaries. $Cd_{1-x}Co_xS$ nanofilms show columnar growth of crystallites oriented along (*002*) reflection plane indicating prominent WZ structure. A red shift in the peak position of Cd–S stretch may be due to incorporation of Co^{2+} ions in CdS lattice. A red shift in

the absorption edge of transmission spectra makes the optical band gap shift from 2.88 eV to 2.43 eV with increasing Co^{2+} concentration. The diamagnetic state of CdS vanishes with increasing Co content for $x = 0.02$ and a transition to ferromagnetic state for $x > 0.02$ has been observed which may be due to the induced lattice defects, phase separation and *sp–d* exchange interaction.

CHAPTER 6

Summary

JAYPEE UNIVERSITY OF INFORMATION TECHNOLOGY
juit
विद्या तत्व ज्योतिसमः

Nanofilms are strongly influenced by surface/interface effects and have a wide range of applications in modern world. Understanding the behavior of nanofilms in relation to their structure, morphology, optical and magnetic response is of greater importance. CdS is II–VI semiconductor. CdS films are promising candidate for optoelectronics and photovoltaics applications. Transition metal doping in CdS increase its potential towards spintronics. In this work, pure and transition metal doped CdS nanofilms have been deposited *via* chemical bath deposition technique. The Ni^{2+} and Co^{2+} ions have been selected as transition metal dopants. The deposited nanofilms have been studied for structural, morphological, optical and magnetic properties.

The nanopowder and nanofilm of CdS have been synthesized simultaneously using chemical bath deposition. The nanopowder has low texture and weakly crystalline nanocrystallites while, the nanofilm has high texture and strongly crystalline nanocrystallites. CdS nanocrystallites growth is better in the nanofilm in comparison to nanopowder.

The effect of annealing temperature on CdS nanofilms results in an enhancement of coalescence of small crystallites, reduction of defects and densification of the nanofilms. The optical band gap decreases with increase in annealing temperature.

The S/Cd molar ratio (0.05, 1, 2, 3, 4 and 5) affects the film formation with variation in structure, morphology and optical behaviour of CdS nanofilms. A phase transition has been observed with varying S/Cd molar ratio. The observed band gap *v*alues are more than that of bulk CdS. The nanofilms for S/Cd = 2 show minimum crystallite size and maximum blue shift.

The effect of deposition temperature (323 K, 333 K, 343 K, 353 K and 363 K) on CdS nanofilms results in wurtzite (α–CdS), zinc blende (β–CdS) and polymorph (α/β–CdS) structures. The CdS nanofilms deposited at 343 K, shows polymorph structure with better morphology, low crystallite size (~ 20 nm), high stoichiometry, higher band gap (2.88 eV) and minimum disorder.

CdS nanofilms of different thickness have been studied. Nanofilms show an increase in crystallite size and lattice parameter relaxing the inherent strain and dislocations with increase in film thickness. The crystallization and orientation of the crystal growth gets enhanced with increase in film thickness. The optical band gap

decreases, whereas the refractive index and extinction coefficient shows normal dispersion and increase with an increase in film thickness.

The substitution of Ni^{2+} ions in CdS ($Cd_{1-x}Ni_xS$, $0 \leq x \leq 0.09$) structure is responsible for structural disorders and hence, results in degradation of crystallinity. The incorporation of Ni^{2+} ions in CdS shows band gap narrowing. A transition in magnetic phase from diamagnetism to para/weak ferromagnetism with Ni content in CdS nanofilms has been observed.

The crystallite size, interplanar spacing and lattice parameter ratio decrease with increasing Co^{2+} concentration in CdS ($Cd_{1-x}Co_xS$, $0 \leq x \leq 0.08$) nanofilms. A red shift in the peak position of Cd–S stretch and optical band gap has been found with Co^{2+} content. The diamagnetic state of CdS vanishes with increasing Co content for $x = 0.02$ and a transition to ferromagnetic state at $x > 0.02$ has been observed.

The pure and transition metal doped CdS nanofilms deposited using low molar concentration of chemicals *via* chemical bath deposition which grow with columnar structure of crystallites parallel to the plane of substrate possess less grain boundaries. The CdS nanofilms, having low thickness (< 100 nm), small crystallite size (< 30 nm) and high transmittance (> 75%) may be suitable for photovoltaic, optoelectronic and visible light detection applications.

The stable wurtzite structure, high transmittance and band gap tailoring of Ni^{2+} & Co^{2+} doped CdS nanofilms in visible region and UV end of solar spectrum make them suitable for large area coating of photovoltaic devices, anti–reflection coating, solar control coating and warming window layers. The flexibility in magnetic phase from diamagnetic to para/ferromagnetic with transition metal (Ni^{2+} & Co^{2+}) content in CdS and the presence of low magnetic coercivity, may offer multipurpose dilute magnetic semiconductors for opto–electronic, magneto–optical and spintronics applications.

REFERENCES

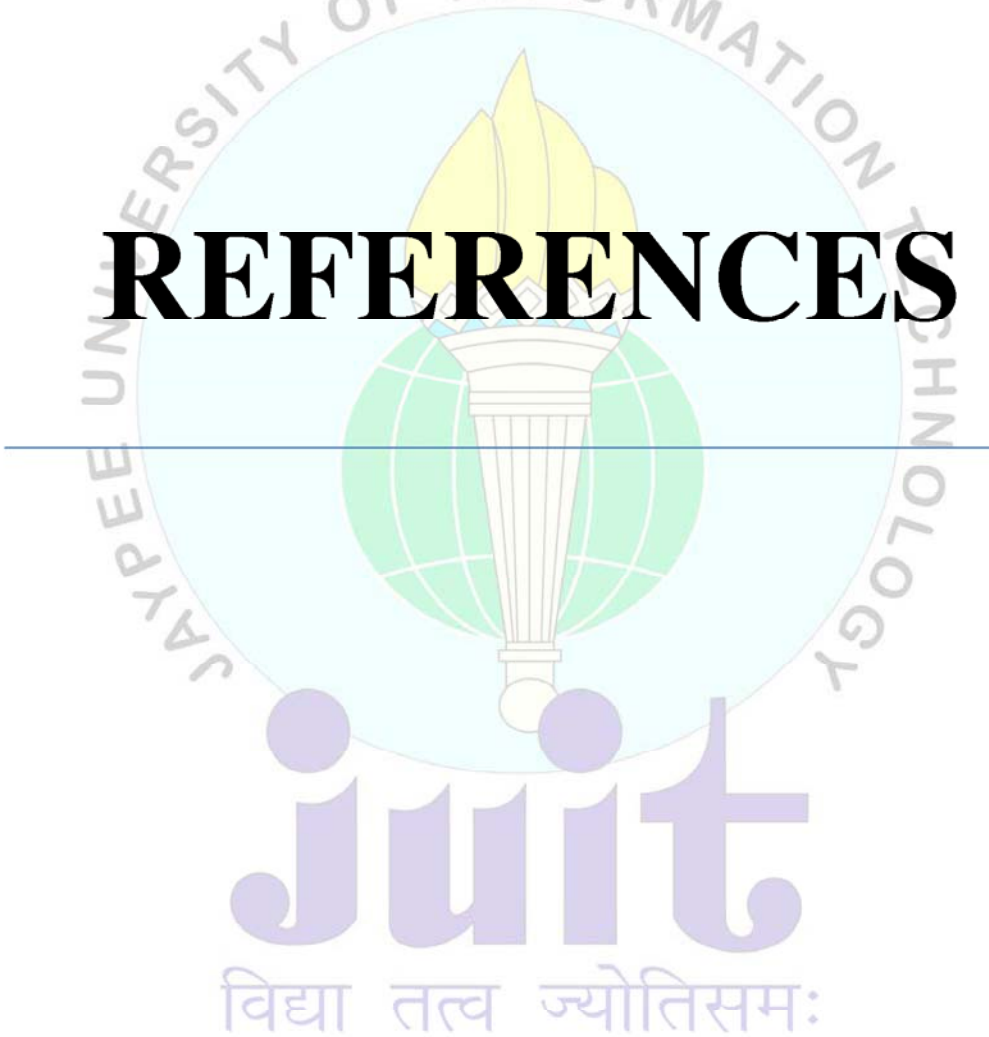
JAYPEE UNIVERSITY OF INFORMATION TECHNOLOGY
juit
विद्या तत्व ज्योतिसमः

JAYPEE UNIVERSITY OF INFORMATION TECHNOLOGY
juit
विद्या तत्व ज्योतिसमः

1. Turnbull D 1969 *Contemp. Physics* **10** 473
2. Kittel C 2004 *Introduction to Solid State Physics* (New York: John Wiley & Sons)
3. Sze S M 1981 *Physics of Semiconductor Devices* 2nd edn (New York: Wiley – Intrascience)
4. Chu T L and Chu S S 1995 *Solid State Electron.* **38** 533
5. Lee S C 1998 *The Nanobiological Strategy for Construction of Nanodevices* in *Biological Molecules in Nanotechnology: The Convergence of Biotechnology, Polymer Chemistry and Materials Science* eds Lee S C and Savage L (Southborough, MA: IBC Press)
6. Cao G 2004 *Nanostructures & Nanomaterials: Synthesis, Properties & Applications* (London: Imperial College Press)
7. Shen G and Chen D 2009 *Nanoscale Res. Lett.* **4** 779
8. Hochbaum A I and Yang P 2010 *Chem. Rev.***110** 527
9. Mirov S, Fedorov V, Moskalev I, Mirov M and Martyshkin D 2013 *J. Luminescence* **133** 268
10. Yang H, Santra S and Holloway P H 2005 *J. Nanosci. Nanotechno.* **5** 1364
11. Afzaal M and O'Brien P 2006 *J. Mater. Chem.* 16 1597
12. Yao W T and Yu S H 2008 *Adv. Funct. Mater.* **18** 3357
13. Saran A D and Bellare J R 2010 *Colloids Surf. A: Physicochem. Eng. Aspects* **369** 165
14. Kirovskaya I A, Timoshenko O T and Karpova E O 2011 *Russ. J. Phys. Chem.* A **85** 557
15. Liu X, Jiang Y, Lan X, Zhang Y, Li S, Li J, Han T, Wang B and Zhong H 2011 *Mater. Chem. Phys.* **130** 909
16. Jin M J, Chen X Y, Gao Z M, Ling T and Du X W 2012 *Nanotechnology* **23** 485401
17. Wang J and Isshiki M 2007 *Wide–bandgap II–VI Semiconductors: Growth and Properties* Chapter 16 in *Springer Handbook of Electronic and Photonic Materials* ed Kasap S and Capper P (New York: Springer–Verlag) p 325
18. Pearton S J, Abernathy C R, Overberg M E, Thaler G T, Norton D P, Theodoropoulou N, Hebard A F, Park Y D, Ren F, Kim J and Boatner L A 2003 *J. Appl. Phys.* **93** 1

19. Lupan O, Pauporte T, Chow L, Vianae B, Pelle F, Ono L K, Cuenya B R and Heinrich H 2010 *Appl. Surf. Sci.* **256** 1895
20. Minegishi K, Koiwai Y, Kikuchi Y, Yano K, Kasuga M and Shimizu A 1997 *Jpn. J. Appl. Phys.* **36** L1453
21. Hwang D K, Bang K H, Jeong M C and Myoung J M 2003 *J. Cryst. Growth* **254** 449
22. Sharma P, Gupta A, Rao K V, Owens F J, Sharma R, Ahuja R, Guillen J M O, Johansson B and Gehring G A 2003 *Nat. Mater.* **2** 673
23. Sato K and Yoshida H K 2001 *Jpn. J. Appl. Phys.* **40** L334; Sato K and Yoshida H K 2002 *Phys. Status Solidi* ***B*** **229** 673; Sato K and Yoshida H K 2002 *Semicond. Sci. Technol.* **17** 367; Sato K, Bergqvist L, Kudrnovsky J, Dederichs P H, Eriksson O, Turek I, Sanyal B, Bouzerar G, Yoshida H K, Dinh V A, Fukushima T, Kizaki H and Zeller R 2010 *Rev. Mod. Phys.* **82** 1633
24. Ozgur U, Alivov Y I, Liu C, Teke A, Reshchikov M A, Dogan S, Avrutin V, Cho S J and Morkoc H 2005 *J. Appl. Phys.* **98** 041301
25. Dou Y, Egdell R G, Walker T, Law D S L and Beamson G 1998 *Surf. Sci.* **398** 241
26. Dakhel A A 2009 *J. Alloys Compd.* **475** 51
27. Ueda N, Maeda H, Hosono H and Kawazoe H 1998 *J. Appl. Phys.* **84** 6174
28. Khallaf H, Chen C T, Chang L B, Lupan O, Dutta A, Heinrich H, Shenouda A and Chow L 2011 *Appl. Surf. Sci.* **257** 9237
29. Kar S and Chaudhuri S 2004 *Chem. Phys. Lett.* **414** 40
30. Biswas S and Kar S 2008 *Nanotechnology* **19** 045710
31. Bredol M and Merikhi J 1998 *J. Mater. Sci.* **33** 471
32. Oladeji I O and Chow L 1999 *Thin Solid Films* **339** 148; Oladeji I O and Chow L 2005 *Thin Solid Films* **474** 77
33. Bhargava R N, Gallagher D, Hong X and Nurmikko A 1994 *Phys. Rev. Lett.* **72** 416
34. Bae W K, Kwak J, Lim J, Lee D, Nam M, Char K, Lee C and Lee S 2009 *Nanotechnology* **20** 075202
35. Sambasivam S, Joseph D P, Lin J G and Venkateswaran C 2009 *J. Solid State Chem.* **182** 2598
36. Zeng X, Zhang J and Huang F 2012 *J. Appl. Phys.* **111** 123525

37. Patel S P, Pivin J C, Patel M K, Won J, Chandra R, Kanjilal D and Kumar L 2012 *J. Magn. Magn. Mater.* **324** 2136
38. O'Brien P and McAleese J 1998 *J. Mater. Chem.* **8** 2309
39. Goudarzi A, Aval G M, Park S S, Choi M C, Sahraei R, Ullah M H, Avane A and Ha C S 2009 *Chem. Mater.* **21** 2375
40. Pawlikowski J M 1985 *Thin Solid Films* **127** 9
41. Pramanik P and Biswas S 1986 *J. Electrochem. Soc.* **133** 350
42. Hankare P P, Chate P A, Sathe D J, Chavan P A and Bhuse V M 2009 *J. Mater Sci: Mater. Electron.* **20** 374
43. Wang S Y, Hauksson I, Simpson J, Stewart H, Adams S J A, Wallace J M, Kawakami Y, Prior K A and Cavenett B C 1992 *Appl. Phys. Lett.* **61** 506
44. Rusu G I, Popa M E, Rusu G G and Salaoru I 2003 *Appl. Surf. Sci.* **218** 222
45. Begum M Sk, Nirmala G, Ravindranadh K, Aswani T, Rao M C, Rao P S and Ravi R V S S N K 2011 *J. Mol. Struc.* **1006** 344
46. Lad A D, Rajesh C, Khan M, Ali N, Gopalakrishnan I K, Kulshreshtha S K and Mahamuni S 2007 *J. Appl. Phys.* **101** 103906
47. Kumar P and Singh K 2011 *J. Nanopart. Res.* **13** 1613
48. Mahalingam T, John V S, Rajendran S and Sebastian P J 2002 *Semicond. Sci. Technol.* **17** 465
49. Saito H, Zayets V, Yamagata S and Ando K 2003 *Phys. Rev. Lett.* **90** 207202
50. Erlacher A, Lukaszew A R, Jaeger H and Ullrich B 2006 *Surf. Sci.* **600** 3762
51. Pattar J, Sawant S N, Nagaraja M, Shashank N, Balakrishna K M, Sanjeev G and Mahesh H M 2009 *Int. J. Electrochem. Sci.* **4** 369
52. Aqili A K S, Saleha A J, Ali Z and Al–Omaria S 2012 *J. Alloys Compd.* **520** 83
53. Guo M, Gao G and Hu Y 2011 *J. Magn. Magn. Mater.* **323** 122
54. McCandless B E and Sites J R 2003 *Cadmium Telluride Solar Cells* Chapter 14 in *Handbook of Photovoltaic Science and Engineering* eds Luque A and Hagedus S S (Chichester: John Wiley & Sons Ltd) p 617
55. Neretina S, Hughes R A, Britten J F, Sochinskii N V, Preston J S and Mascher P 2007 *Nanotechnology* **18** 275301
56. Shah N A, Ali A, Aqili A K S and Maqsood A 2006 *J. Cryst. Growth* **290** 452
57. Al–Douri A A J, Al–Shakily F Y, Alias M F A and Alnajjar A A 2010 *Adv. Condens. Matter Phys.* **2010** 947684

58. Kosyachenko L A, Maslyanchuk O L, Gnatyuk V A, Lambropoulos C, Rarenko I M, Sklyarchuk V M, Sklyarchuk O F and Zakharuk Z I 2008 *Semicond. Sci. Technol.* **23** 075024

59. Mnasri S, Nasrallah S A B, Sfina N, Bouarissa N and Said M 2009 *Semicond. Sci. Technol.* **24** 095008

60. Alver U, Bacaksız E and Yanmaz E 2008 *J. Alloys Comp.* **456** 6

61. Ung T D T, Tran T K C, Pham T N, Nguyen D N, Dinh D K and Nguyen Q L 2012 *Adv. Nat. Sci.: Nanosci. Nanotechnol.* **3** 043001

62. Rai B K, Bist H D, Katiyar R S, Nair M T S, Nair P K and Mannivannan A 1997 *J. Appl. Phys.* **82** 1310

63. Velumani S, Narayandass Sa K, Mangalaraj D, Sebastian P J and Mathew X 2004 *Sol. Energy Mater. Sol. Cells* **81** 323

64. Kale R B and Lokhande C D 2005 *Semicond. Sci. Technol.* **20** 1

65. Wang G X, Park M S, Liu H K, Wexler D and Chen J 2006 *Appl. Phys. Lett.* **88** 193115

66. Broody T P, Asars J A and Dixon G D 1973 *IEEE Tran. Electron Devices.* ED–20 11 995

67. Singh S B, Limaye M V, Date S K, Gokhale S and Kulkarni S K 2009 *Phys. Rev.* B **80** 235421

68. Kumar S, Kumar S, Verma N K and Chakarvarti S K 2011 *J. Mater Sci: Mater. Electron.* **22** 901

69. Zhong Q H and Liu C H 2008 *Thin Solid Films* **516** 3405

70. Hayden O, Greytak A B and Bell D C 2005 *Adv. Mater.* (Weinheim, Ger.) **17** 701

71. Reiss P, Protiere M and Li L 2009 *Small* **5** 154

72. Feng M, Sun R, Zhan H and Chen Y 2010 *Nanotechnology* **21** 075601

73. Liu P, Singh V P, Jarro C A and Rajaputra S 2011 *Nanotechnology* **22** 145304

74. Joseph J, Nishad K K, Sharma M, Gupta D K, Singh R R and Pandey R K 2012 *Mater. Res. Bull.* **47** 1471

75. Fang J, Wu J, Su L, Zhang X, Mao H, Shena Y and Lu Z 1997 *J. Mater. Chem.* **7** 737

76. Mondal S P and Ray S K 2009 *Appl. Phys. Lett.* **94** 223119; Mondal S P, Aluguri R and Ray S K 2009 *J. Appl. Phys.* **105** 114317; Mondal S P, Reddy V S, Das S, Dhar A and Ray S K 2009 *Nanotechnology* **19** 215306

77. Pfisterer F and Schock H W 1982 *J. Cryst. Growth* **59** 432

78. Hirai T, Miyamoto M and Komasawa I 1999 *J. Mater. Chem.* **9** 1217

79. Chandramohan S, Kanjilal A, Tripathi J K, Sarangi S N, Sathyamoorthy R and Som T 2009 *J. Appl. Phys.* **105** 123507; Chandramohan S, Kanjilal A, Sarangi S N, Majumder S, Sathyamoorthy R and Som T 2009 *J. Appl. Phys.* **106** 063506; Chandramohan S, Strache T, Sarangi S N, Sathyamoorthy R and Som T 2010 *Mater. Sci. Eng.* B **171** 16

80. Zhong Z H, Wang D L, Cui Y, Bockrath M W and Lieber M C 2003 *Science* **302** 1377

81. Murai H, Abe T, Matsuda J, Sato H, Chiba S and Kashiwaba Y 2005 *Appl. Surf. Sci.* **244** 351

82. Wei T Y, Huang C T, Hansen B J, Lin Y F, Chen L J, Lu S Y and Wang Z L 2010 *Appl. Phys. Lett.* **96** 013508

83. Dhawale D S, Dubal D P, Jamadade V S, Salunkhe R R, Joshi S S and Lokhande C D 2010 *Sensors and Actuators* B **145** 205–210

84. Dang T C, Pham D L, Nguyen H L and Pham V H 2010 *Adv. Nat. Sci: Nanosci. Nanotechnol.* **1** 035010

85. Wang Y, Wu J, Zheng J, Jiang R and Xu R 2011 *Catal. Sci. Technol.* **2** 581

86. Villasenor A L S, Mejia I, Lerma M S, Gnade B E and Lopez M A Q 2012 *Appl. Phys. Lett.* **101** 262103

87. Adachi S 2009 *Properties Of Semiconductor Alloys Group* IV, III–V and II–VI semiconductors (West Sussex, England: John Wiley & Sons Ltd)

88. Datta S, Dasgupta T S and Sarma D D 2008 *J. Phys.: Condens. Matter.* **20** 445217

89. Zhai T, Fang X, Li L, Bando Y and Golberg D 2010 *Nanoscale* **2** 168

90. Yeh C Y, Lu Z W, Froyen S and Zunger A 1992 *Phys. Rev.* B **46** 10086

91. He C, Liu B, Li M, Su T and Gao C 2012 *J. Appl. Phys.* **111** 113718

92. Derin H and Kantarli K 2009 *Surf. Interface Anal.* **41** 61

93. Dingyu Y, Xinghua Z, Zhaorong W, Weiqing Y, Lezhong L, Jun Y and Xiuying G 2011 *J. Semicond.* **32** 023001

94. Kokotov M, Feldman Y, Avishai A, DeGuire M and Hodes G 2011 *Thin Solid Films* **519** 6388

95. Pal U, Gonzalez R S, Martinez G M, Jimenez M G, Vidal M A and Torres S 1997 *Thin Solid Films* **305** 345

96. Hu S, Zheng J, Feng L, Li W and Yang D 2010 *Power and Energy Engineering Conference*, Asia–Pacific, 10.1109/APPEEC.2010.5449533

97. Dhawale D S, Dubal D P, Phadatare M R, Patil J S and Lokhande C D 2011 *J. Mater. Sci.* **46** 5009

98. Tong X L, Jiang D S, Hu W B, Liu Z M and Luo M Z 2006 *Appl. Phys.* A **84** 143

99. Kaur I, Pandya D K and Chopra K L 1980 *J. Electrochem. Soc.* **127** 943

100. Choi J Y, Kim K J, Yoo J B and Kim D 1998 *Solar Energy* **64** 41

101. Mahanty S, Basak D, Rueda F and Leon M 1999 *J. Electron. Mater.* **28** 559

102. He X W, Liu W F, Zhu C F and Jiang G S 2011 *Chin. J. Chem. Phys.* **24** 471

103. Feitosa A V, Miranda M A R, Sasaki J M and Araujo M A S 2004 *Braz. J. Phys.* **34** 656

104. Khallaf H, Oladeji I O, Chai G and Chow L 2008 *Thin Solid Films* **516** 7306

105. Rakhshani A E and Al–Azab A S 2000 *J. Phys.: Condens. Matter.* **12** 8745

106. Sasikala G, Thilakan P and Subramanian C 2000 *Sol. Energy Mater. Sol. Cells* **62** 275

107. Lazos C D G, Rosendo E, Oliva A I, Ortega M, Perez P B, Juarez H, Diaz T, Garcia G and Rubin M 2010 *Thin Solid Films* **518** 5387

108. Kim M J, Lee S H and Sohn S H 2011 *Thin Solid Films* **519** 1787

109. Acevedo A M, Galan O V, Puente G C, Larramendi J V, Mejia G A, Castaheda M C, Esquivel A E, Contreras H H, Carbajal A A and Gandarilla F C 2002 *IEEE Photovoltaic Specialists Conference* 624

110. Lee J 2005 *Appl. Surf. Sci.* **252** 1398

111. Brus L E *J. Chem. Phys.* 1983 **79** 5566; Brus L E 1986 *J. Phys. Chem.* **90** 2555

112. Kayanuma Y 1988 *Phys. Rev. B* **38** 9797

113. Lippens P E and Lannoo M 1990 *Phys. Rev. B* **41** 6079

114. Einvoll G T 1992 *Phys. Rev. B* **45** 3410

115. Nanda K K, Sarangi S N, Mohanty S and Sahu S N 1998 *Thin Solid Films* **322** 21

116. Zou Y, Li D and Yang D 2010 *Nanoscale Res. Lett.* **5** 966

117. Sebastian P J 1993 *Appl. Phys. Lett.* **62** 2956

118. Kim S Y, Kim D S, Ahn B T and Im H B 1993 *Thin Solid Films* **229** 227

119. Wu X J, Shen D Z, Zhang Z Z, Zhang Y J, Liu K W, Li B H, Lu Y M, Zhao D X and Yao B 2002 *Appl. Phys. Lett.* **89** 262118

120. Thambidurai M, Muthukumarasamy N, Agilan S, Arul N S, Murugan N and Balasundaraprabhu R 2011 *J. Mater. Sci.* **46** 3200; Thambidurai M, Muthukumarasamy N, Velauthapillai D, Murugan N, Chaudhuri J, Parameswaran S, Marathe A, Agilan S and Balasundaraprabhu R 2012 *J. Mater. Sci: Mater. Electron.* **23** 618

121. Marandi M, Taghavinia N, Sedaghat Z, Iraji zad A and Mahdavi S M 2008 *Nanotechnology* **19** 225705

122. Bogle K A, Ghosh S, Dhole S D, Bhoraskar V N, Fu L F, Chi M F, Browning N D, Kundaliya D, Das G P and Ogale S B 2008 *Chem. Mater.* **20** 440

123. Firdous A, Singh D and Ahmad M M 2012 *Appl. Nanosci.* DOI 10.1007/s13204–012–0065–0

124. Furdyna J K 1988 *J. Appl. Phys.* **64** R29

125. Dietl T 1994 *Diluted Magnetic Semiconductors* Chapter 14 in *Handbook of Semiconductors* vol. **3** B eds Mahajan S (Amsterdam: North Holland) p. 1251

126. Ohno H 1998 *Science* **281** 951; Ohno H 2010 *Nat. Mater.* **9** 952

127. Dietl T, Haury A and Merle d'Aubigne Y 1997 *Phys. Rev.* B **55** R3347; Dietl T, Ohno H, Mutsukura F, Cibert J and Ferrand D 2000 *Science* **287** 1019; Dietl T, Ohno H and Matsukura F 2001 *Phys. Rev.* B **63** 19520; Dietl T and Ohno H 2001 *Physica* E **9** 185; Dietl T and Ohno H 2003 *MRS Bulletin* 714

128. Prellier W, Fouchet A and Mercey B 2003 *J. Phys.: Condens. Matter* **15** R1583

129. Liu Y and Liu B G 2006 *J. Magn. Magn. Mater.* **307** 245

130. Seong M J, Alawadhi H, Miotkowski I and Ramdas A K 2001 *Phys. Rev.* B **63** 125208

131. Liu C, Yun F and Morkoc H 2005 *J. Mater. Sci.: Mater. Electron.* **16** 555

132. Akai H 1998 *Phys. Rev. Lett.* **81** 3002; Akai H 1993 *Phys. Rev.* B **47** 8739

133. Jiang Y, Yan W, Sun Z, Liu Q, Pan Z, Yao T, Li Y, Qi Z, Zhang G, Xu P, Wu Z and Wei S 2009 *J. Phys.: Conf. Ser.* **190** 012100

134. Bouzerar G, Bouzerar R and Cepas O 2007 *Phy. Rev.* B **76** 144419

135. Prinz G A 1998 *Science* **282** 1660

136. Zener C 1950 *Phys. Rev.* **81** 440; Zener C 1951 *Phys. Rev.* **83** 299

137. Ruderman M A and Kittel C 1954 *Phys. Rev.* **96** 99

138. Yosida K 1957 *Phys. Rev.* **106** 893

139. Blinowski J, Kacman P and Dietl T 2001 *MRS Fall Meeting*. 690

140. Chelikowsky J R, Kaxiras E and Wentzcovitch R M 2006 *Phys. Stat. Sol.* (b) **243** 2133

141. Wolf S A, Awschalom D D, Buhrman R A, Daughton J M, Molnar S V, Roukes M L, Chtchelkanova A Y and Treger D M 2001 *Science* **294** 1488

142. Boeck J D, Roy D V, Das J, Motsnyi V, Liu Z, Lagae L, Boeve H, Dessein K and Borghs G 2002 *Semicond. Sci. Technol.* **17** 342

143. Chambers S A and Yoo Y K 2003 *MRS Bulletin* 706

144. Fert A 2008 *Rev. Mod. Phys.* **80** 1517

145. Bhattacharyya S, Estrin Y, Rich D H, Zitoun D, Koltypin Y and Gedanken A 2010 *J. Phys. Chem.* C **114** 22002

146. Pang X, Zhang J, Gao K and Volinsky A A 2011 *Mater. Lett.* **65** 2728

147. Baibich M N, Broto J M, Fert A, Dau F N V, Petroff F, Etienne P, Creuzet G, Friederich A and Chazelas J 1988 *Phys. Rev. Lett.* **61** 2472; Binasch G, Grunberg P, Saurenbach F and Zinn W 1989 *Phys. Rev.* B **39** 4828

148. Storchak V G, Eshchenko D G, Luetkens H, Morenzoni E, Lichti R L, Marenkin S F, Pashkova O N and Brewer J H 2006 *Physica* B **374–375** 430

149. Sarkar I, Sanyal M K, Kar S, Biswas S, Banerjee S, Chaudhuri S, Takeyama S, Mino H and Komori F 2007 *Phys. Rev.* B **75** 224409

150. Wang C C, Liu M, Man B Y, Chen C S, Jiang S Z, Yang S Y, Gao X G, Xu S C, Hu B, Sun Z C, Guo J J and Hou J 2012 *AIP Advances* **2** 012182

151. Herbich M, Mac W, Twardowski A, Ando K, Shapira Y and Demianiuk M 1998 *Phys. Rev.* B **58** 1912; Herbich M, Mac W, Twardowski A and Demianiuk M 1999 *Phy Rev* B **59** 2726

152. Mac W, Herbich M, Twardowski A and Demianiuk M 2000 *Semicond. Sci. Technol.* **15** 748

153. Zhang X W, Fan W J, Li S S and Xia J B 2007 *Phys. Rev.* B **76** 195306

154. Nazir S, Ikram N and Tanveer M 2009 *J. Phys. Chem.* A **113** 6022

155. Ren M, Zhang C, Li P, Song Z and Liu X 2012 *J. Magn. Magn. Mater.* **324** 2039

156. Kulkarni J S, Kazakova O and Holmes J D 2006 *Appl. Phys.* A **85** 277

157. Lee L C, Subramaniam N G, Lee J W and Kang T W 2007 *Appl. Phys. Lett.* **90** 262909

158. Liu K W, Zhang J Y, Shen D Z, Wu X J, Li B H, Li B S, Lu Y M and Fan X W 2007 *Appl. Phys. Lett.* **90** 092507

159. Delikanli S, He S, Qin Y, Zhang P, Zeng H, Zhang H and Swihart M 2008 *Appl. Phys. Lett.* **93** 132501

160. Bacaksiz E, Tomakin M, Altunbas M, Parlak M and Colakoglu T 2008 *Physica* B **403** 3740

161. Aksu S, Bacaksiz E, Parlak M, Yilmaz S, Polat I, Altunbas M,Turksoy M, Topkaya R and Ozdogan K 2011 *Mater. Chem. Phys.* **130** 340

162. Gao Y, Sun L, Chen P and Zhang W 2011 *Appl. Phys.* A **103** 97

163. Srivastava P, Kumar P and Singh K 2011 *J. Nanopart. Res.* **13** 5077

164. El–Hagary M and Soltan S 2012 *J. Appl. Phys.* **112** 043907

165. Kumar S, Kumar S, Jain S and Verma N K 2012 *Appl. Nanosci.* **2** 127

166. Murali G, Reddy D A, Prakash B P, Vijayalakshmi R P, Reddy B K and Venugopal R 2012 *Physica B*: *Phys. Condens. Matter.* **407** 2084

167. Saravanan L, Pandurangan A and Jayavel R 2011 *J. Nanopart. Res.* **13** 1621

168. Oh E, Choi J H, Oh D K and Park J 2008 *Appl. Phys. Lett.* **93** 041911

169. Tunkasiri T,Tontrakoon J, Sirlratwatanakul N and Thongtem S 1983 *Science Asia* **9** 257

170. http://learn.adafruit.com/photocells

171. Singh U P and Patra S P 2010 *Int. J. Photoenergy* **2010** Article ID 468147

172. Coutts T J 1982 *Thin Solid Films* **90** 451

173. Reynolds D C, Leies G, Antes L L and Marburger R E 1954 *Phys. Rev.* **96** 533

174. Fraas L M and Yale MA 1977 Journal of Crystal Growth **39** 92

175. Contreras M A, Ramanathan K, Shama J A, Hasoon F, Young D L and Egaas B R 2005 *Prog. Photovolt. Res. Appl.* **13** 209

176. Wu X 2004 *Solar Energy* **77** 803

177. Repins I, Contreras M A and Egaas B 2008 *Progress in Photovoltaics: Res. Appl.* **16** 235

178. Voss C, Subramanian S and Chang C H 2004 *J. Appl. Phys.* **96** 5819

179. Iyyer S B, Sayyed S A and Bhand G R 2012 *AIP Conf. Proc.* **1451** 203

180. Ye Y, Dai L, Wu P C, Liu C, Sun T, Ma R M and Qin G G 2009 *Nanotechnology* **20** 375202

181. Mereu B, Sarau G, Pentia E, Draghici V, Lisca M, Botila T and Pintilie L 2004 *Mater. Sci. Eng.* B **109** 260

182. Smyntyna V A, Golovanov V, Kashulis S, Mattogno G and Viticoli S 1994 *Sensors and Actuators* B **19** 460

183. Urbanczyk M, Jakubik W and Maciak E 2006 *Molecular and Quantum Acoustics* **26** 273

184. Tristao J C, Magalhaes F, Corio P and Sansiviero M T C 2006 *J. Photochem. Photobiol.* A **181** 152

185. Singh S, Singh M, Yadav B C, Tandon P, Pomogailo S I, Dzhardimalieva G I and Pomogailo A D 2011 *Sensors and Actuators* B **160** 826

186. Zhang Y, Zhang N, Tang Z R and Xu Y J 2012 *Chem. Sci.* **3** 2812

187. Hong E, Choi J and Kim J H 2013 *Thin Solid Films* **527** 363

188. Benlattar M, Oualim E M, Mouhib T, M. Harmouchi, Mouhsen A and Belafhal A 2006 *Optics Communications* **267** 65

189. Mitra M, Drayton J, Cooray M L C, Karpov V G and Shvydkac D 2007 *J. Appl. Phys.* **102** 034505

190. Rao C S and Reddy C E 2009 *Indian J. Pure & Appl. Phys.* **47** 54

191. http://www.nanofilmtechnology.com/documents/presskit/What_is_nanotechnology.pdf

192. Rajeshwar K, de Tacconi N R and Chenthamarakshan C R 2001 *Chem. Mater.* **13** 2765

193. Rao C N R, Vivekchand S R C, Biswas K and Govindaraj A 2007 *Dalton Trans.* **34** 3728

194. Hodes G 2003 *J. Electrochem. Soc. Proceedings* **31** 129

195. Ohring M 2002 *Materials Science of Thin Films* 2nd edn (San Diego: Academic Press)

196. Liebig J 1835 *Ann. Pharmaz.* **14** 134

197. Lincot D and Hodes G 2006 *Overview of The History and Present Trends in Chemical Bath Deposition of Thin Solid Films and Structures* in *Electrochemical society Proceeding* PV 2002–32 (Pennington, New Jersey: The Electrochemical Society)

198. Hodes G and Calzaferri G 2002 *Adv. Funct. Mater.* **12** 501

199. Hodes G 2002 *Chemical Solution Deposition of Semiconductor Films* (New York: Marcel Dekker, Inc.)

200. Hodes G 2007 *Phys. Chem. Chem. Phys.* **9** 2181

201. Pawar S M, Pawar B S, Kim J H, Joo O S and Lokhande C D 2011 *Curr. Appl. Phys.* **11** 117
202. Pasquarelli R M, Ginley D S and O'Hayre R 2011 *Chem. Soc. Rev.* **40** 5406
203. Ramaiah K S, Bhatnagar A K, Pilkington R D, Hill A E and Tomlinson R D 2000 *J Mater. Sci.: Mater. Electron.* **11** 269
204. Roy P and Srivastava S K 2006 *J. Phys. D: Appl. Phys.* **39** 4771
205. Khallaf H, Oladeji I O and Chow L 2008 *Thin Solid Films* **516** 5967
206. Khallaf H, Chai G, Lupan O, Heinrich H, Park S, Schulte A and Chow L 2009 *J. Phys. D: Appl. Phys.* **42** 135304
207. Khallaf H, Chen C T, Chang L B, Lupan O, Dutta A, Heinrich H, Shenouda A and Chow L 2011 *Appl. Surf. Sci.* **257** 9237
208. Liu F, Lai Y, Liu J, Wang B, Kuang S, Zhang Z, Li J and Liu Y 2010 *J. Alloys Comp.* **493** 305
209. Boyle D S, O'Brien P, Otway D J and Robbe O 1999 *J. Mater. Chem.* **9** 725
210. www.ambiostech.com, *Operational manual titled next generation XP–Plus series high resolution surface profilometers*
211. Flewit P E J and Wild R K 2003 *Physical Methods for Material Characterization* (Bristol: IOP publishing)
212. Goldstein J I, Newbury D E, Echlin P, Joy D C, Romig A D, Lyman C E, Fiori C and Lifshin E 1992 *Scanning Electron Microscopy and X–ray Microanalysis* 2nd edn (New York: Plenum Press)
213. Howland R and Benatar L 2000 *A Practical Guide to Scanning Probe Microscopy* 1st edn (Sunnyvale, CA: ThermoMicroscopes)
214. Bhushan B 2011 *Nanotribology and Nanomechanics I: Measurement Techniques and Nanomechanics* 3rd edn (Heidelberg: Springer) p 37
215. Cullity B D 1978 *Elements of X–ray Diffraction* (New York, USA: Addison–Wesley)
216. Cappuccio G and Terranova M L 1996 *Thin film Characterization by Advanced X–ray Diffraction Techniques in Proceeding of V School on X–ray Diffraction from Polycrystalline Materials* (Frascati, Italy: SIS)
217. Wilson A J C 1949 *X–ray Optics* (London: Methuen) p 65
218. Lorinczi A 1999 *J. Optoelectron. Adv. Mater.* **1** 37
219. Kozhevnikova N S, Kurlov A S, Uritzkaya A A and Rempel A A 2004 *J. Struct. Chem.* **45** S154

220. Whitfield P and Mitcheli L 2004 *Int. J. Nanosci. Nanotech.* **3** 757

221. Williamson G K and Hall W H 1953 *Acta Cryst.* **1** 22

222. Gao J, Jie W, Yuan Y, Wang T, Zha G and Tong J 2001 *J. Vac. Sci. Technol.* A **29** 051507

223. Watt M 1997 *The Principles and Practice of Electron Microscopy* 2nd edn (UK: Cambridge university press) p 60

224. Hsu C P S 1997 *Infrared Spectroscopy* Chapter 15 in *Handbook of Instrumental Techniques for Analytical Chemistry* eds Settle F A (New Jersey: Prentice Hall)

225. Sole J G, Bausa L E and Jacque D 2005 *An Introduction to The Optical Spectroscopy of Inorganic Solids* (Chichester: John Wiley & Sons Ltd)

226. Pankove J I 1971 *Optical Processes in Semiconductors* (New York: Dover)

227. Salem A M, El–Gendy Y A, Sakr G B and Soliman W Z 2008 *J. Phys. D: Appl. Phys.* **41** 025311

228. Roy D K 2004 *Physics of semiconductor devices* (Hyderabad, India: University Press) p 450

229. Tauc J 1970 *The Optical Properties of Solids* (Amsterdam: North–Holland)

230. Urbach F 1953 *Phys. Rev.* **92** 1324

231. Tan W C, Koughia K, Singh J and Kasap S O 2006 *Fundamental Optical Properties of Materials I* Chapter 1 in *Optical Properties of Condensed Matter and Applications* eds Singh J (Chichester: John Wiley & Sons Ltd)

232. Jiles D 1998 *Introduction to Magnetism and Magnetic Materials* (London: Chapman & Hall)

233. Cullity B D and Graham C D Jr 2008 *Introduction to Magnetic Materials* 2nd edn (New York: Wiley–IEEE Press)

234. http://www.nanomagnetics.org/instrumentation_and_characterization/index.php

235. Yang H 2006 *Met. Mater. Int.***12** 351

236. Ji X, Li H, Cheng S, Wu Z, Xie Y, Dong X and Yan P 2011 *Mater. Lett.* **65** 2776

237. Challa K K, Goswami S K, Oh E and Kim E T 2011 *Appl. Phys. Lett.* **99** 153111

238. Kim D, Hwang C, Gwoo D, Kim T, Kim Y, Kim N and Ryu B K 2011 *Electron. Mater. Lett.* **7** 309

239. Singh V K, Chauhan P, Mishra S K and Srivastava R K 2012 *Electron. Mater. Lett.* **8** 295

240. Galan O V, Carbajal A A, Perez R M, Rodriguez G S, Hernandez J S, Alonso J C, Garcia E M, Puente G C and Acevedo A M 2005 *Semicond. Sci. Technol.* **20** 819

241. Choe J Y, Kim K J and Kim D 1997 *Met. Mater.* **3** 265

242. JCPDS data file 06–0314 and 89–0440

243. AMCSD (database code – 0011167 and 0010058)

244. Mote V D, Purushotham Y and Dole B N 2011 *Cryst. Res. Technol.* **46** 705

245. Kumpf C, Neder R B, Niederdraenk F, Luczak P, Stahl A, Scheuermann M, Joshi S, Kulkarni S K, Chory C B, Heske C and Umbach E 2005 *J. Chem. Phys.* **123** 224707

246. Cannas C, Casu M, Lai A, Musinu A and Piccaluga G 1999 *J. Mater. Chem.* **9** 1765

247. Capozzi J, Ivanov I N, Joshi S and Gerhardt R A 2009 *Nanotechnology* **20** 145701

248. Blackwell S, Smith R, Kenny S D, Walls J M and Navarro C F S 2013 *J. Phys.: Condens. Matter* **25** 135002

249. Yadav H K, Sreenivas K and Gupta V 2006 *J. Appl. Phys*. **99** 083507

250. Das R and Kumar R 2010 *Cryst. Res. Technol.* **45** 725

251. Mahmood A, Ahmed N, Raza Q, Khan T M, Mehmood M, Hassan M M and Mahmood N 2010 *Phys. Scr.* **82** 065801

252. Hankare P P, Chate P A, Sathe D J, Chavan P A and Bhuse V M 2009 *J Mater Electron.* **20** 374

253. Riech I, Pena J L, Ares O, Flores A R, Moo V R, Fragoso P R and Alvarez J G M 2012 *Semicond. Sci. Technol.* **27** 045015

254. Vigil O, Angel OZ and Rodriguez Y 2000 *Semicond. Sci. Technol.* **15** 259

255. Morales R L, Falfan M R, Angel O Z and Bon R R 1998 *J. Phys. Chem. Solids*. **59** 1393

256. Lei C, Duch M, Robertson I M and Rockett A 2010 *J. Appl. Phys*. **108** 114908

257. Perkins C L and Hasoon F S 2006 *J. Vac. Sci. Techn. A* **24** 497

258. Lee J H, Song W C, Yi J S, Yang K J, Han W D and Hwang J 2003 *Thin Solid Films*, **431–432** 349

259. Haider A J, Mousa A M and Al–Jawad S M H 2008 *J. Semicond. Technol. Sci.* **8** 326

260. Metin H and Esen R 2003 *J. Cryst. Growth*. **258** 141

261. Oztas M, Bedir M, Ocak S and Yildirim R G 2007 *J. Mater. Sci: Mater. Electron.* **18** 505

262. Li Z Q, Shi J H, Liu Q Q, Wang Z A, Sun Z and Huang S M 2010 *Appl. Surf. Sci.* **257** 122

263. Cortes A, Gomez H, Marotti R E, Riveros G and Dalchiele E A 2004 *Sol. Energy Mater. Sol. Cells* **82** 21

264. Marin E, Santoyo J, Calderon A, Galan O V and Puente G C 2010 *J. Appl. Phys.* **107** 123701

265. Wang S, Yang S, Yang C, Li Z, Wang J and Ge W 2000 *J. Phys. Chem. B* **104** 11853

266. Wang Y, Suna A, Mahler W and Kasowski R 1987 *J. Chem. Phys.* **87** 7315

267. So W W, Jang J S, Rhee Y W, Kim K J and Moon S J 2011 *J. Colloid Interface Sci.* **237** 136

268. Hodes G, Yaran A A, Decker F and Matsuke P 1987 *Phys. Rev. B* **36** 4215

269. Chestnoy N, Haris T D, Hull R and Brus L E 1986 *J. Phys. Chem*. **90** 3393

270. Sapra S and Sarma D D 2004 *Phys. Rev. B* **69** 125304

271. Schulz S and Czycholl G 2005 *Phys. Rev. B* **72** 165317

272. Wang Y and Herron N 1991 *Phy. Rev.* B **42** 7253

273. Moualkia H, Hariech S, Aida M S, Attaf N and Laifa E L 2009 *J. Phys. D: Appl. Phys.* **42** 135404

274. Begum A, Hussain A and Rahman A 2012 *Beilstein. J. Nanotechnol.* **3** 438

275. Lu W, Huang P, Li K, Yan P, Wang Y and Yan B 2013 *Int. J. Electrochem. Sci.* **8** 2354

276. Pawar S M, Gurav K V, Shin S W, Choi D S, Kim I K, Lokhande C D, Rhee J I and Kim J H 2010 *J. Nanosci. Nanotechnol.* **10** 3412

277. Choi Y and Suresh S 2002 *Acta Materialia.* **50** 1881

278. Akyuz I, Kose S, Atay F and Bilgin V 2006 *Semicond. Sci. Technol.* **21** 1620

279. Vigil O, Riech I, Rocha M G and Angel O Z 1997 *J. Vac. Sci. Technol. A* **15** 2283

280. Kariper A, Guneri E, Gode F, Gumus C and Ozpozan T 2011 *Mater. Chem. Phys.* **129** 183

281. Orgassa K, Rau U, Nguyen Q, Schock H W and Werner J H 2002 *Prog. Photovolt. Res. Appl.* **10** 457

282. Enriquez J P and Mathew X 2003 *Sol. Energy Mater. Sol. Cells* **76** 313

283. Das N S, Ghosh P K, Mitra M K and Chattopadhyay K K 2010 *Physica E* **42** 2097

284. Challa K K, Goswami S K, Oh E and Kim E T 2011 *Appl. Phys. Lett.* **99** 153111

285. Krishnakumar V, Han J, Klein A and Jaegermann W 2011 *Thin Solid Films* **519** 7138

286. Dey S N, Chatterjee P and Gupta S P S 2006 *J. Appl. Phys.* **100** 073509

287. Lazos C D G, Rosendo E, Juarez B H, Salgado G G, Diaz T, Falfan M R, Oliva A I, Quintana P, Aguilar D H, Cauich W, Ortega M and Matsumoto Y 2008 *J. Electrochem. Soc.* **155** D158

288. Pal U, Samanta D, Ghorai S, Samantaray B K and Chaudhuri A K 1992 *J. Phys. D appl. Phys.* **25** 1488

289. Cao J and Wua J 2011 *Mat. Sci. Eng. R*, **71** 35

290. Lalitha S, Sathyamoorthy R, Senthilarasu S, Subbarayan A and Natarajan K 2004 *Sol. Energy Mater. Sol. Cells* **82** 187

291. Chen H L, Lu Y M and Hwang W S 2005 *Mater. Trans. JIM* **46** 872

292. H. Metin and R. Esen, *Semicond. Sci. Technol.* **18**, 647 (2003)

293. E. Cetinorgu, C. Gumus and R. Esen, *Thin Solid Films* **515**, 1688 (2006)

294. Jun M C and Koh J H 2012 *Nanoscale Res. Lett.* **7** 294

295. Meeder A, Marron D F, Rumberg A and Steiner M C L, Chu V and Conde J P 2002 *J. Appl. Phys.* **92** 3016

296. Dai Z H, Zhang R J, Shao J, Chen Y M, Zheng Y X, Wu J D and Chen L Y 2009 *J. Korean Phys. Soc.*, **55** 1227

297. Adamska H and Spector H N 1984 *J. Appl. Phys.* **56** 1123

298. Burda C, Chen X, Narayanan R and El–Sayed M A 2005 *Chem. Rev.* **105** 1025

299. Ma C, Moore D, Ding Y, Li J and Wang Z L 2004 *Int. J. Nanotechnology* **1** 431

300. Di Trolio A, Bauer E M, Scavia G and Veroli C 2009 *J. Appl. Phys.* **105** 113109

301. Umebayashi T, Yamaki T, Itoh H and Asai K 2002 *Appl. Phys. Lett.* **81** 454

302. Mane S T, Kamble S S, Lendave S A and Deshmukh L P 2012 *Mater. Lett.* **67** 373
303. Schwartz D A, Kittilstved K R and Gamelin D R 2004 *Appl. Phys. Lett.* **85** 1395
304. Ozer M M, Thompson J R and Weitering H H 2012 *Phys. Rev. B* **85** 125208
305. Polat I, Aksu S, Altunbas M and Bacaksz E 2012 *Phys. Status Solidi A* **209** 160
306. Kyrychenko F V and Ullrich C A 2011 *Phys. Rev. B* **83** 205206
307. Santara B, Pal B and Giri P K 2011 *J. Appl. Phys.* **110** 114322
308. Liang X, Guo P, Wang G, Deng R, Pan D and Wei X 2012 *RSC Adv.* **2** 5044
309. Ming L C, Mei F L, Tao Z X and Lie Z W 2007 *Chin. Phys. Soc.* **16** 95
310. Misra S K, Andronenko S I, Engelhard M H, Thurber A, Reddy K M and Punnoose A 2008 *J. Appl. Phys.* **103** 07D122.
311. Singhal R K, Sharma S C, Kumari P, Kumar S, Xing Y T, Deshpande U P, Shripathi T and Saitovitch E 2011 *J. Appl. Phys.* **109** 063907
312. Podlowski L, Heitz R, Hoffmann A and Broser I 1992 *J Lumin*. **53** 401
313. Quintelas C, Rocha Z, Silva B, Fonseca B, Figueiredo H and Tavares T 2009 *Chem. Eng. J.* **149** 319
314. *Coates J* 2000 *Interpretation of IR spectra, a practical approach* in *Encyclopedia of Analytical Chemistry* eds Mayers R A (Chichester: John Wiley & Sons Ltd.) p 10815
315. Thangadurai P, Balaji S and Manoharan P T 2008 *Nanotechnology* **19** 435708
316. Cabana Z L, Torres C M S and Gonzalez G 2011 *Nanoscale Res. Lett.* **6** 523
317. Li L, Muckerman J T, Hybertsen M S and Allen P B 2011 *Phys. Rev.* B **83** 134202
318. Ubale A U and Bargal A N 2011 *Mater. Res. Bull.* **46** 1000
319. Kim Y D, Chang Y C and Klein M V 1993 *Phys. Rev. B* **48** 17770
320. Samanta K, Bhattacharya P and Katiyar R S 2009 *J. Appl. Phys.* **105** 113929
321. Jiang J Z, Goya G F and Rechenberg H R 1999 *J. Phys.: Condens. Matter* **11** 4063
322. Hanif K M, Meulenberg R W and Strouse G F 2002 *J. Am. Chem. Soc.* **124** 11496
323. Zhang Z, Chen Q, Lee H D, Xue Y Y, Sun Y Y, Chen H, Chen F and Chu W K 2006 *J. Appl. Phys.***100** 043909

324. Santara B, Pal B and Giri P K 2011 *J. Appl. Phys.***110** 114322

325. Chawla A K, Singhal S, Gupta H O and Chandra R 2011 *Thin Solid Films* **520** 1437

326. Fang J S, Luo W H, Hsu C H, Yang J C and Tsai T K 2012 *J Electron Mater.* **41** 122

327. Gopinadhan K, Kashyap S C, Pandya D K and Chaudhary S 2008 *J. Phys.: Condens. Matter* **20** 125208

328. Ivill M, Pearton S J, Rawal S, Leu L, Sadik P, Das R, Hebard A F, Chisholm M, Budai J D and Norton D P 2008 *New J. Phys.* **10** 065002

329. Paz M G S and Bon R R 2011 *Thin Solid Films* **520** 999

330. Sathyamoorthy R, Sudhagar P, Balerna A, Balasubramanian C, Bellucci S, Popov A I and Asokan K 2010 *J. Alloys Compd.* **493** 240

331. Ghosh M, Dilawar N, Bandyopadhyay A K and Raychaudhuri A K 2009 *J. Appl. Phys.* **106** 084306

332. Gadelmawla E S, Koura M M, Maksoud T M A, Elewa I M and Soliman H H 2002 *J. Mater. Process. Technol.* **123** 133

333. Ouyang Z, Pillai S, Beck F, Kunz O, Varlamov S, Catchpole K R, Campbell P and Green M A 2010 *Appl. Phys. Lett.* **96** 261109

334. Asikoglu A and Yukselici M H 2011 *Semicond. Sci. Technol.* **26** 055012

335. Deo N, Bain M F, Montgomery J H and Gamble H S 2005 *J. Mat. Sci. Mater. Electron.* **16** 387

336. Straumal B B, Mazilkin A A, Protasova S G, Myatiev A A, Straumal P B, Schutz G, Aken P A V, Goering E and Baretzky B 2009 Phys. Rev. B **79** 205206

337. Phan M H, Morales M B, Chinnasamy C N, Latha B, Harris V G and Srikanth H 2009 *J. Phys. D: Appl. Phys.* **42** 115007

338. Darbandi M, Stromberg F, Landers J, Reckers N, Sanyal B, Keune W and Wende H 2012 *J. Phys. D: Appl. Phys.* **45** 195001

List of Publications

A. International Journals

1. **Suresh Kumar**, N.S. Negi, Pankaj Sharma and Vineet Sharma, "*Structural, Morphological and Magnetic Analysis of Cd–Co–S Dilute Magnetic Semiconductor Nanofilms*", **Journal of Magnetism and Magnetic Materials** (2014) Vol. 367, 1–8.

2. **Suresh Kumar**, Pankaj Sharma and Vineet Sharma, "*Red Shift in Absorption Edge of $Cd_{1-x}Co_xS$ Nanofilms*", **IEEE Transactions on Nanotechnology** (2014) Vol. 13, 343–348.

3. **Suresh Kumar**, Pankaj Sharma and Vineet Sharma, "*Phase Transition in II–VI Nanofilms of Dilute Magnetic Semiconductors $Cd_{1-x}Ni_xS$*", **Science of Advanced Materials** (2013) Vol. 5, 713–717.

4. **Suresh Kumar**, Pankaj Sharma and Vineet Sharma, "*Red shift in absorption edge of $Cd_{1-x}Ni_xS$ dilute magnetic semiconductor nanofilms*", **Journal of Nanoparticle Research** (2013) Vol. 15, 1662 (pp 8).

5. **Suresh Kumar**, Pankaj Sharma and Vineet Sharma, "*CdS Nanopowder and Nanofilm: Simultaneous Synthesis and Structural Analysis*", **Electronic Materials Letters** (2013) Vol. 9, 371–374.

6. **Suresh Kumar**, Pankaj Sharma and Vineet Sharma, "*CdS nanofilms: Effect of deposition temperature on morphology and optical band gap*", **Physica Scripta** (2013) Vol. 88, 045603 (pp 8).

7. **Suresh Kumar**, Santosh Kumar, Pankaj Sharma, Vineet Sharma and S. C. Katyal, "*CdS nanofilms: Effect of film thickness on morphology and optical band gap*", **Journal of Applied Physics** (2012) Vol. 112, 123512/1–123512/8.

8. **Suresh Kumar**, Pankaj Sharma and Vineet Sharma, "*Structural transition in II–VI nanofilms: Effect of molar ratio on structural, morphological and optical properties*", **Journal of Applied Physics** (2012) Vol. 111, 113510/1–113510/8.

9. **Suresh Kumar**, Pankaj Sharma and Vineet Sharma, "*CdS nanofilms: Synthesis and the role of annealing on structural and optical properties*", **Journal of Applied Physics** (2012) Vol. 111, 043519/1–043519/6.

10. **Suresh Kumar**, Dheeraj Sharma, Pankaj Sharma, Vineet Sharma, P. B. Barman and S. C. Katyal, "*Structural and Optical Study of Chemical Bath Deposited Nano Structured CdS Thin Films*", **American Institute of Physics Conference Proceeding** (2011) Vol. 1393, 179–180.

B. International/National Conferences

1. **Suresh Kumar**, Pankaj Sharma, Vineet Sharma and P. B. Barman, "*Structural study of CBD deposited CdS nanofilm*", International conference on frontiers in nanoscience, nanotechnology and their applications (**NanoSciTech–2012**; Panjab University, Chandigarh, 16–18 Feb) (2012).

2. **Suresh Kumar**, Pankaj Sharma, Vineet Sharma, S. C. Katyal and P. B. Barman, "*XRD Analysis of Chemical Bath Deposited CdS Nanofilms*", National conference on recent trends in materials science (**RTMS–2011**; Jaypee University of Information Technology, Waknaghat, Solan, H.P., 08–10 Oct.) (2011) P–33, p–39.

3. **Suresh Kumar**, Pankaj Sharma and Vineet Sharma, "*Band Gap Study of Chemical Bath Deposited CdS Thin Films*", National Conference on Research methods in Science, Technology and Management (**REMET–2011**; GHEC, Solan, 26–27 March) (2011) p. 26–28.

4. **Suresh Kumar**, Dheeraj Sharma, Pankaj Sharma, Vineet Sharma, P. B. Barman and S. C. Katyal, "*Structural and Optical Study of Chemical Bath Deposited Nano Structured CdS Thin Films*", International conference on advances in condensed and nano materials (**ICACNM–2011**; Panjab University, Chandigarh, 23–26 Feb.) (2011) P–261.